Machine-Learning and First-Principles Modelling: From Dielectric Breakdown in Solids to Mechanical Behavior of High-Entropy Alloys

A Thesis

Submitted for the Degree of

DOCTOR OF PHILOSOPHY

in the Faculty of Science

by

Narendra Kumar

THEORETICAL SCIENCES UNIT

JAWAHARLAL NEHRU CENTRE FOR ADVANCED SCIENTIFIC RESEARCH

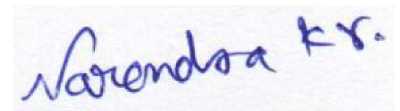Bangalore - 560 064

December 2023

To my parents

DECLARATION

I hereby declare that the matter embodied in the thesis entitled "**Machine-Learning and First-Principles Modelling: From Dielectric Breakdown in Solids to Mechanical Behavior of High-Entropy Alloys**" is the result of investigations carried out by me at the Theoretical Sciences Unit, Jawaharlal Nehru Centre for Advanced Scientific Research, Bangalore, India under the supervision of Prof. Umesh V. Waghmare and that it has not been submitted elsewhere for the award of any degree or diploma.

In keeping with the general practice in reporting scientific observations, due acknowledgement has been made whenever the work described is based on the findings of other investigators.
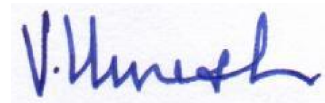
Narendra Kumar

CERTIFICATE

I hereby certify that the matter embodied in this thesis entitled "**Machine-Learning and First-Principles Modelling: From Dielectric Breakdown in Solids to Mechanical Behavior of High-Entropy Alloys**" has been carried out by **Mr. Narendra Kumar** at the Theoretical Sciences Unit, Jawaharlal Nehru Centre for Advanced Scientific Research, Bangalore, India under my supervision and that it has not been submitted elsewhere for the award of any degree or diploma.

Prof. Umesh V. Waghmare

(Research Supervisor)

Acknowledgements

First of all I want to thank my research supervisor Prof. Umesh V. Waghmare for giving me the opportunity to work with him and for encouraging me always. I enjoyed working under his supervision and his constant guidance and motivation helped me to be on the right track. He introduced me to the field of machine learning which I liked. I am again thankful to my supervisor for providing me a fruitful collaboration with Shell Technology Centre, Bangalore (STCB) which addressed industry-related problems such as dielectric breakdown and fuel cells that became part I of this thesis.

I thank my collaborators, Arnab Bhattacharyya at IISc, and Padmini Rajagopalan, Janakiraman Balachandran, and Suchismita Sanyal at STCB for industrial work exposure.

I would like to thank Prof. C.N.R. Rao for providing excellent research facilities and creating a scientific environment within JNCASR. He is a source of inspiration to me.

I am thankful to the present and past chairpersons of "Theoretical Sciences Unit" & "Chemistry and Physics of Materials Unit" whose regular suggestions mentored me in the right direction.

I am privileged to attend courses lectured by Prof. Balasubramanian, Prof. Sundaresan, Prof. Chandrabhas Narayana, Prof. Rajesh Ganapathy, Prof. Ganesh Subramanian, Prof. Kavita Jain, Prof. Swapan K Pati, Prof. Subir K Das, Prof. Umesh V. Waghmare, Prof. Srikanth Sastry, Prof. N S Vidhyadhiraja, Dr. Meher K Prakash, Prof. Chandan Dasgupta (IISc), Prof. Rahul Pandit (IISc), and Dr. Ajay B Harish (UoM).

I am very grateful to all the members of the Materials Theory Group who helped me in many ways during the work embodied in this thesis. I interacted frequently with Aparna, Arijit or

Synopsis

Materials modelling involves the use of ideas and techniques from quantum mechanics and statistical mechanics to simulate and predict the structure and properties of materials at the atomic, molecular, and macroscopic scales. It plays a crucial role in accelerating materials discovery and optimization, reducing the need for time-consuming and expensive experimental trials. Machine learning and first-principles modelling are two powerful computational schemes widely used to understand challenging and complex phenomena in materials science.

Machine learning (ML) algorithms analyze the available datasets of material properties and identify patterns and correlations within data. ML-extracted insights from data help predict new materials with specific properties and identify promising candidates for experimental validation. On the other hand, first-principles calculations solve the Schrödinger equation to accurately describe the interactions between electrons and nuclei in a material. These calculations provide atomistic insights into the electronic structure, bonding, thermal, and mechanical properties of materials. By integrating machine learning and first-principles modeling, this thesis aims to contribute to the advancement of materials science and engineering, focusing on a few systems.

The first part of the thesis focuses on a machine learning approach to understand multi-scale phenomena such as dielectric breakdown in solids (Chapter 2) and proton conduction in perovskite oxides (Chapter 3). Generally, ML models such as neural networks are complicated and hard to interpret. In Chapter 2, we present work on constraining the ML model with dimensional analysis and known physical laws and arrive at a simple, interpretable, and transferable model from a small dataset of dielectric breakdown (a phenomenon relevant to failures in electronic devices and energy storage systems). In Chapter 3, we present an ML framework to model the proton conduction in cubic ABO_3. Relevant descriptors of proton conductivity have been proposed and energy barriers for proton transfer in a few perovskite

oxides have been estimated through first-principles calculations.

The second part of the thesis (Chapters 4-5) shifts the focus to multicomponent alloys within which equiatomic configurations are termed high-entropy alloys (HEAs). An HEA consists of multiple metallic elements in nearly equal atomic concentrations. The core features of HEAs are high configurational entropy, severe internal lattice distortions (ILDs), sluggish diffusion, and cocktail effect. We simulate here special quasirandom structures of HEAs through first-principles calculations. In Chapter 4, we present an analysis of the role of entropy on the phase stability of refractory HEAs and also highlight the origin of internal lattice distortions. In HEAs Nb$_x$HfZrTi, using Voronoi analysis and bond-orientational order parameters as structural descriptors, we identified HCP-BCC transition with increasing Nb-concentration and demonstrated a peak in ILDs at the transition. In Chapter 5, we study the impact of Nb on the mechanical behavior of Nb$_x$HfZrTi high-entropy alloys. We find a switching of failure mode from tetragonal shear to mixed to a pure shear with increasing Nb-concentration. The alloys in this family display an anomalous variation in elastic anisotropy and also exhibit a strength-ductility trade-off as a function of Nb-concentration. We also simulate other quaternary HEAs to juxtapose the results with those of Nb$_x$HfZrTi.

List of Publications

- **Narendra Kumar**, Padmini Rajagopalan, Praveen Pankajakshan, Arnab Bhattacharyya, Suchismita Sanyal, Janakiraman Balachandran*, and Umesh V. Waghmare*. Machine Learning Constrained with Dimensional Analysis and Scaling Laws: Simple, Transferable, and Interpretable Models of Materials from Small Datasets. Chemistry of Materials **31**, 314-321 (2019).

- **Narendra Kumar*** and Umesh V. Waghmare. Entropic stabilization and descriptors of structural transformation in high entropy alloys. Acta Materialia **255**, 119077 (2023).

- **Narendra Kumar** and Umesh V. Waghmare. Anomalous Elastic Anisotropy and Mechanical Behavior of High Entropy Alloys. (*manuscript under preparation*)

- **Narendra Kumar** and Umesh V. Waghmare. Employing Machine Learning to Understand Proton Conduction in Perovskite Oxides. (*manuscript under preparation*)

Not included in the thesis

- Soumya Sanyal, Arun Kumar Sagotra, **Narendra Kumar**, Sharad Rathi, Mohana Krishna, Nagesh Somayajula, Duraivelan Palanisamy, Ram R Ratnakar, Suchismita Sanyal, Partha Talukdar, Umesh Waghmare, Janakiraman Balachandran. Potential energy surface prediction of Alumina polymorphs using graph neural network. arXiv preprint arXiv:2301.12059 (2023).

Machine Learning Constrained with Dimensional Analysis and Scaling Laws: Simple, Transferable, and Interpretable Models of Materials from Small Datasets

Author:
Narendra Kumar, Padmini Rajagopalan, Praveen Pankajakshan, et al

Publication: Chemistry of Materials
Publisher: American Chemical Society
Date: Jan 1, 2019

Copyright © 2019, American Chemical Society

BACK   CLOSE WINDOW

Copyright for Chapter 2

Entropic stabilization and descriptors of structural transformation in high entropy alloys

Author: Narendra Kumar,Umesh V. Waghmare
Publication: Acta Materialia
Publisher: Elsevier
Date: 15 August 2023

Journal Author Rights

BACK   CLOSE WINDOW

Copyright for Chapter 4

Thesis

List of Figures

List of Tables

Contents

Chapter 1

Introduction

1.1 Challenges in condensed matter physics

In 1929, P. A. M. Dirac [1] famously said that

"The underlying physical laws necessary for the mathematical theory of a large part of physics and the whole of chemistry are thus completely known, and the difficulty is only that the exact application of these laws leads to equations much too complicated to be soluble. It, therefore, becomes desirable that approximate practical methods of applying quantum mechanics should be developed, which can lead to an explanation of the main features of complex atomic systems without too much computation."

Dirac's statement necessitates the development of tools and methods to tackle the mathematical challenges that arise when applying those fundamental laws to real-world problems. Density functional theory (DFT) [2, 3] based quantum calculation is one such predictive method widely used today in condensed matter physics, especially for solid-state systems. The properties of crystalline materials are routinely estimated using DFT calculations and that compare quite well with the experiment [4, 5, 6]. However, a high computational cost associated with DFT restricts to simulation of only systems containing a few hundred atoms. The disordered solids lack the symmetries and require a large supercell in their computational modelling and that makes the calculation formidable.

If we were provided unlimited computational resources, we could solve the Schrödinger equation for solids to understand the popular problems in condensed matter physics such as the

quantum phase transitions, dielectric breakdown, proton conduction, and mechanical failure in materials. Generally, we lack the microscopic theories of these phenomena and depend on the phenomenological models to understand them, for example, Ginzburg-Landau theory of phase transitions [7, 8, 9], Frölich-von Hippel criterion of dielectric breakdown [10, 11, 12], Grotthuss mechanism of proton conduction [13], and Griffith criterion of mechanical failure for a specimen containing crack [14] and Born criterion for the mechanical instability of a single-crystal material [15].

In structural materials, understanding of mechanisms of failure is of utmost importance in any application due to long-term performance and safety [16]. Most elemental metals are soft and ductile due to intrinsic non-localized metallic bonding [17, 18]. Single crystals of metals often fail by shear through the movement of dislocations on the slip planes along the closed-packed directions [19, 17]. To enhance their strength (by sacrificing ductility), researchers employ alloying, heat processing, and defect engineering such as altering grain size and introducing secondary phases called precipitates which impede the movement of dislocations [20, 21, 22]. The trade-off between strength and toughness has been a long-standing issue in materials science [23, 24].

High-entropy alloys (HEAs) [25, 26], the equiatomic configurations among multi-elemental mixtures of metals, exhibit superior strength [27, 28, 29, 30, 31, 32, 33, 34] compared to the conventional alloys and also evade the strength-ductility trade-off [35, 36, 37, 38, 39]. The multicomponent nature and intrinsic chemical disorder in HEAs pose several challenges in their computational modelling [40, 41]. The characteristic features of HEAs [42, 43, 21] are (1) high configurational entropy of mixing attributed to stabilizing solid solution phase, (2) severe lattice distortions due to mismatch in the chemistry of alloying elements, (3) sluggish diffusion kinetics, and (4) emergence of exceptional mechanical properties due to mutual interactions among randomly distributed atoms. These four *core aspects* of HEAs are under extensive research to understand the emergence of structural order and exceptional mechanical behavior. Under external loading, an HEA can show a cascade of events comprising stacking fault, twinning, structural transformation, and under the extreme load, amorphization [44, 45, 46, 47].

1.2 First-principles modelling

First-principles modelling of materials refers to the solution of quantum mechanical equations without considering any empirical parameter. Density functional theory (DFT) [2, 3] is one of the most widely used methods in first-principles modeling and simulations. DFT requires only an initial guess of spatial electron density $n(r)$ instead of a many-electron wave function to determine the ground-state properties of a given system after solving Kohn-Sham (KS) equations self-consistently [2, 48]. Therefore, the computational complexity associated with KS-DFT energy calculations is $\mathscr{O}(N^3)$ where N is the number of (valence) electrons present in the system. Although the KS-DFT is effectively a single electron Schrödinger equation, the computational cost of $\mathscr{O}(N^3)$ makes simulations of large-scale systems formidable. Machine-learned interatomic potentials developed by training on DFT configurational energies can be efficiently employed in molecular dynamics simulation of large system size (say μm) of a given material.

1.3 Machine-learning models

Machine learning, a discipline of *artificial intelligence*, does not need any introduction to the current generation of people. Everyone experiences it through spam filtering of emails, automatic recommendations of things and places, and ChatGPT [49] which is an AI language model being used for various tasks. Researchers use machine-learning models to understand complex phenomena across various disciplines such as drug discovery [50], cancer prediction [51], image analysis [52], image recognition [53] and reconstruction [54, 55], remote sensing [56, 57], climate change [58], machine fault diagnosis [59], and materials discovery [60, 61, 62] to name a few.

Many-body interactions within a material are approximately but accurately captured in quantum calculations such as in DFT methods but at high computational cost. This prompts researchers to use simple classical interatomic potentials such as Lennard-Jones potential (which was designed for noble gases [63]) in molecular simulation of large-scale systems and that yields unrealistic results [64]. In the latest development of interatomic potentials, the DFT-based ground state energies of many configurations are used for energy-structure mapping

via machine-learning algorithms. Such an ML functional map between energy and corresponding structure is called machine-learning interatomic potential [65, 66]. I was also involved in the development of CGCNN-based MLIP [67] for different polymorphs of alumina [68] and noted that a huge configurational dataset was required to construct an accurate potential energy surface.

With development of advanced and accurate computational modelling of materials and resources, a huge data are available in various databases such as Materials Project [69], AFLOW [70] NOMAD [71], Khazana [72], and OQMD [73]. In addition to computational databases, there are also multiple experimental databases such as ICSD [74], HTEM [75], and NIST [76]. Since the last decade, availability of enormous data has enabled researchers to learn from the data. Various machine learning algorithms depending on the size of data are being used to develop predictive models of the properties of interest [77, 61]. For a smaller dataset, we rely on classical machine learning algorithms such as linear regression [78] and support vector machine [79]. Neural network-inspired ML algorithms [80, 81] outperform the classical ones but they need large data and lack physical interpretation because those predictive models are complex and not in closed forms [82]. On the other hand, linear regression models contain closed form expressions [83, 84, 85] and we can interpret them by correlation analysis [86] between input and output variables. In some cases, researchers have used empirical relationships based on observed data [87, 88, 89]. Such empirical relations may not have a rigorous theoretical foundation but can provide useful predictions and insights within an ML model. Dimensional analysis [90] can also assist in identifying the right expression by analyzing the units and dimensions of the involved physical quantities [85]. The dimensional analysis approach makes the ML model physically meaningful by interpreting the dimension of each variable participating in regression analysis [85].

1.4 Complex phenomena

There are several phenomena in physical sciences and materials science which lack fundamental understanding. For instance, dielectric breakdown in solids, proton conduction in solids, phase transition, and mechanical failure of solids are technologically relevant but they lack microscopic theories. We rely on phenomenological or mean field theories to understand them. The complexity arises due to their highly nonlinear behavior and spanning across multiple scales. The availability of enormous data due to advancement in computational resources and techniques led one to predict complex phenomena through ML modelling. The complexity and multiscale nature of the studied phenomena is the linking thread of this thesis.

1.4.1 Dielectric breakdown

Dielectric breakdown is the electric field driven failure of dielectric insulators. Under an electric field, a dielectric gets polarized and reduces the internal field. When the electric field strength exceeds a critical value, the dielectric gets ionized or becomes conductive and allows a sudden surge in electric current to pass through it leading to dielectric breakdown. In a defect-free specimen of dielectric, the electric field required to cause dielectric breakdown is maximum and termed as the *intrinsic* dielectric breakdown field (F_b). Therefore, the value of intrinsic F_b depends only on the nature of chemical bonding within a dielectric. According to the Fröhlich-von Hippel dielectric breakdown criterion [10, 11, 12], the breakdown occurs when the energy gain by electrons from the electric field exceeds the energy loss due to electron-phonon scatterings for all electrons occupied closer to the conduction band.

Dielectrics are technologically important due to their application in insulation and capacitors. For safety and long-term performance, electronic/electrical equipment is insulated with a good dielectric to avoid short circuits or electrocution. In capacitors, the stored energy is proportional to the square of applied voltage ($U = \frac{1}{2}CV^2$). Therefore, a high-energy density capacitor should contain a high electric breakdown strength dielectric [91]. The necessity of high F_b dielectrics demands the phenomenological models of dielectric breakdown [83, 92, 85] which can easily predict new dielectrics without any explicit computation [85]. Researchers have resorted to machine-learning modelling for such a complex phenomenon to develop predictive models of dielectric breakdown field which can screen or discover a better dielectric if the right input

descriptors are fed to the models [83, 92, 85].

1.4.2 Proton conduction

Fuel cell technology holds significant potential for converting the chemical energy of hydrocarbon fuels into electricity without emitting air pollutants. Similar to a battery, the fuel cell consists of a cathode and an anode separated by an electrolyte. However, unlike batteries, fuel cells do not require recharging; instead, they rely on a continuous supply of specific fuel for sustained electricity generation. For instance, hydrogen (H_2) is supplied to the anode, where it undergoes oxidation to form H^+ ions, releasing electrons into the external circuit and generating a direct current. The released H^+ ions travel through the proton-conducting electrolyte to the cathode, where they recombine with oxygen and electrons from the external circuit, producing water as a byproduct [93]. In solid oxide fuel cells [94, 95], a solid electrolyte comprises proton- or oxide-ion-conducting ceramics, ensuring compact size, safety, and thermal stability.

The phenomenon of proton conduction in perovskite oxides is intricate, involving the diffusion of protons (H^+) through a hopping process between lattice sites, regulated by the Grotthuss mechanism in solid-state materials [13]. Constructing a machine learning (ML) model to predict proton conductivity in perovskite oxides holds promise for identifying crucial descriptors pertinent to proton conduction. This, in turn, facilitates the expedited discovery and synthesis of superior proton conductors.

1.4.3 Structural phase transition in HEAs

Structural phase transition refers to the change of crystal symmetry due to external perturbation such as stress, temperature, or internal chemical pressure caused by alloying within the solid-state phase. The thermal- and pressure-induced structural transformations are seen in pure chemical elements as allotropy (for example, graphite and diamond are allotropes of carbon) and in compounds as polymorphism (such as alumina exists in different structures depending on the temperature). Reversible austenite-martensite phase transformation with stress or heat in stainless steel and shape memory alloys (for example, NiTi) is a typical example of structural phase transition in materials science.

Phase transitions are often studied using phenomenological models such as Ginzburg-Landau theory [7, 8] which include an *order parameter* having symmetry-dependent distinct values. The microscopic origin of structural transformation is the emergence of soft phonons which make the lattice unstable and, therefore, atomic displacements cause structural change [96, 97, 98]. In internally distorted crystals which arise in multicomponent alloys (say HEAs), the identification of average lattice becomes challenging [99, 100, 101, 102]. In such a noisy crystal, local structure analysis [102] using Voronoi cell partitioning [103] and bond-orientational order parameters help identify the average lattice structure [104, 99].

1.4.4 Mechanical failure

The lattice of crystal structure evolves in response to applied load. For example, a body-centered cubic structural material under tensile load along a [100] direction will cause a phase transformation into a face-centered cubic structure (see Figure 5.5) [105, 97]. In practice, a material fails at a much lower strain [106, 107]. The strength of a material is the value of maximum stress sustained before undergoing failure. For a defect-free single-crystal material, the strength is ultimate. Born's stability criteria [15, 108] in terms of eigenvalues or principal values of elastic constants matrix ($\mathbf{C}$) marks the onset of failure. The eigenvector corresponding to the negative eigenvalue of $\mathbf{C}$ determines the failure mode of a material.

1.5 Overview of the thesis

In this thesis comprised of two parts, we employed machine-learning and first-principles modelling to understand phenomena involving processes at many scales in materials science. Dielectric breakdown in solids, proton conduction in cubic perovskite oxides, and structural stability & mechanical behavior of high-entropy alloys are the topics I have worked on during my Ph.D. tenure. Multi-scale phenomenon is the linking thread among the studied problems here.

Part I of the thesis is dedicated to employing a machine learning (ML) approach for comprehending intricate phenomena, specifically dielectric breakdown in solids (Chapter 2) and proton conduction in perovskite oxides (Chapter 3). Typically, ML models, such as neural networks, pose challenges in terms of complexity and interpretability. In Chapter 3, we

introduce a method to constrain the ML model by incorporating dimensional analysis and established physical laws. This results in a simplified, interpretable, and transferable model derived from a limited dataset of dielectric breakdown–a phenomenon relevant to the malfunctioning of electronic devices and energy storage systems. Chapter 4 delves into an ML framework designed to model proton conduction in cubic ABO_3, where pertinent descriptors of proton conductivity are proposed and estimated through first-principles calculations.

Part II of the thesis (chapters 4-5) shifts the focus to the exploration of complex multicomponent materials known as high-entropy alloys (HEAs). HEAs consist of multiple metallic elements in nearly equal atomic concentrations and are characterized by high configurational entropy, severe internal lattice distortions (ILDs), sluggish diffusion, and the cocktail effect. Special quasirandom structures of HEAs are simulated through first-principles calculations. In Chapter 4, an analysis is presented regarding the impact of entropy on the phase stability of refractory HEAs, along with an exploration of the origin of internal lattice distortions. For HEAs Nb_x(HfZrTi), employing Voronoi analysis and bond-orientational order parameters as structural descriptors, we identify an HCP-BCC transition with increasing Nb-concentration and demonstrate a peak in ILDs at the transition. Chapter 5 delves into an investigation of the elastic and mechanical behavior of HEAs Nb_xHfZrTi. We find a switching of failure mode from tetragonal shear to mixed to a pure shear with increasing Nb-concentration. The alloys of this family display an anomalous variation in elastic anisotropy and also exhibit a strength-ductility trade-off as a function of Nb-concentration. We also simulate a few binary alloys and other quaternary HEAs to compare the results with those obtained for Nb_xHfZrTi.

Note: We have used DFT-based calculations under standard settings. Each work Chapter contains sufficient computational details. Appendix of Chapter 4 contains a detailed discussion on special quasirandom structures, Voronoi cell construction, and bond-orientational order parameters.

Part I

Machine Learning

Chapter 2

Machine Learning Constrained with Dimensional Analysis and Scaling Laws: Simple, Transferable, and Interpretable Models of Materials from Small Datasets

2.1 Introduction

Discovery and design of novel materials with desired properties underpin the development of next-generation energy, mobility, and electronics technologies. At the moment, it takes more than two decades from discovery of a material to development and deployment in a product [109]. The goal of data-driven approaches is to create a new paradigm that can accelerate the materials development lifecycle. One of the challenges in use of data-driven approaches for materials discovery is the lack of large experimental datasets, especially in the space of inorganic materials. This problem can be mitigated through augmentation of the experimental data with data generated from computational models based on ab initio theories. Various projects such as Materials Project [69], AFLOW [70] NOMAD [71], Khazana [72], and OQMD [73] have enabled public sharing of computational datasets that predict materials properties for a wide range of applications such as CO_2 capture [110], piezoelectrics [111], dielectrics [112], photovoltaics [113], thermoelectrics [114], and others.

In spite of the rapid growth in computational resources and data storage capabilities, analysis based on these ab initio models is able to tackle only a small subspace of search space [115]. The large unexplored material search space can be rapidly screened to identify the most promising material candidates for a given application if one develops accurate, computationally inexpensive, interpretable, and transferable data-driven models. Such models can be derived by employing statistical and machine learning (ML) approaches to learn from available materials datasets.

The process of developing data-driven models for materials discovery and the associated challenges are shown schematically in Figure 2.1. A crucial challenge in developing these models is the selection of input features aka descriptors [116, 117, 118]. To represent a material in a concise way to the learning algorithm, it is necessary to extract the right minimal set of features (aka descriptors or fingerprints) that capture the property of interest. The features/descriptors are the columns of the input information in the matrix form shown in Figure 2.1. The features chosen should not be too sparse which leads to loss of information (high bias). On the other hand, employing too many features could lead to overfitting (high variance) and nonunique models. Furthermore, the features must be easily measurable/calculable to ensure that the model can be used efficiently to predict properties in screening of large unexplored materials search spaces.

A major challenge in developing ML models for materials discovery that is well acknowledged in the community [119] involves the limited availability of materials data. In certain instances, such limited data can create challenges pertaining to interpretability and transferability when explored with conventional ML algorithms. In materials science and chemistry, it is particularly important to reconcile such data-driven models with known physics and chemistry to build confidence in these models. Hence, data-driven models should possess physical interpretability. Many ML algorithms such as neural networks, random forests, and kernel regression result in nonlinear models that perform well with respect to the training and test datasets. However, these models do not provide an explicit functional relationship between input descriptors and the target property [119].

Even in case of algorithms such as LASSO [120] and Bootstrapped Projected Gradient Descent (BoPGD) [84] that provide explicit functional relationships, the models are typically very
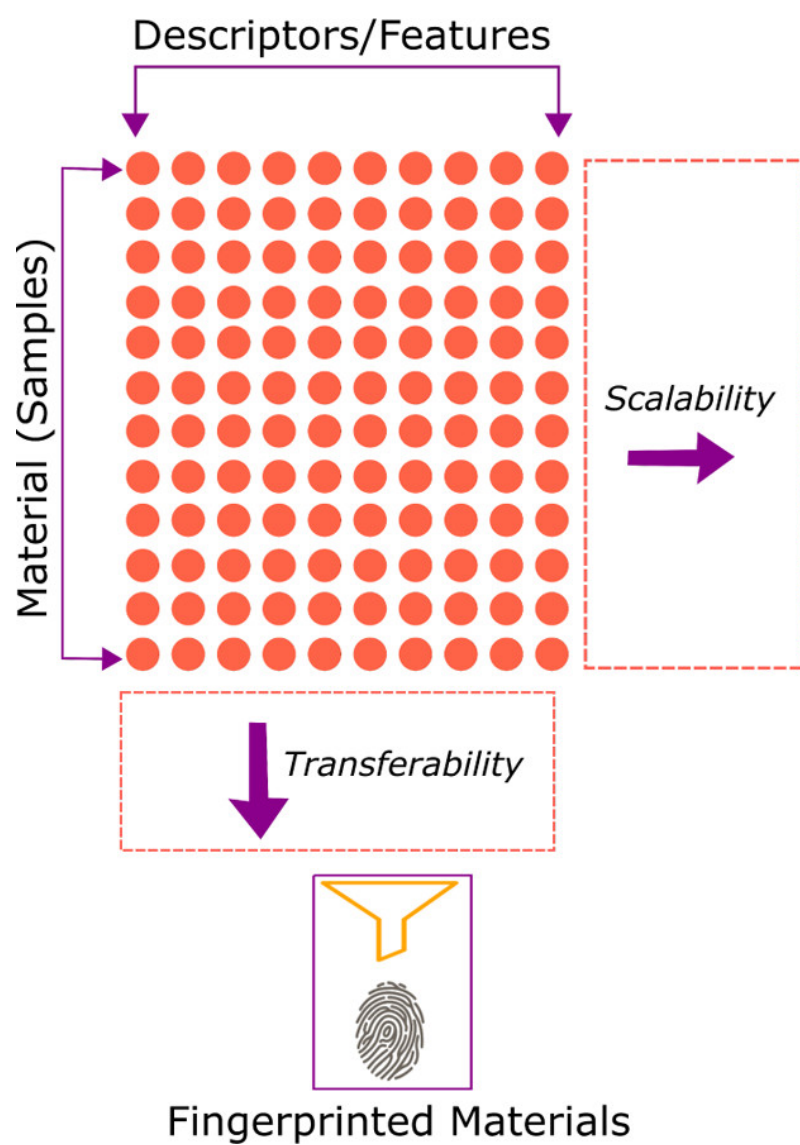
Figure 2.1: Schematic figure that illustrates the process of developing data-driven models for predicting material properties from small datasets through down-selection of a small set of fingerprint descriptors.

complex making the interpretation hard. Moreover, correlations among the descriptors, especially in small materials datasets, can lead to instability, resulting in nonunique fingerprints that are sensitive to the choice of training data.

Further, there is also the risk of high variance (overfitting), where the performance is linked to specific inputs. This in turn limits the transferability of the models. We discuss this aspect in greater detail in Section 2.4, where we analyze the change in model accuracy when the value of one input material (LiF) is changed.

In this article, we address these challenges by developing a hybrid scheme by constraining the data-driven ML (BoPGD) with the Buckingham Pi theorem (BPT)-based dimensional analysis and known empirical scaling relations between descriptors. We demonstrate this approach by developing a stable, accurate, transferable, and physically insightful model to predict the intrinsic dielectric breakdown of inorganic materials.

2.2 Case of dielectric breakdown

Dielectric breakdown is a primary mode of failure of an insulator subjected to high electric fields. When the applied electric field exceeds a critical value, the dielectric becomes a conductor and suddenly allows a large current to flow through it [121]. This phenomenon, called dielectric breakdown, is the electrical analogue of mechanical failure, in which a material loses its load-carrying capacity when subjected to a stress above a critical value.

The phenomenon of dielectric breakdown is influenced by several factors such as defects, grain boundaries, temperature, and pressure. A defect-free dielectric has the highest breakdown field that depends only on its bonding and electronic structure. This maximum theoretical breakdown field is known as intrinsic breakdown field F_b .

In this article, we consider the problem of predicting intrinsic dielectric breakdown (F_b) in elemental and binary dielectric compounds. This dataset comprising target property F_b and eight different primary descriptors that describe different material properties as listed in Table 2.1 was generated by Kim et al. [83].

There are in total 82 materials in the dataset, which can further be classified into three different crystal structures, namely, 36 zinc blende (ZB), 40 rock-salt (RS), and 6 cesium chloride (CC)

compounds (Figure 2.2). The target property of interest (intrinsic breakdown field F_b) spans three orders of magnitude.
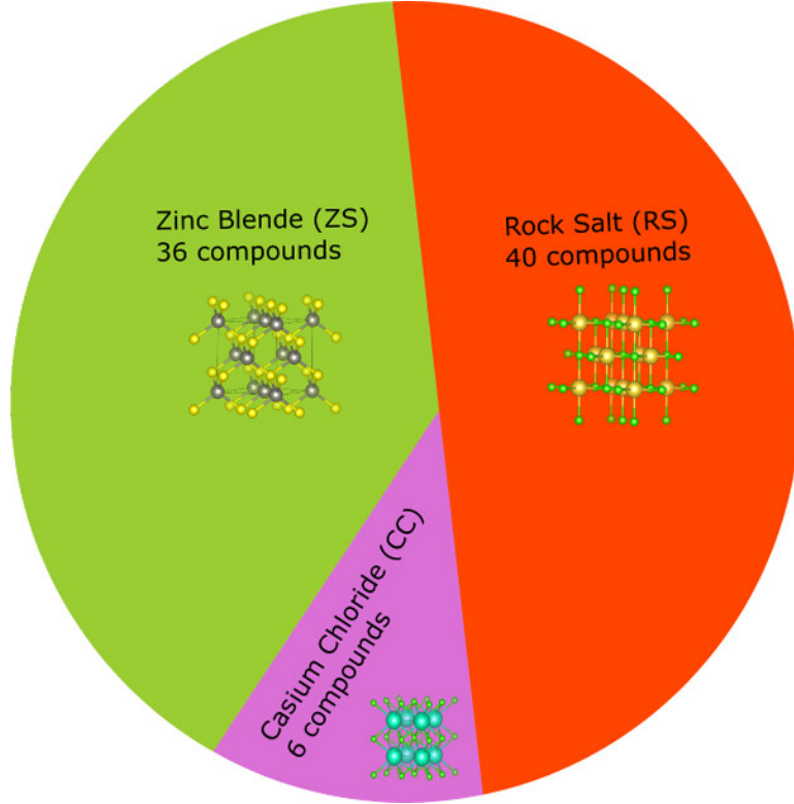
Figure 2.2: Distribution of crystal structures of the 82 dielectric materials [83] explored in this work. Each material in the dataset has one of the three crystal structures: ZB (36), RS (40), and CC (6).

2.3   Principal component analysis and correlation analysis

We first apply some of the basic statistical tools such as principal component analysis (PCA) and pairwise correlations to explore the relationship between descriptors and target property and among descriptors themselves. PCA was applied on the dataset by including the eight input descriptors and the target property of interest (F_b). As shown in Figure 2.3, the first two PCA components account for 72.81% variance in the data and enable us to identify the outlier compounds LiF, BN, and C. Analyzing the coefficient matrix of PCA, we identify that the major contribution to the first two principal components (PC1 and PC2) comes from F_b. Thus, the materials with a very high value of F_b (LiF = 4829.6 MV/m, C = 2624.0 MV/m, and BN = 2062.1 MV/m) demonstrate a clear separation from the rest of the samples when projected into the (PC1, PC2) subspace. Further, we see a clear separation of the materials with RS and ZS

Table 2.1: Descriptors considered in analysis of F_b, their notations and value ranges.

	Descriptor	Notation (unit)	Value Range
1	Band Gap	E_g (eV)	0.20–13.60
2	Phonon cutoff frequency	ω_{max} (THz)	2.91–40.51
3	Average Phonon Frequency	ω_{mean} (THz)	1.42–29.67
4	Electronic part of the dielectric constant	ε_e	1.82–26.29
5	Total dielectric constant	ε_{tot}	4.17–57.21
6	Nearest-neighbor distance	d_{nn} (Å)	1.52–3.60
7	Mass Density	ρ (g/cm^3)	2.32–10.25
8	Bulk Modulus	B (GPa)	18.32–460.52

crystal structures.
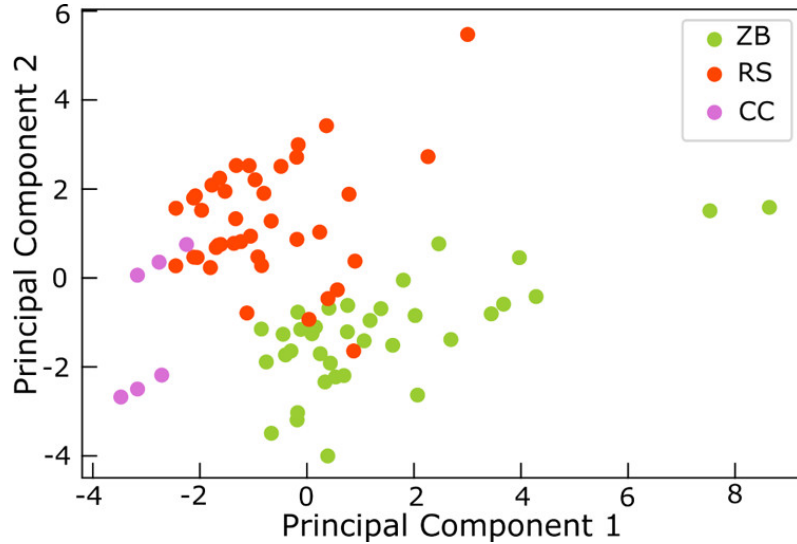
Figure 2.3: Scatter plot of the first and second principal components with outliers on the materials. The compounds LiF, BN, and C, with a very high value of F_b, are separated from the group. We can see a clear separation of the three different crystal structures: ZB, RS, and CC.

To understand the correlations between the descriptors and the target property, we calculate the pairwise correlations ($\hat{\rho}(X^{(p)}, y)$) visualized as a heat map in Figure 2.4 and as a schemaball diagram in the Appendix (Figure A2.5). Here, we observe that F_b correlates positively with E_g and ω_{max} as expected from the models of Kim et al., and Yuan and Mueller [83, 92]. Calculating the pairwise correlations between descriptors ($\hat{\rho}(X^{(p)}, X^{(q)})$), we note that phonon frequencies ($\omega_{max}, \omega_{mean}$) are positively correlated to the bulk modulus (B), consistent with previous experiments [122]. They are also inversely correlated with the nearest-neighbor distance (d_{nn}). Likewise, the electronic dielectric constant (ε_e) and the band gap (E_g) exhibit a

strong inverse correlation consistent with earlier work [123]. Understanding these correlations
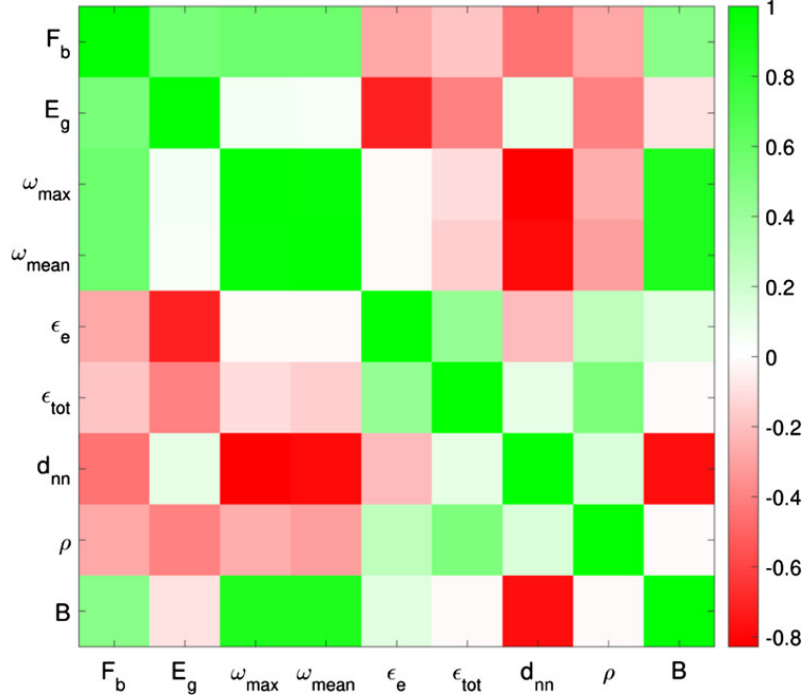
Figure 2.4: Heat map of pairwise correlation between descriptors and target property $(\hat{\rho}(X^{(p)}, y))$ and among descriptors $(\hat{\rho}(X^{(p)}, X^{(q)}))$. Bright green denotes a strong positive correlation, whereas bright red indicates a strong negative correlation between descriptors.

between descriptors is critical in employing our ML scheme that involves clustering of descriptors and down-selecting from those clusters, as described in detail in the next section.

2.4 BoPGD method

In case large-dimensional datasets (X_i, y_i), where i is the number of samples, $\boldsymbol{X_i} \in R^d$, and $y_i \in R$, the goal of sparse estimation methods is to calculate a sparse coefficient vector θ that minimizes the error as

$$\theta = \min_{\beta \in R^d} ||y - X\beta||, \quad \text{subject to} \quad ||\beta||_0 \leq s$$

where $s \leq d$ is the support of the sparse vector. The motivation to perform sparse estimation is to down-select the most important descriptors that are needed to describe the target property. This in turn decreases the model variance (reduces overfitting probability), while simultaneously improving the interpretability of the model [120]. However, the problem in this form cannot be solved optimally because of its NP-hardness. This problem is overcome

through a class of iterative shrinkage thresholding algorithms [124], of which the most commonly used is LASSO [120] that performs this sparse regression with regularization by the l_1 norm.

$$\theta = \min_{\beta \in R^d} ||y - X\beta|| + \lambda ||\beta||_1$$

where $\lambda \geq 0$ is the regularization parameter. Although LASSO has been extensively used in training from various datasets, instability can arise in the LASSO estimate (variables that the algorithm selects), when there are strong correlations between the feature variables (close to multicollinearity) [124].

To overcome these limitations, we employ the BoPGD method. A detailed explanation of this algorithm is provided elsewhere [84, 124]. Here, we summarize the major steps involved in this algorithm. As shown in the green boxes in Figure 2.5, the key ingredients in BoPGD are (i) clustering of descriptors, (ii) bootstrapping the samples, (iii) sparse estimation through Projected Gradient Descent to down-select the dominant cluster for every bootstrap, and (iv) identification of the dominant clusters.

The clustering of descriptors is performed to ensure that strongly correlated descriptors (by magnitude) are grouped into the same cluster, whereas the weakly correlated descriptors end up in different clusters. This in turn enables us to handle the root cause of inconsistency in feature selection — strong correlations among input features that cause the issues in sparse estimation approaches such as LASSO. Here, we employ agglomerative hierarchical clustering (AHC) to cluster the descriptors. Typically, hierarchical clustering is either top-down or bottom-up. AHC is a bottom-up clustering approach in which each descriptor is treated as a cluster and then successively merged until all the descriptors are merged into a single cluster. The distance metric used for clustering is the dissimilarity matrix $D(p,q) = 1 - \left| \hat{\rho} \left(X^{(p)}, X^{(q)} \right) \right|$. A small value of D between two descriptors indicates a strong pairwise correlation and hence they are clustered together, whereas a large value of D suggests that they are not correlated and hence will be classified into different clusters. We can visualize AHC through a dendrogram as shown in Figure A2.6 of the Appendix, where each merge is represented by a horizontal line. The strongly correlated descriptors are merged first for small D values. In this work, we use a cutoff, where the magnitude of pairwise correlation within a cluster is higher than 0.6 ($\hat{\rho}(X^{(i)}, X^{(j)} \geq 0.6$). Alternatively, the dissimilarity matrix has a value lower than 0.4
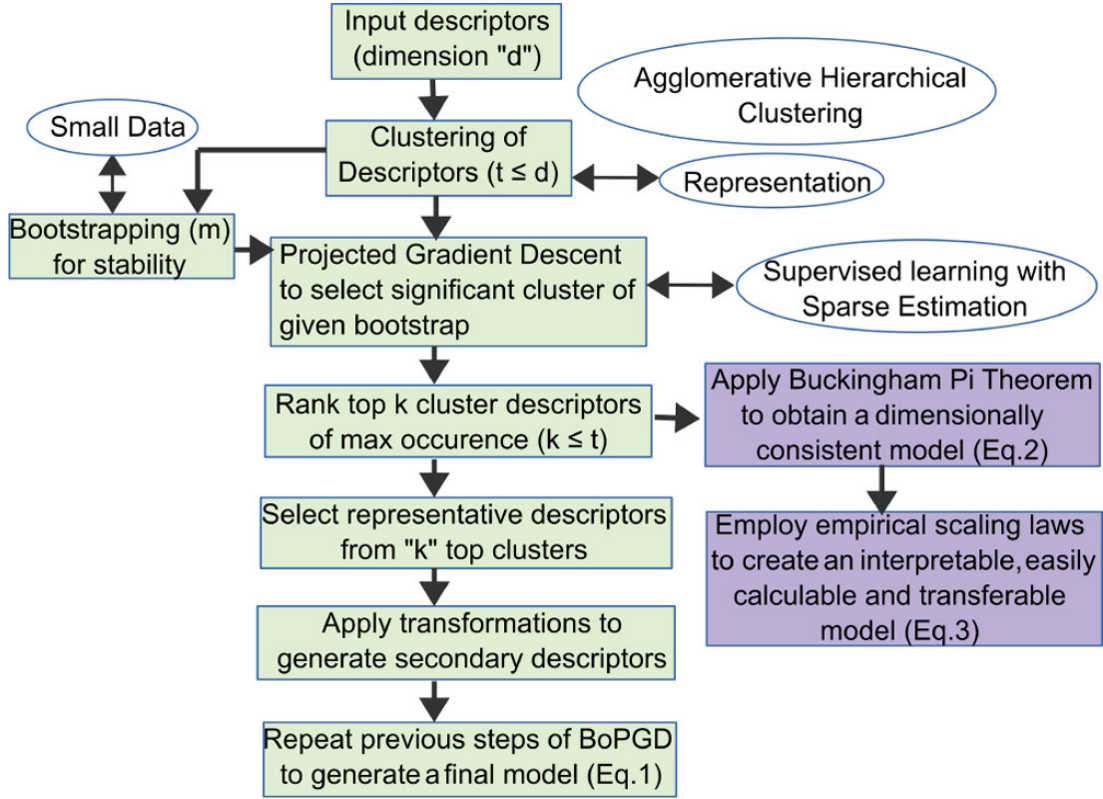
Figure 2.5: Workflow of constraining the BoPGD ML algorithm (in green boxes) with dimensional analysis and known scaling or physical laws (in purple).

$(D(i, j) \leq 0.4)$. Employing this cutoff, we obtain four clusters. The first cluster comprises phonon frequencies $(\omega_{max}, \omega_{mean})$, bulk modulus (B), and nearest-neighbor distance (d_{nn}). The second cluster comprises the electronic part of dielectric constant (ε_e) and band gap (E_g). The mass density (ρ) and total dielectric constant (ε_{tot}) are treated as separate clusters.

Bootstrapping is a resampling method [125] that is used to mimic the availability of several datasets. The goal of bootstrapping is to create m replicas of the n datapoints (samples), that is, $(\boldsymbol{X}(c)_i, y(c)_i)$, where $c = 1, 2, \cdots, m$ and $i = 1, 2, \cdots, n$. These n datapoints for every replica (or bootstrap) is obtained by sampling the original dataset uniformly at random and with replacement. Here, we create 128 bootstraps ($m = 128$) from the original dataset. Bootstrapping increases the sample size and mitigates the stability issues associated with down-selection of the dominant clusters that is discussed in the next paragraph. These down-selection (or sparse estimation) approaches are typically sensitive to specific inputs for small datasets.

The third step is to down-select the most important clusters for every bootstrap through sparse estimation. Here, we employ PGD because PGD scales better compared to other sparse estimation algorithms [126]. Finally, we identify the most frequently down-selected descriptor

clusters from all the bootstraps and select these to be the most important descriptor clusters for the entire dataset.

In this particular dataset when no outliers were ignored, regardless of the way the data were split into training and test sets or any other parameter value, this approach consistently deemed two feature clusters as being the most important for prediction of the intrinsic breakdown field F_b : (i) the first cluster containing bulk modulus (B), nearest-neighbor distance (d_{nn}), and the phonon frequencies ($\omega_{max}, \omega_{mean}$) and (ii) the second cluster containing band gap (E_g) and the electronic part of the dielectric constant (ε_e).

One descriptor (B, E_g) was picked from each down-selected cluster at random. Various linear and nonlinear functions (see Figure A2.4 in the Appendix) were now applied on these two primary descriptors to generate a large number of secondary (compound) descriptors. We again apply the BoPGD algorithm on these compound descriptors and down-select the cluster that possesses the most important compound descriptors. We pick a compound descriptor from the cluster at random. We obtain the coefficients for the model through linear regression on 84% of the complete dataset chosen at random. The final BoPGD model obtained was

$$F_b = 11.48 E_g^{1.02} e^{0.17\sqrt{B}} \tag{2.1}$$

The model described above has a complex form and has limited accuracy, with a coefficient of determination (R^2) of 0.648 as shown in Figure 2.6.

The BoPGD approach used in this work is consistent until the down-selection of primary descriptor clusters. However, instability in the algorithm arises during the creation and down-selection of compound descriptors. This is likely because the input matrix containing compound descriptors has high rank deficiency because of strong correlations among the descriptors and availability of very few samples.

In order to resolve this issue, we apply the BoPGD algorithm only until the down-selection of primary descriptors and then use dimensional analysis along with empirical relationships to obtain a simple, robust, and transferable model.
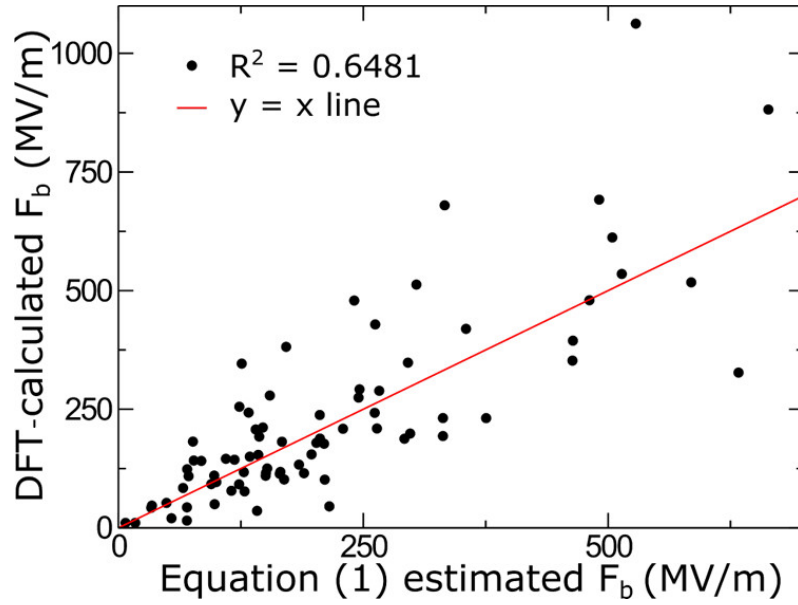
Figure 2.6: Comparison between intrinsic breakdown strength values estimated by eq 2.1 and the original values obtained using density functional theory (DFT) for 78 dielectrics.

2.5 Dimensional analysis with BPT

The Buckingham-Pi Theorem (BPT) is a fundamental theorem in dimensional analysis [90]: if an equation of a physical law in n arguments is dimensionally homogeneous with respect to m fundamental units, it can be expressed as a relation between $n - m$ independent dimensionless arguments. If a physical law is expressed with an equation

$$f(q_1, q_2, \cdots, q_n) = 0$$

where q_i's are the n physical variables, which are expressible in terms of m basic physical dimensions, then the physical law can be rewritten as

$$f(\pi_1, \pi_2, \cdots, \pi_{n-m}) = 0$$

where the π_i's are dimensionless variables constructed from q_i's with a form

$$\pi_i = \prod_{j=1}^{\leq n} q_j^{\alpha_j}$$

We have four fundamental units [mass (M), length (L), time (T) and charge (Q)] in the current dataset that results in $m = 4$. Hence, we need at least five physical variables ($n = 5$) to obtain

20

one dimensional variable (π). Here, we pick the target property F_b along with four input descriptors namely $\{E_g, \omega_{max}, B, \varepsilon_e\}$ from the two down-selected clusters obtained from BoPGD. Inclusion of the electronic dielectric constant(ε_e) is important because it is the only variable that contains the dimension of charge (Q) essential to the physical expression of the target property F_b. Further, we also pick E_g and ω_{max}, that are the descriptors of a previous model developed for the same dataset [83].

For $\pi = F_b{}^{\alpha_1} \varepsilon_e^{\alpha_2} E_g^{\alpha_3} \omega_{max}^{\alpha_4} B^{\alpha_5}$ to be dimensionless, we get $\alpha_3 = \alpha_4 = 0$, $\alpha_2 = \alpha_1/2$, $\alpha_5 = -\alpha_1/2$. Substituting this result in the previous equation, we find that the dimensionless variable π is

$$\pi = F_b \sqrt{\frac{\varepsilon_e}{B}} \Rightarrow F_b = a'\sqrt{\frac{B}{\varepsilon_e}} + b' \tag{2.2}$$

The correlation $F_b \approx \varepsilon_e^{-0.5}$ has also been reported by McPherson et al. [127] which is established here using dimensional analysis.

2.6 Empirical relations

The functional form described in eq 2.2 relates the intrinsic breakdown field (F_b) to bulk modulus (B) and electronic dielectric constant (ε_e). We obtain the linear coefficients of the model ($a' = 152.15, b' = -277.37$) by fitting the data against the 79 compounds. However, this model exhibits limited accuracy ($R^2 = 0.593$ as shown in Figure A2.1 in the Supplementary Information). The negative intercept of the model is of concern because the model would predict an unphysical negative value of F_b for materials with small B or high ε_e. Furthermore, as these descriptors are relatively expensive, the resulting ML model cannot be easily employed to search across a large materials search space.

To improve this model obtained from BPT, we note that the band gap (E_g) is inversely correlated with the electronic part of dielectric constant (ε_e) (see Figures 2.4 and 2.7) and both are present in the same down-selected cluster (obtained from BoPGD). Similarly, the nearest-neighbor distance (d_{nn}), which is computationally trivial, is inversely correlated with bulk modulus (B) (see Figures 2.4 and 2.8), and both are present in the same cluster.

We exploit the knowledge of existing scaling relations in the literature to obtain a functional form of the correlation between (i) E_g versus ε_e and (ii) d_{nn} versus B. It has been proposed in the

literature [87] that the bulk modulus scales in a crystal through a power-law relation: $B \approx d_{nn}^{-3.5}$. Although Cohen [87] established this relation empirically only for diamond and ZB solids, we find it to be valid here for a wider range of crystal structures (RS, ZB, and CC) as shown in Figure 2.8.
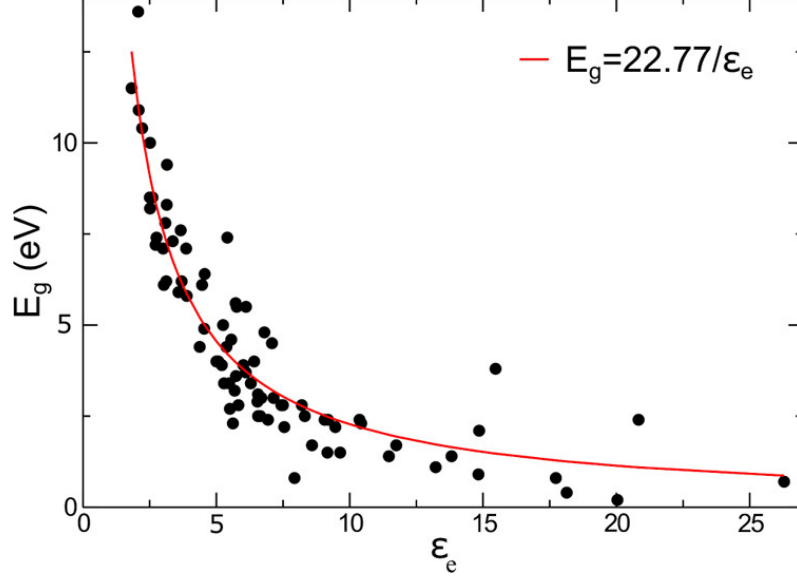
Figure 2.7: Band gap vs electronic dielectric constant for the 82 dielectrics in the dataset. The line represents the inverse law fit to the data points (black dots), confirming the relation $E_g \approx 1/\varepsilon_e$.

The band gap varying inversely with the electronic part of dielectric constant of dielectrics ($E_g \approx 1/\varepsilon_e$) was reported earlier in the literature [123, 88] for oxide dielectrics. The data of Kim et al. also validate this relation (see Figure 2.7). Additionally, we also demonstrate the universality of this behavior by testing it on a large dataset of dielectrics (see Figure A2.3 in the Appendix). We emphasize that even if such empirical correlations were not previously known in the literature, it would have been possible to identify and quantify these correlations, thanks to the cluster-based descriptor down-selection employed by BoPGD (Figure 2.9).

2.7 Simple predictive model

Using the two scaling relations $B \approx d_{nn}^{-3.5}$ and $E_g \approx 1/\varepsilon_e$ in eq 2.2, we get

$$F_b = \sqrt{\frac{E_g}{d_{nn}^{3.5}}}.$$
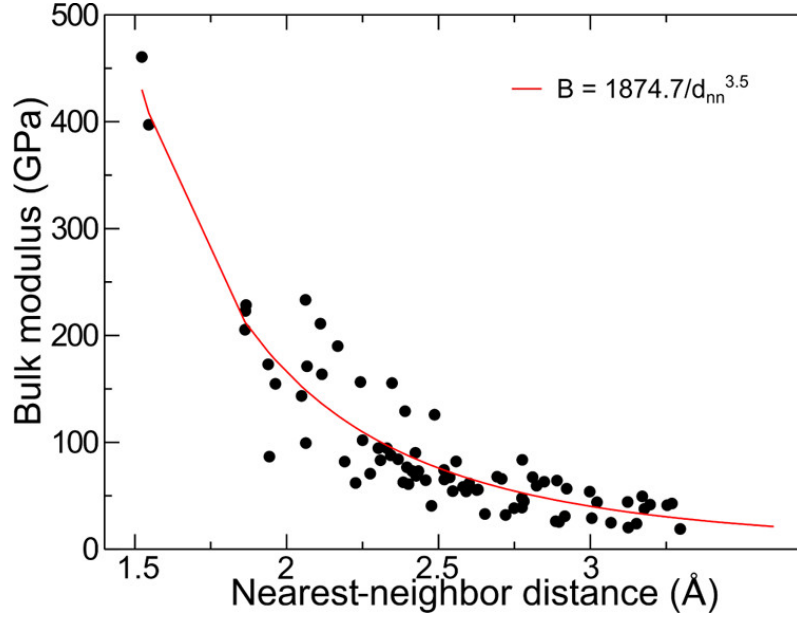
Figure 2.8: Bulk modulus vs the nearest-neighbor distance for the 82 dielectrics in the dataset. The line represents a power-law fit, and the black dots are data points, confirming the relation $B \approx d_{nn}^{-3.5}$.

With a suitable reference, Taylor's series expansion of $F_b = \sqrt{E_g/d_{nn}^{3.5}}$ about $E_g^0/d_0^{3.5}$ to the first-order term gives

$$F_b \simeq F_b^0 + \frac{1}{2F_b^0}\left(\frac{E_g}{d_{nn}^{3.5}} - F_b^0 \times F_b^0\right) = \frac{1}{2F_b^0}\frac{E_g}{d_{nn}^{3.5}} + \frac{F_b^0}{2}$$

where $F_b^0 = \sqrt{E_g^0/d_0^{3.5}}$. Thus, the breakdown field takes a simple form

$$F_b = a\left(\frac{E_g}{d_{nn}^{3.5}}\right) + b.$$

As done earlier for the BPT model, we fit the linear coefficients (a and b) to the data. Fitting it to whole data including compounds with a high breakdown field (such as C, BN, MgO, and LiF) results in an unphysical negative intercept (for $E_g \to 0$, $F_b \to b < 0$). Hence, we fit the coefficients to only 78 compounds, ignoring the four mentioned compounds that possess high values of F_b that skew the model (see Figure A2.2 in the Appendix). The final model we obtain is of the form

$$F_b = 1323(\text{Å}^{3.5}/e)\left(\frac{E_g}{d_{nn}^{3.5}}\right) + 16.25 \tag{2.3}$$

where E_g is in electronvolt, d_{nn} is in angstrom, F_b is in megavolt/meter, and e is the electronic charge.

23

Table 2.2: Comparison of the coefficients of determination (R^2) of our models (eqs 2.1 and 2.3) with previous models for original data and dataset with corrected LiF.

Model	82 materials (Original)	82 materials (Corrected LiF)
BoPGD (eq 2.1)	0.499	0.874
BoPGD+ (eq 2.3)	0.803	0.853
$24.442 \exp\left\{\left(0.315\sqrt{E_g \omega_{max}}\right)\right\}$ [83]	0.908	0.740
$E_g^2 \omega_{max}$ [92]	0.789	0.525
$E_g^2 (\omega_{max} - 1.17)$ [92]	0.811	0.543
$\frac{262\,\omega_{max}}{14.6 - E_g}$ [92]	0.869	0.339
$\frac{348\,\omega_{max}}{15 - E_g} - 101$ [92]	0.901	0.436

The model described in eq 2.3 has a simple form and comprises descriptors that can be easily computed for a wide range of materials (as shown in Figure 2.9). To test the robustness of our model, we compare the coefficient of determination (R^2), which is a measure of the closeness of predicted data to the actual data from our models BoPGD (eq 2.1) and BoPGD with constraints and empirical laws, henceforth called BoPGD+ (eq 2.3) against the prior work by Kim et al. [83] and Yuan et al. [92] as shown in Table 2.2. Kim et al.'s model has the highest accuracy (R^2 = 0.907), whereas the BoPGD+ model has a lower accuracy (R^2 = 0.803) for the original dataset with all the 82 materials. However, in the original dataset, the F_b was calculated for LiF using the band gap criterion, with its experimental band gap (E_g) of around 14.2 eV, and the predicted value of F_b is 4829.6 MV/m. On the other hand, the enthalpy of formation of LiF is only 6.39 eV per formula unit, which is much lower than its band gap. Under high electric field, LiF bond will break, leading to decomposition before reaching the impact ionization in which carriers get populated in their conduction band. Following this bond enthalpy criterion, the F_b of LiF is predicted to be 1290 MV/m [128], much lower than the earlier estimate of 4830 MV/ m [83]. Using this corrected F_b of LiF, we observe that the accuracy of all other models significantly drops (see Table 2.2), whereas the accuracy of the BoPGD+ model slightly improves to R^2 = 0.853. This suggests that our BoPGD+ model has a very low variance indicative of the absence of overfitting. This also suggests that the accuracy and performance of the model are less dependent on the specific inputs to the model.

Table 2.3: Comparison of the coefficients of determination (R^2) of our models (eqs 2.1 and 2.3) with Kim model for different subsets of the materials dataset.

No. of dielectrics	BoPGD (eq 2.1)	BoPGD+ (eq 2.3)	Kim et al. [83]
81 (except LiF)	0.879	0.891	0.880
80 (except LiF, MgO)	0.905	0.907	0.888
78 (except C, BN, MgO and LiF)	0.648	0.807	0.754
40 rock-salt (RS)	0.459	0.865	0.978
38 RS (except LiF and MgO)	0.494	0.861	0.864
36 zinc blende (ZB)	0.970	0.925	0.894
34 ZB (except C and BN)	0.851	0.776	0.635

We further analyze our model output with the Kim et al. model with datasets obtained by removing outliers and applying on subgroups of the dataset as shown in Table 2.3. On removal of four compounds having a higher breakdown field (C, BN, LiF, and MgO), the BoPGD+ model (eq 2.3) ($R^2 = 0.807$) performs more efficiently than the BoPGD model (eq 2.1) ($R^2 = 0.648$) and Kim et al. model ($R^2 = 0.754$). For the subgroup analysis, we analyze the model performance on different crystal structures. We find that Kim et al.'s model has a higher prediction accuracy for dielectrics with RS structure, whereas BoPGD and BoPGD+ models (eq 2.1) perform efficiently for ZB structured compounds. Because of the small number of CC structured dielectrics in the present data, we do not make any comments on the working performance of these models on them. From this comparative analysis, it can be observed that compared to the other two models, the R^2 value of the BoPGD+ model is robust against the removal of outliers and on testing on limited subsets in the data.

In order to demonstrate greater transferability of our model to new material compounds with different crystal structures, we need to have a precise and consistent approach to define the nearest-neighbor distance (d_{nn}). The BoPGD algorithm had previously identified that the first cluster of significance comprises the descriptors: $B, d_{nn}, \omega_{max}, \omega_{mean}$. Here, the descriptors B, ω_{max}, and d_{nn} are all measures of maximum bond stiffness that represent the dielectric breakdown in a material because of bond breaking and decomposition. For example, phonon cutoff frequency (ω_{max}) corresponds to the vibrational frequency of the strongest bond in a
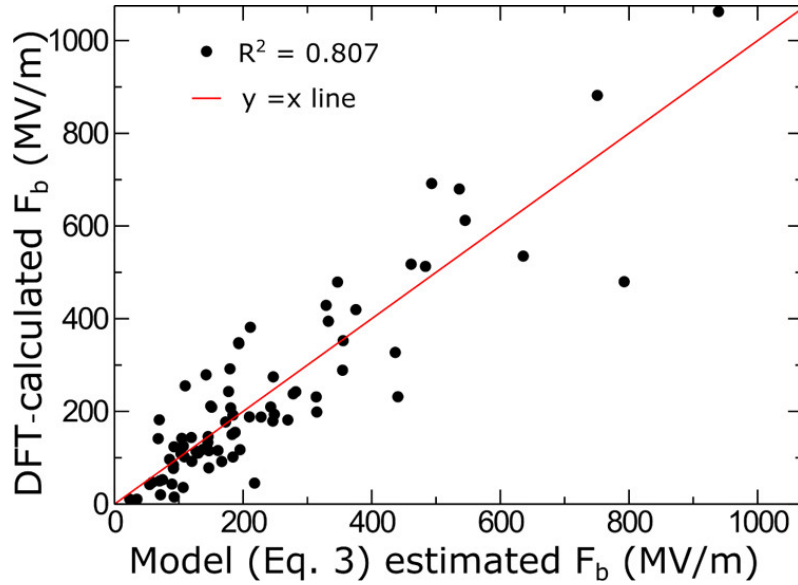
Figure 2.9: DFT estimates of F_b vs F_b obtained with our model from eq 2.3 by fitting against 78 dielectrics.

given material. Such a bond is expected to be the bond between the most electropositive and the most electronegative element in a complex material, and this bond length should be taken as d_{nn} in estimation of the dielectric breakdown field. For elemental compounds, d_{nn} is the same as the nearest-neighbor distance. Following this generalized definition of d_{nn}, we chose 10 crystalline materials [83, 92, 129] from different space groups ($Pm\bar{3}m$, $Fm\bar{3}m$, $P1$, Cm) that were not part of the training/validation process. We note that our model (BoPGD+) consistently provides better prediction of F_b as shown in Figure 2.10. The numerical values are provided for comparison in Table A2.1 in the Appendix. In particular, we find a significantly better accuracy of our model in predicting F_b of fluorides such as $BaBO_2F$, $SrBO_2F$, and $BSiO_2F$.

As described earlier, d_{nn} represents the dielectric breakdown of a material because of bond breaking and decomposition. The other phenomena that can lead to dielectric breakdown is the impact ionization that can populate the conduction band with carriers. This electronic phenomenon of dielectric breakdown in turn depends on the band gap (E_g) of the material. The influence of band gap on the dielectric breakdown in presented as a schematic in Figure 2.11. In case of ionic materials, the valence band is dominated by electronic states originating from the anions, whereas the conduction band is dominated by electronic states of the cations. The work done by an electron for displacement d under an external field E is $-eEd$. This in turn distorts the electronic bands and results in an electron jump from valence band to conduction band. A large band gap requires a high dielectric breakdown field because the energy required
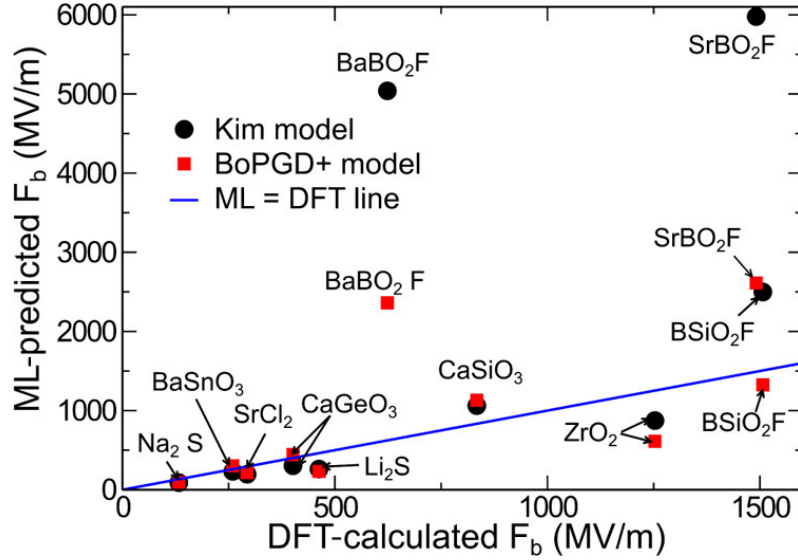
Figure 2.10: Comparison of BoPGD+ and Kim models for 10 other crystalline materials including perovskites and $Pm\bar{3}m$ space group compounds. We note that the BoPGD+ model works relatively better even for other materials. Refer to Table A2.1 in the Appendix for numerical values.

to make an electron jump from valence band to conduction band is higher.

2.8 Conclusions

We have demonstrated a novel hybrid approach in which the ML algorithm (BoPGD) is constrained by the BPT-based dimensional analysis and other known empirical scaling laws that relate the input descriptors. This approach enables the development of simple, transferable, easily calculable, and physically interpretable models to predict functional material properties from small datasets. As a demonstration, we employ this approach to create a model to predict intrinsic dielectric breakdown field. The model is based on readily calculable descriptors (band gap E_g and nearest-neighbor distance d_{nn}) and is trained from only 82 data points. The simple descriptors in our model can be calculated more easily than the phonon cutoff frequency (ω_{max}) in the ML model of Kim et al. [83].

Our results underline the importance of enforcing physical constraints and augmenting ML with pre-existing knowledge of property relationships to develop simple, transferable models for predicting material properties such as dielectric breakdown from sparse datasets. Our approach is generic in nature and can be modified or generalized to study other functional properties with limited data. A few examples from recent literature of such sparse materials
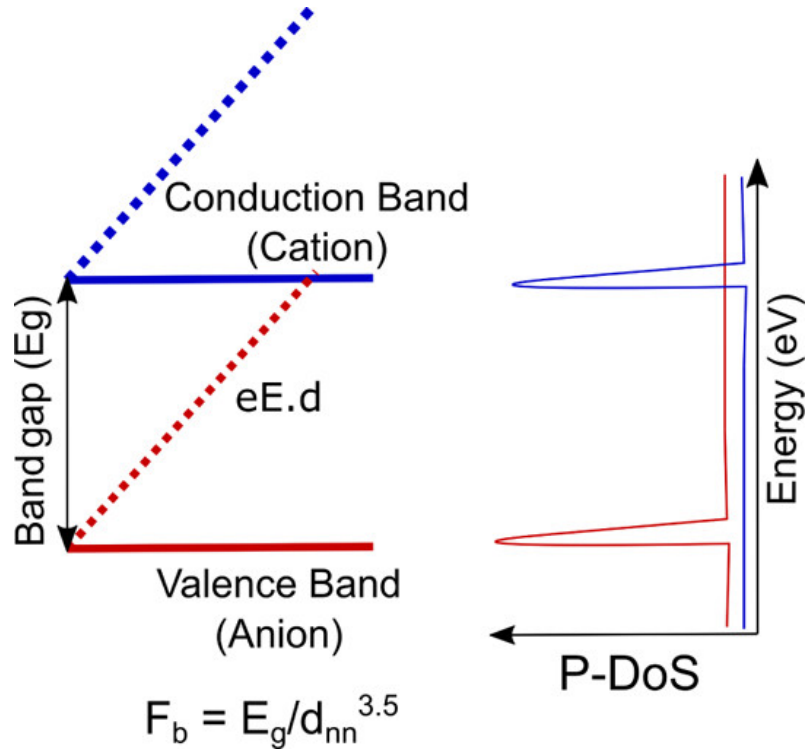
Figure 2.11: Schematic picture representing the band gap of the materials and how it is related to the dielectric breakdown field.

datasets that might be amenable to such hybrid approaches are (i) hybrid organic-inorganic perovskites for photovoltaics [130] (about 212 input materials), (ii) lattice thermal conductivity of inorganic materials [131] (about 93 input materials), (iii) thermal hysteresis of Ni-Ti-based shape memory alloys [132] (about 60 input materials), and (iv) mechanical properties of zeolites [133] (about 121 input materials).

2.9   Appendix

Dimensional Analysis and Scaling Relations

In the manuscript, we have derived a breakdown field expression (eq 2.2 in main manuscript) using *Buckingham Pi theorem*. To fix the proportionality constant, we plotted breakdown field (F_b) *vs.* $\sqrt{B/\varepsilon_e}$ and performed straight-line fitting (see Figure A2.1) for the dataset excluding the three outliers (LiF, BN, C). So the proposed breakdown field model can be written as

$$F_b = 152.15\sqrt{\frac{B}{\varepsilon_e}} - 277.37 \tag{SI-1}$$

From Figure A2.1, we can observe that the model based only on Buckingham Pi theorem
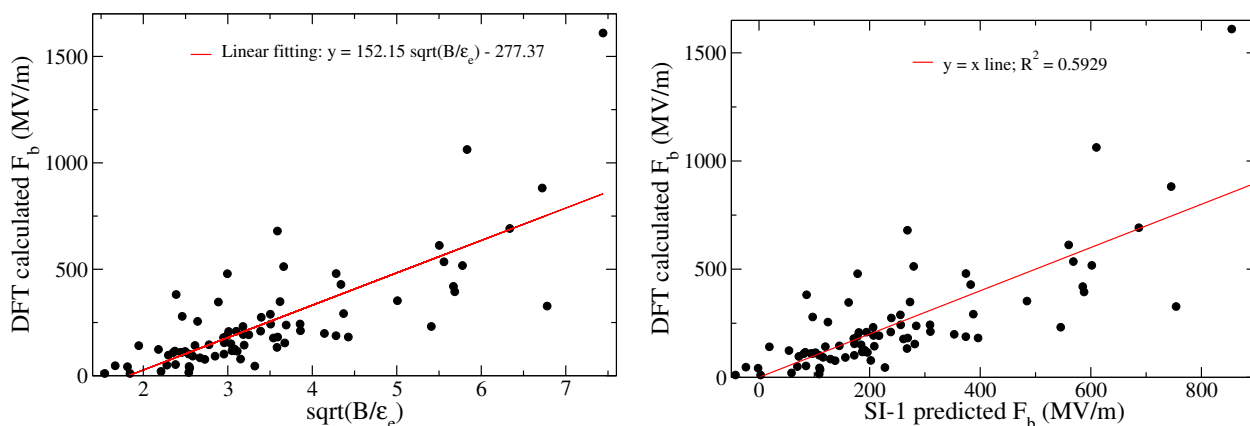
Figure A2.1: Left: F_b vs. $\sqrt{B/\varepsilon_e}$ plot: Linear regression performed to obtain the slope and intercept. The negative intercept (-277.37) can result in unphysical negative values of F_b for small values of $\sqrt{B/\varepsilon_e}$. Right: DFT estimates of F_b vs. F_b obtained using equation SI-1, indicates limited predictive accuracy of the model ($R^2 = 0.5929$ for 79 compounds).

constrain has limited predictive accuracy. Thus, incorporating scaling laws enables us to arrive at eq 2.3 in the paper which improves not only the accuracy, but also the computational simplicity.

Machine Learning

The process of obtaining eq 2.1 in the main manuscript is described here and shown schematically in Figure A2.4. BoPGD algorithm [84] was used to down-select from the strongly correlated primary descriptors. This resulted into two highly correlated clusters of
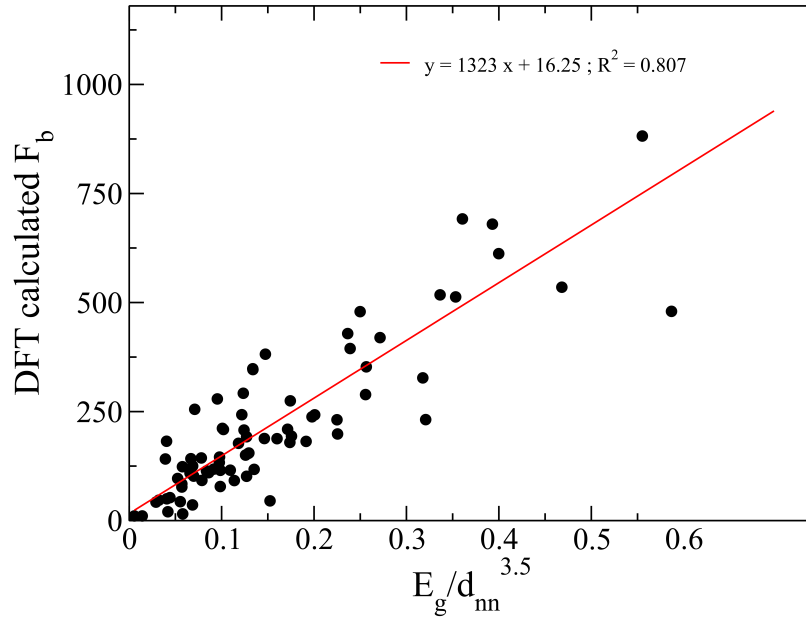
Figure A2.2: F_b vs. $E_g/d_{nn}^{3.5}$ plot. Linear regression is performed to obtain the parameters a and b in Equation 3.3 of the main manuscript. For 78 compounds (ignoring outliers LiF, MgO, BN and C) we obtain a model with $R^2 = 0.807$. The positive intercept of the model, makes the model physically consistent ($F_b \geq 0$).
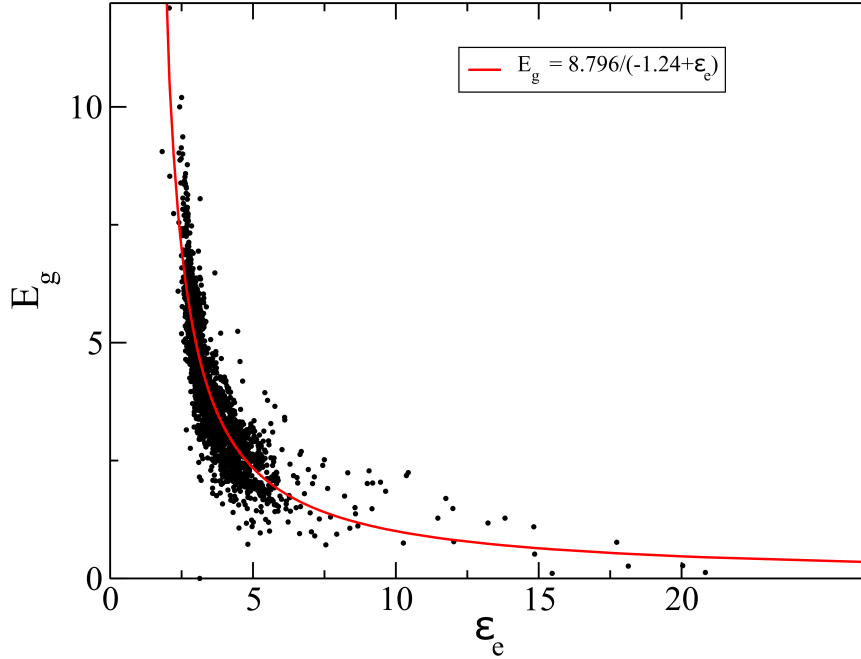
Figure A2.3: E_g vs. ε_e plot for 3277 dielectrics. The inverse relationship between E_g and ε_e looks general after testing this relation for such a large number of dielectrics. The data have been taken from data repository [72] http://khazana.uconn.edu.
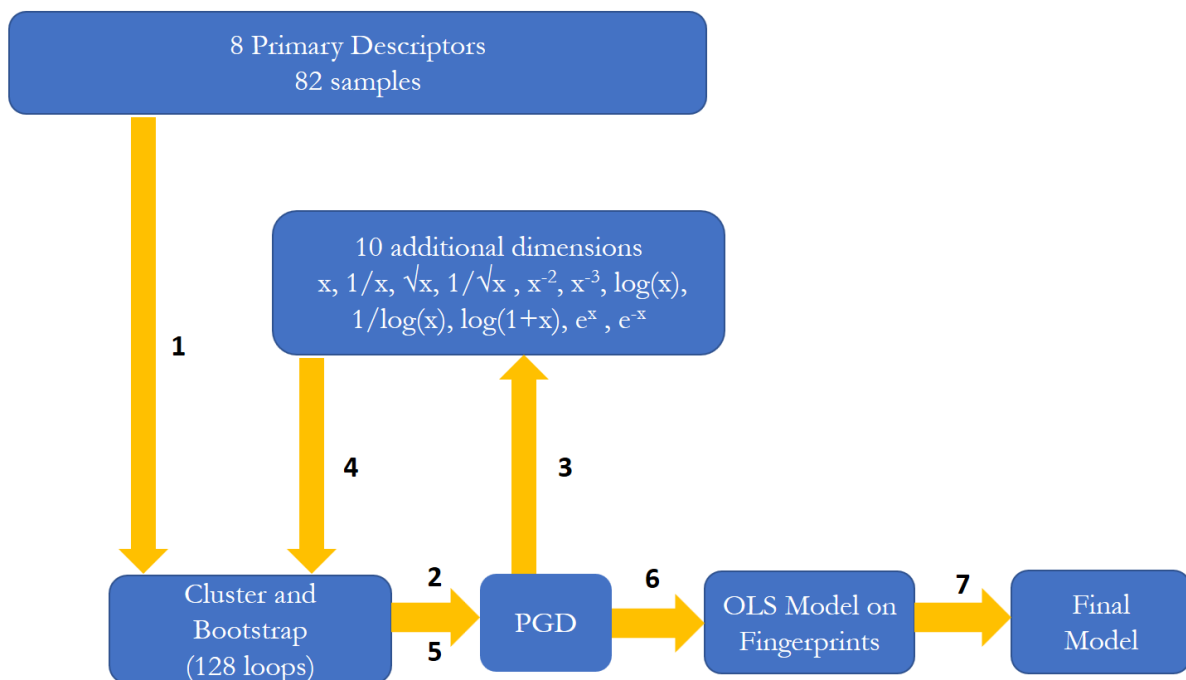
Figure A2.4: Schematics of the BoPGD workflow employed to downselect primary descriptors, create compound descriptors from the downselected primary descriptors to obtain eq 2.1 in main manuscript.

descriptors– (i) $\{B, d_{nn}, \omega_{max}, \omega_{mean}\}$ and (ii) $\{\varepsilon_e, E_g\}$. We, then select one descriptor at random from these clusters (B, E_g) to create the compound descriptors employing various polynomial, rational and exponential functions (see Figure A2.4). These compound descriptors were then reclustered and down-selected. A linear relationship between the down-selected compound descriptors and the KPI was derived and this model could explain about 87.2% of the variance in the value of breakdown strength (see eq 2.1 in the manuscript).
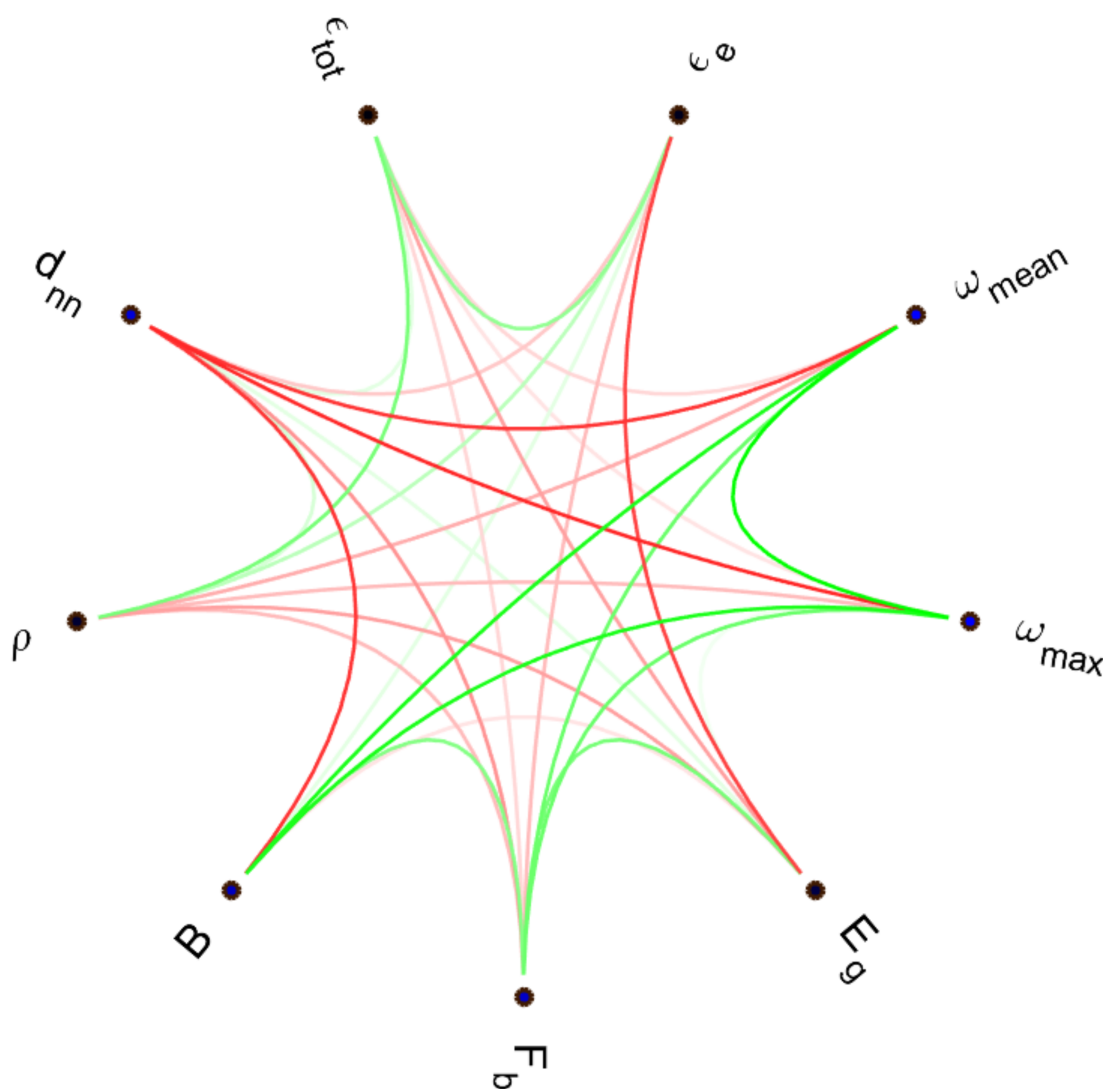
Figure A2.5: Schemaball diagram showing pairwise descriptor correlations. Green lines denote positive correlations between descriptors and red lines denote negative correlations. Brighter the line, stronger the correlation.
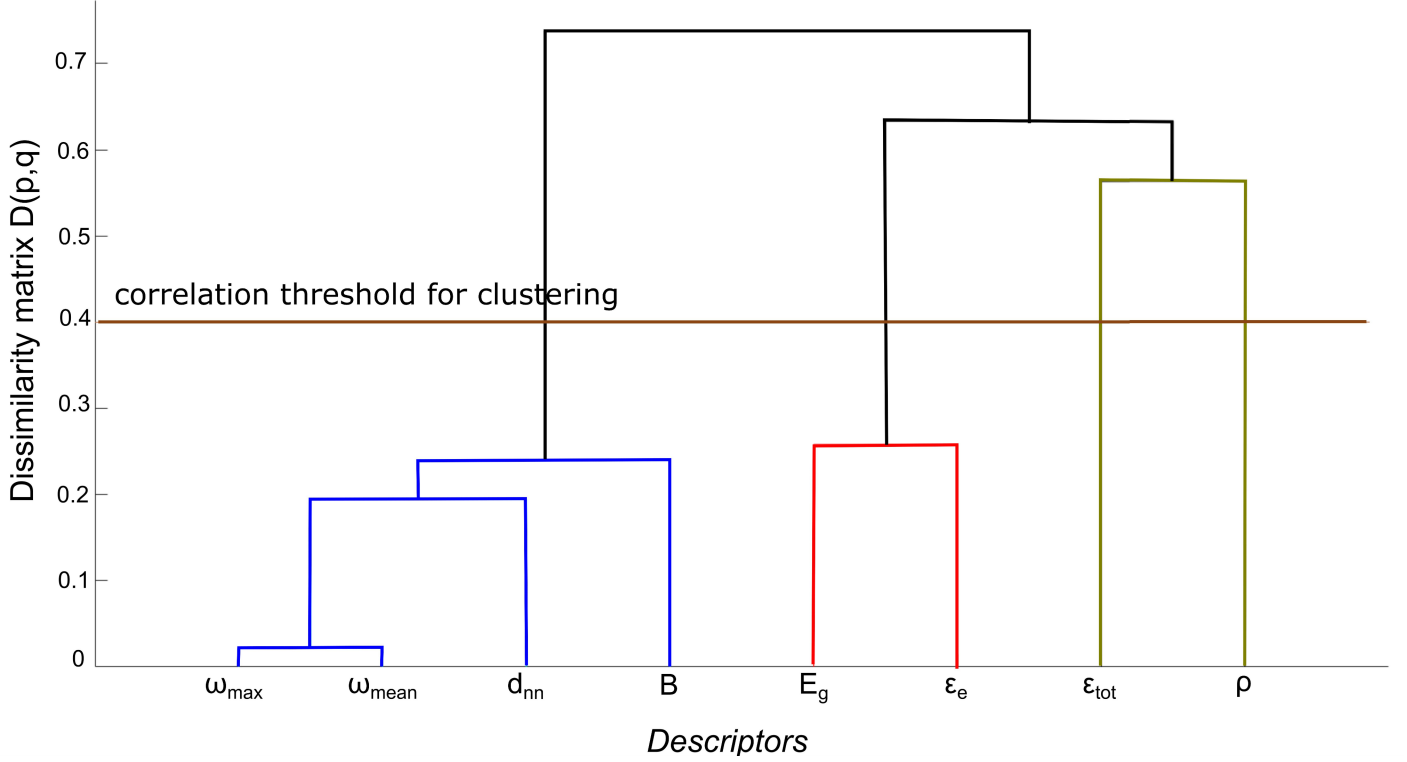
Figure A2.6: Dendrogram that visualizes the agglomerative hierarchical clustering (AHC) of the eight descriptors employed in this work. A cutofff value of $\hat{\rho}\left(\boldsymbol{X}^{(p)}, \boldsymbol{X}^{(q)}\right) \geq 0.6$ (or alternatively $(D(p,q) \leq 0.4)$) is employed. This results in four clusters. The first cluster comprising of phonon frequencies (ω_{max}, ω_{mean}), bulk modulus (B) and nearest-neighbor distance (d_{nn}). The second cluster comprises of electronic part of dielectric constant (ε_e) and bandgap (E_g). The mass density (ρ) and total dielectric constant (ε_{tot}))are treated as separate clusters.

Table A2.1: Comparison of the ML predicted dielecteric breakdown fields with DFT computed breakdown field for 10 new materials which were not the part of the dataset on which model was developed.

Dielectric	DFT computed [129, 83, 92] F_b (MV/m)	BoPGD+ (eq 2.3) predicted F_b (MV/m)	Kim model [83] predicted F_b (MV/m)
$BaSnO_3$	259.7	302.6	231.6
$CaGeO_3$	401.3	444.4	303.3
$CaSiO_3$	833.9	1131.7	1062.7
$BSiO_2F$	1507.0	1325.5	2497.3
$BaBO_2F$	623.6	2360.8	5038.9
$SrBO_2F$	1491.4	2611.7	5977.2
Li_2S	462.5	232.0	260.9
Na_2S	132.7	91.2	89.8
$SrCl_2$	293.4	216.3	195.9
ZrO_2	1253.0	612.5	874.1

Chapter 3

Towards Machine Learning Model of Proton Conductivity in Perovskite Oxides

3.1 Introduction

Fuel cell technology shows great promise in converting the chemical energy of hydrocarbon fuels into electricity without generating air pollutants [93]. Similar to a battery, a fuel cell comprises of cathode and anode separated by an electrolyte. However, unlike a battery, it doesn't require recharging and instead relies on a continuous supply of a specific fuel for ongoing electrical generation. The fuel such as H_2 is fed to the anode and gets oxidized to H^+, releasing electrons to the external circuit and producing a direct current. The H^+ species produced at the anode traverse through the proton conducting electrolyte to recombine at the cathode with oxygen and electrons (came through the external circuit) to release water as a byproduct [93], see Figure 3.1. In solid oxide fuel cell [94], the solid electrolyte is a proton (or oxide ion) conducting ceramics that are compact in size, safe, and thermally stable [95].

Proton conduction in perovskite oxides is a complex phenomenon. In solid-state materials, protons (H^+) diffuse through a hopping process from one lattice site to another governed by Grotthuss mechanism [13]. Developing a machine learning (ML) model for predicting proton conductivity in perovskite oxides can identify important descriptors relevant to proton conduction which in turn will help us to accelerate the discovery/synthesis of a better proton conductor. Machine learning techniques leverage patterns and relationships within data to

make predictions. For example, Liu Xu et al. [134] find that the ratio of O–O charge population to their separation distance shows a quadratic relationship with the logarithm of oxide-ion conductivity in ABO_3 perovskites.

To create such a model for proton conductivity, we do an extensive literature survey to collect a comprehensive list of ABO_3 perovskites that exhibit proton conductivity. Then, we compute the proton diffusion energy barriers in them and look for the Nernst-Einstein equation [93] to estimate proton diffusivity. We also list the important descriptors encompassing structural, chemical, and thermodynamic properties relevant to influence proton conduction [135, 134, 136, 137]. Based on the size of the dataset, a suitable ML algorithm can be chosen to train a model that establishes the relationship between the input features and the (target property) proton conductivity. We have outlined our ML framework in Figure 3.6.
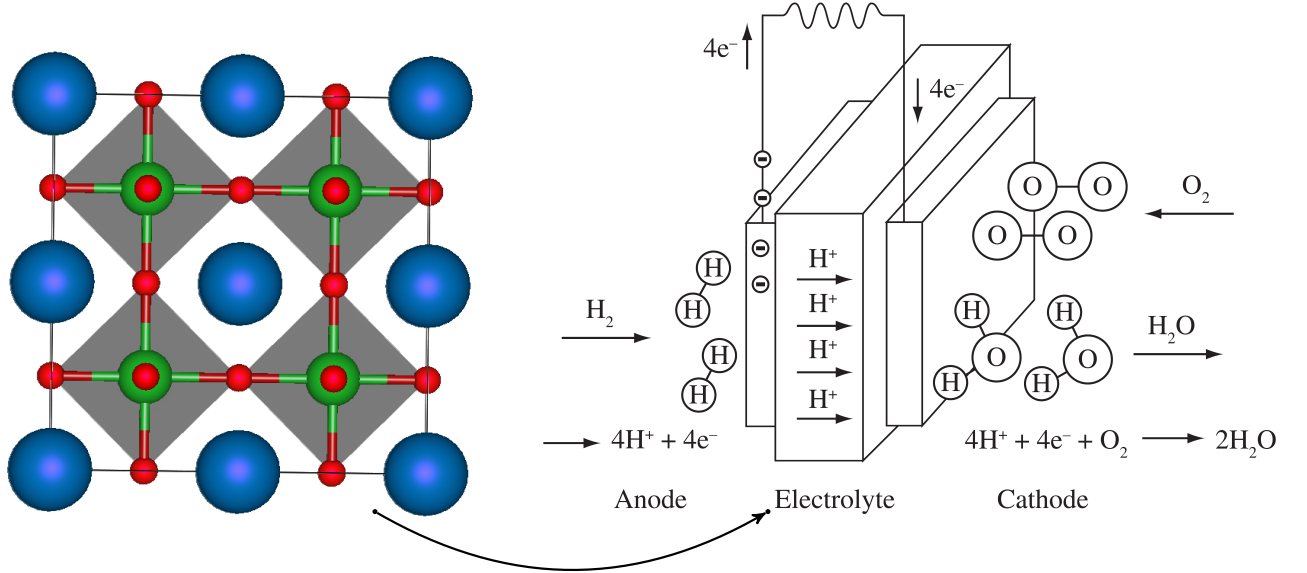
Figure 3.1: Workflow of proton conducting perovskite oxide-based electrolyte containing fuel cell (the right figure has been adapted from ref [93]). The input fuel at anode is pure H_2 gas and the byproduct of full cell reaction is water.

3.2 Computational details

We insert one H-atom near an oxygen site within $2 \times 2 \times 2$-size supercell of cubic perovskite unit cell (hence total 41 atoms) and perform ionic relaxation within the density functional theory (DFT) method using the Quantum ESPRESSO computational package [138]. We used a generalized gradient approximation (GGA) [139] within Perdew-Burke-Ernzerhof [140] parameterization of electronic exchange-correlation energy functional. The interaction between

ionic core and valence electrons is modelled using ultrasoft pseudopotentials [141]. The energy cut-offs of 40 Ry for wave functions and 320 Ry for charge density were taken to truncate the plane wave basis sets used to represent Kohn-Sham (KS) wave functions. Uniform meshes of $3 \times 3 \times 3$ k-points were used in sampling integrations over the Brillouin zone of the supercell. Using Hellmann-Feynman forces and Broyden Fletcher Goldfarb Shanno (BFGS) scheme, the supercell is relaxed till the force components on each atom $\vec{F}$ become less than 10^{-3} Ry/Bohr. Total energy was converged within 10^{-8} Ry to achieve electronic self-consistency. Fermi-Dirac distribution with a width of $k_{\mathrm{B}}T = 0.002$ Ry is used for smoothening the discontinuity in occupation numbers of electronic states.

We follow the Grotthuss mechanism [13] of proton transfer in which the hydrogen bond O$\cdots$H reorients itself to get closer to the nearest oxygen atom and then H diffuses by hopping to that oxygen atom. We estimate the associated barrier and transition pathway of proton transfer through the climbing image nudged elastic band (CI-NEB) method [142]. Seven or more images (intermediate configurations) have been considered to trace the transition pathway between two chosen equilibrium configurations in the CI-NEB calculations. All the transition states were fully relaxed until the Hellmann–Feynman forces acting on the atoms were within 0.05 eV/Å.

We apply the Arrhenius equation ($k(T) = A \exp(-E_a/k_{\mathrm{B}}T)$) to estimate the proton transfer rate $k(T)$ within perovskite oxide lattice. Transition state theory [143] determines the Arrhenius factor (A) as the ratio of the product of phonon frequencies at transition state (TS) to that of equilibrium (reactant) state configuration excluding one imaginary frequency at TS. For $2 \times 2 \times 2$-size supercell of ABO_3 containing one H-atom, we have to estimate phonon calculation of 41 atoms which is computationally very expensive due to $O(N^4)$ scaling. Following the work of N. Bork et al. [136], we have frozen some atoms which are far from H-atom. Only atoms in the vicinity of the H-atom have been allowed to move in the phonon calculation. Out of 41 atoms, only 23 atoms were allowed to move and hence 23×3 = 69 representations were considered in the phonon calculation at Γ-point of the Brillouin zone of the supercell. We employ density functional perturbation theory (DFPT) scheme [144] to estimate the phonon frequencies and encounter several imaginary frequencies due to cubic configurations of ABO_3 which are often metastable at $T = 0$ K.

3.3 Results & Discussions

3.3.1 Proton conducting perovskite oxides

Perovskite oxides are high-temperature proton conductors at which their structures are cubic of spacegroup $Pm\bar{3}m$. In Table 3.1, we list a few proton-conducting perovskite oxides through an extensive literature survey and following the book written by T. Ishihara [94]. Typical proton-conducting perovskites are yttrium-doped $BaCeO_3$, $SrCeO_3$, and $BaZrO_3$ [145].

Here, we study cubic perovskite oxides (listed in Table 3.1) with 2.43% H-atom concentration (one H-atom in $2 \times 2 \times 2$-size supercell of ABO_3) to understand the diffusion mechanism and relevant descriptors of proton conductivity. We idealize the H-atom as a proton or H^+ which weakly binds with oxygen-atom through a hydrogen bond. Although quantum diffusion of H-atom occurs predominantly due to tunnelling motion [146, 147], we restrict our analysis to classical diffusion through a thermally activated Arrhenius-type form [93] which parameters (A and E_a) have been evaluated by quantum mechanical calculations [136]. The transition state theory [143] needs phonon calculation to estimate the Arrhenius factor (A), and the climbing image nudged elastic band method gives the activation energy barrier (E_a).

Table 3.1: Proton conducting perovskite oxides listed from the book "Perovskite oxides for solid oxide fuel cells" written by T. Ishihara [94] and the references therein.

$BaCeO_3$	$CaTiO_3$	$KTaO_3$
$BaZrO_3$	$CaMnO_3$	$PbTiO_3$
$BaTbO_3$	$LaAlO_3$	$PbZrO_3$
$BaThO_3$	$LaBO_3$	$SmNiO_3$
$BaTiO_3$	$LaGaO_3$	$SrCeO_3$
$BaNbO_3$	$LaScO_3$	$SrTiO_3$
$BaSnO_3$	$LaErO_3$	$SrZrO_3$
$BaHfO_3$	$LaYO_3$	$SrNbO_3$
$CaZrO_3$	$LiNbO_3$	——

3.3.2 Activation energy barrier of proton transfer in perovskite oxides

Proton transfer is a thermally activated process that occurs at a high temperature. In a solid, the proton conducts fast due to the Grotthuss process which involves H-hopping through hydrogen bond network [13, 148]. The Grotthuss mechanism of proton transfer constitutes two activation energy barriers. In the first step, the hydrogen bond $O \cdots H$ rotates to get closer to another oxygen in which a rate-determining barrier of E_{rot}^{OH} has to be crossed. In the second step, when the H-atom gets aligned with another oxygen atom it hops by breaking the earlier hydrogen bond and creates a new one. The second step often requires a larger activation energy E_{hop}^{H} than E_{rot}^{OH} as it follows by bond-breaking phenomenon.
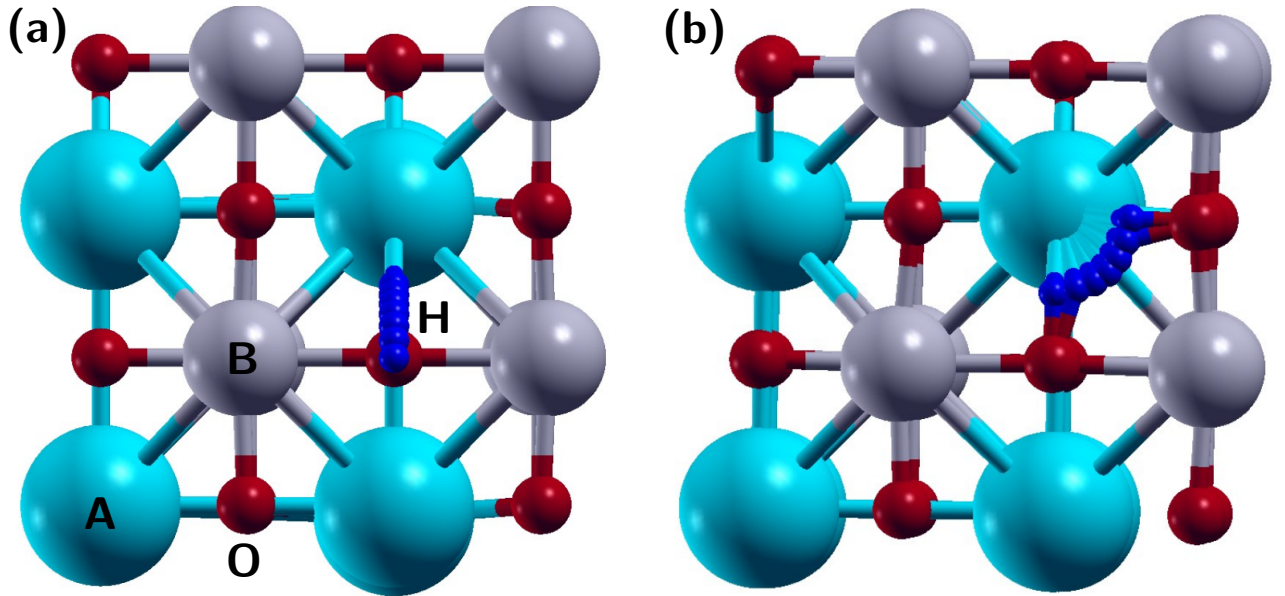
Figure 3.2: Proton (blue) transfer pathways in ABO_3 compounds through Grotthuss process. (a) First, OH orients itself (shown here only the H-atom of several images of NEB calculation) to get closer to another oxygen atom, and then (b) H hops to the nearest O-atom. This completes the one instance of proton diffusion and it continues to traverse a proton from one electrode to another through an electrolyte ABO_3 within the fuel cell.

We use the Nudged Elastic Band [142] method to estimate proton hopping and OH rotation barrier in a few perovskite oxides (see Table 3.2). We introduce one hydrogen atom (idealized as a proton) near an oxygen site and rotate the OH-bond to get closer to another nearest oxygen site for hopping. These two configurations are regarded as reactant and product states for the OH-rotation process. Next, we determine the binding site for H-atom around the nearest oxygen atom at which the jump is to be completed to trace an H-hopping pathway. In Figure 3.2, we show one such instance of proton transfer in ABO_3 compound (shown for BaTiO$_3$) from one
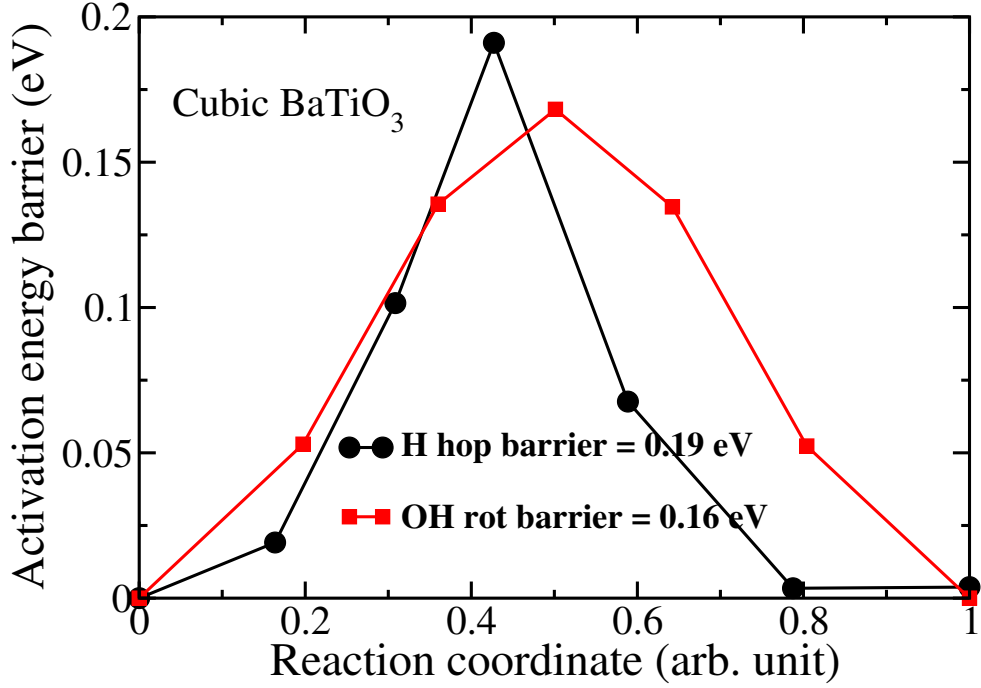
Figure 3.3: Activation energy barriers of OH-rotation (E_{rot}^{OH}) and H-hopping (E_{hop}^{H}) in cubic BaTiO$_3$ estimated through CI-NEB method. The relative energy of the saddle point configuration (i.e. the highest energy one) to the initial (reactant) configuration gives the activation energy barrier. The corresponding configurational pathways have been presented in Figure 3.2.

oxygen site to the nearest one. The corresponding energy barrier profiles of OH-rotation and H-hopping in BaTiO$_3$ have been presented in Figure 3.3. Both barrier profiles in BaTiO$_3$ are Gaussian-like curves, but the OH-rotation energy landscape within CaTiO$_3$ draws a double-well potential curve (see Figure 3.4). The activation energy barrier (the difference in energies between transition and equilibrium reactant state) in the double-well potential is measured from the well to the top of the energy surface. In both BaTiO$_3$ and CaTiO$_3$, we note that $E_{rot}^{OH} < E_{hop}^{H}$ as expected. We list OH-rotation and H-hop energy barriers in Table 3.2 for a few perovskite oxides. We observe that the H-hop barrier profile is always a Gaussian curve but the OH-rotation energy landscape contains multiple valleys in a few cases. The appearance of multi-valleys in the OH-rotation energy landscape refers to the presence of several binding sites around a given oxygen atom within ABO_3 perovskites.

3.3.3 Transition state theory

As we have estimated the activation energy barriers of proton transport within ABO_3 compounds, we now turn to determine the proton transfer rate at temperature T. According to the famous

Table 3.2: We estimated OH-rotation ($E_{\text{rot}}^{\text{OH}}$) and H-hopping barrier ($E_{\text{hop}}^{\text{H}}$) in a few cubic perovskite oxides. As expected, $E_{\text{hop}}^{\text{H}}$ is greater than $E_{\text{rot}}^{\text{OH}}$.

Perovskite	$E_{\text{rot}}^{\text{OH}}$ (eV)	$E_{\text{hop}}^{\text{H}}$ (eV)
$BaTiO_3$	0.16	0.19
$BaNbO_3$	0.12	0.25
$BaSnO_3$	0.16	0.35
$BaHfO_3$	0.15	0.28
$CaTiO_3$	0.15	1.77
$CaMnO_3$	0.23	1.58
$KTaO_3$	0.21	0.35
$LaGaO_3$	0.19	$\cdots$
$PbTiO_3$	0.09	0.28
$PbZrO_3$	0.13	$\cdots$
$SrTiO_3$	0.16	0.33
$SrNbO_3$	0.10	0.41
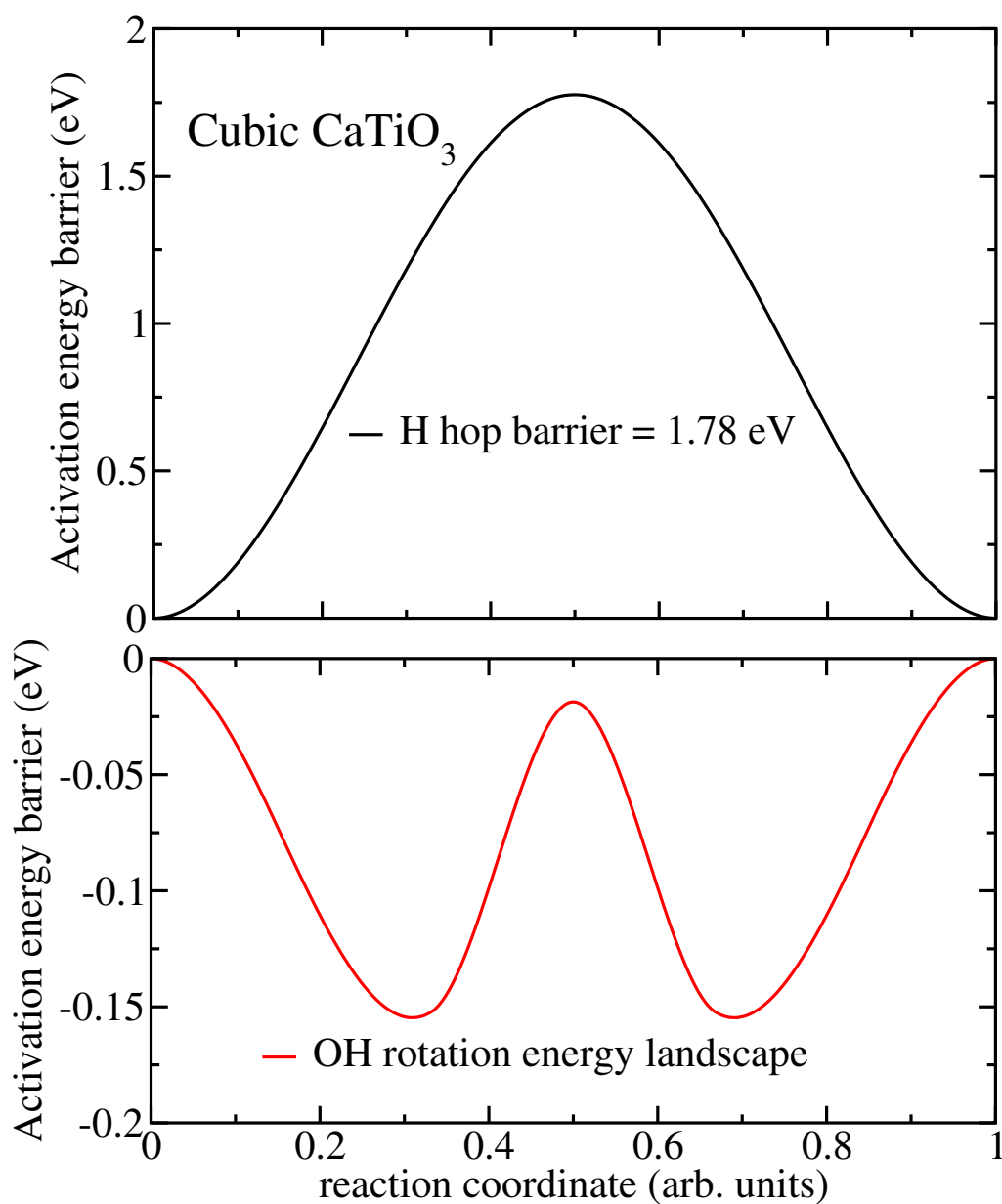
Figure 3.4: Activation energy barriers of (top) H-hopping (E_{hop}^{H}) and (bottom) OH-rotation (E_{rot}^{OH}) in cubic CaTiO$_3$. Configurational energies in H-hop trace a Gaussian profile with the progress of the reaction (reaction coordinate), while OH-rotation traces a double-well potential. The double-well barrier profile means that our initial configuration itself is at the saddle point or transition state and the valleys represent reactant and product states.

Arrhenius equation, the rate constant ($k(T)$) of a reaction reactant→product is given by

$$k(T) = A \exp\left(-\frac{E_a}{k_\mathrm{B}T}\right)$$

Where A is a proportionality constant (known as Arrhenius factor or pre-exponential factor) and E_a is the activation energy barrier to overcome to finish the reaction. In Figure 3.5, we show the typical energy barrier of a reaction (for example, OH-rotation in ABO_3) in which the peak energy (i.e. transition state) configuration is of great interest because its energy controls the rate of a reaction.
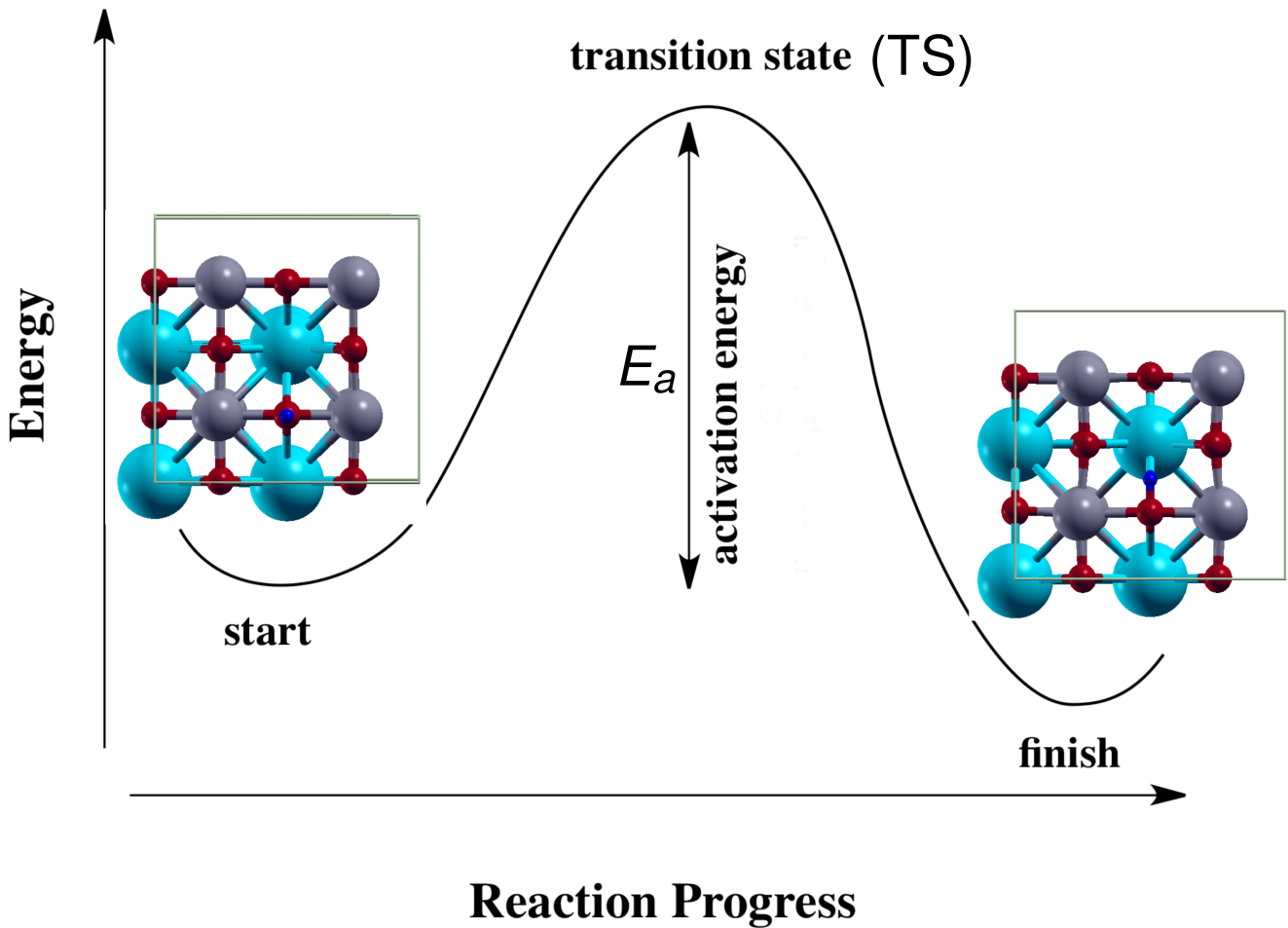
Figure 3.5: A typical energy barrier profile of a reaction reactant→product. In the proton transfer mechanism, the configurational change of hydrogen (or proton) creates two such states (reactant and product) after overcoming an activation energy barrier (E_a).

Transition state theory [143] estimates the pre-exponential factor within the harmonic approximation as follows:

$$A = \frac{\prod \nu_{\mathrm{initial}}}{\prod \nu^\dagger{}_{\mathrm{TS}}}$$

i.e. the ratio between the product of vibrational frequencies of the initial state (should be a local minimum), v_{initial}, and the vibrational frequencies of the transient state, v_{TS}. Here, † indicates that one imaginary phonon frequency that will appear at the transition state has been dropped in the equation. Therefore, under harmonic approximation transition state theory (TST), the Arrhenius equation gets modified to

$$k(T) = \frac{\prod v_{initial}}{\prod v^{\dagger}_{TS}} \exp\left(-\frac{E_a}{k_{\mathrm{B}}T}\right) \tag{3.1}$$

We have considered $2 \times 2 \times 2$ supercell of perovskite structure unit cell and one hydrogen atom has been introduced into the supercell to study the proton transport behavior. We expect (see Figure 3.5)

- at local minimum, all the phonon frequencies be real and positive since $\partial^2 V/\partial x_\alpha \partial x_\beta > 0$ and

- at a local maximum, only one of the phonon frequencies be imaginary along a particular vibrational eigenmode since $\partial^2 V/\partial x_\alpha^2 < 0$.

Instead of only one imaginary phonon frequency, we are encountering multiple imaginary frequencies at the transition state. Phonon instabilities are present even in the equilibrium (reactant or product state) configuration because these cubic perovskites are high-temperature structures that undergo a structural transition to a lower symmetry configuration at a lower temperature. The consideration of cubic perovskites in our study is relevant as the fuel cell technology operates at high temperatures where thermally activated proton transfer becomes feasible.

3.3.4 ML framework and descriptors of proton conductivity

In machine-learning (ML) modelling, we require a set of descriptors or features that influences a target property. The pairwise correlation estimation gives the strength of the influence of a quantity on another. Among the chosen descriptors, a pair of descriptors may display a strong correlation which should be taken care of by dropping one as one may find the functional dependence such as a power law relationship between the two [85]. Dimensional analysis can also help in identifying physically meaningful features consistent with the target property [85].

To enhance the list of descriptors, we can apply simple mathematical operations (which might be nonlinear too) on the primary descriptors to generate additional descriptors (see refs [83] and [85]). Now, to downselect the fingerprint descriptors, we can use a feature reduction algorithm such as BoPGD [120, 124] described in chapter 3 of this thesis.

In this study, we aim for an ML model of proton diffusivity which can be further used to explore/predict an excellent proton conductor. The proposed ML framework and the relevant descriptors of proton diffusion have been charted in Figure 3.6. We discuss below briefly about these descriptors and their relevance to proton conduction in ABO_3 perovskites.

- Hydration enthalpy: For proton transport, the electrolyte ABO_3 should be hydrated. The hydration enthalpy measures the extent of solvation of H^+ ions in the electrolyte [148, 135, 137]. It also shows the bond strength between oxygen and H-atom.

- Tolerance factor: It is a structural descriptor whose value determines the crystal structure of a perovskite oxide. It follows from the geometrical packing of metallic elements A, B, and oxygen atoms. Mathematically, Goldschmidt tolerance factor is given as

$$t = \frac{r_A + r_O}{\sqrt{2}(r_B + r_O)},$$

  where r_α is the radius of atom α. For ideal cubic perovskite oxide, the tolerance factor is 1. The deviation of t from 1 marks the structural distortions that impact the pathways and energetics of proton transport.

- Lattice energy: It is the energy released when the individual atoms assemble to form the lattice. It has been observed that the lower lattice energy perovskite oxides are superior proton conductors (see Table 1 of ref [135]).

- O-H binding energy: It should be moderate to allow sufficient H^+ concentration [136, 149]. O-H binding energy negatively correlates with activation energy barriers of proton transfer in ABO_3 perovskites [136].

- O-O neighbor distance: A shorter O-O distance enhances the proton transfer rate as it decreases the activation energy barrier of H-hopping [134].

- $\chi_B - \chi_A$: T Norby et al. [150] noted the correlation between hydration enthalpy and

electronegativity difference between atoms *A* and *B*, i.e. $\Delta H \propto \chi_B - \chi_A$. This correlation makes one of these two redundant from an ML perspective. The estimation of ΔH is difficult, while the electronegativity values are trivial and often tabulated in a textbook.

- Unit cell free volume: A larger unit cell volume favors a higher hydrogen content in ABO_3[151].

- Ionic radii of *A* and *B*: These control the tolerance factor (*t*) and electronegativity difference $\chi_B - \chi_A$.

We can create additional descriptors by applying various mathematical transformations to the above-listed ones.

3.4 Conclusions and future directions

In summary, we have proposed an ML framework with relevant descriptors of proton conductivity. We listed 26 proton-conducting perovskite oxides in Table 3.1, and estimated proton migration activation energy barriers in a few of them. In the future, we want to enhance the sample space of perovskite oxides to make ML modelling meaningful.

To resolve the appearance of imaginary phonon frequencies (which are not an error of density functional theory as we are simulating cubic perovskites at zero temperature), we can look for machine-learning interatomic potential to run molecular dynamics simulations at elevated temperatures. We can also include zero-point energy and quantum tunneling effect if *ab initio* path-integral-based molecular-dynamics simulation [147, 149] is set up.

A machine learning algorithm for a small dataset is often regression-based such as LASSO [120] (least absolute shrinkage selection operator) and GPR [152] (Gaussian process regression) models. The advantage of regression-type modelling is that we get a closed-form predictive model which is easy to interpret. Such a model will help us identify the crucial descriptor of proton conductivity which can be used for the discovery of a better proton conductor.
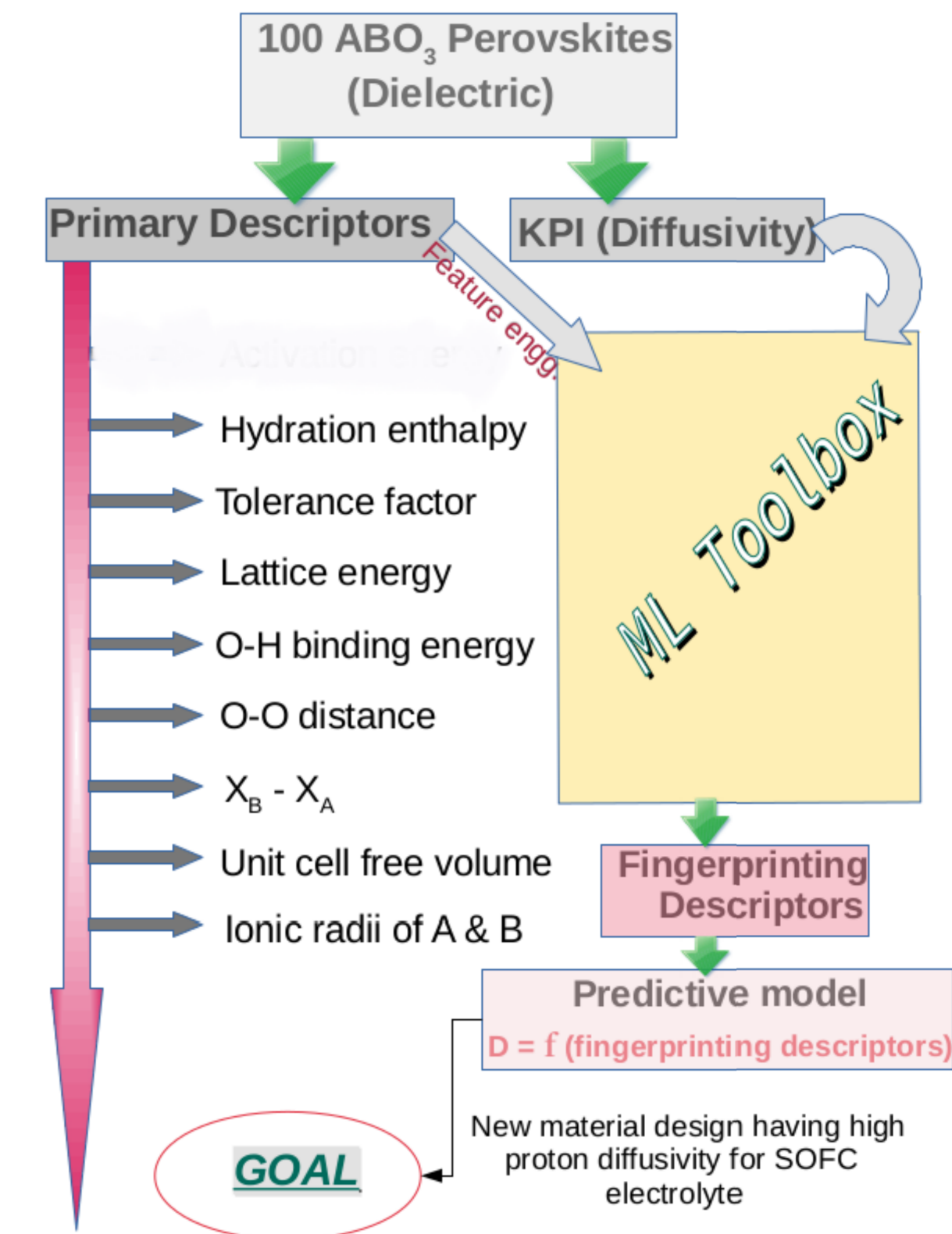
Figure 3.6: Proposed machine learning framework and list of relevant descriptors to proton conductivity in perovskite oxides.

Part II

High-Entropy Alloys

Chapter 4

Entropic Stabilization and Descriptors of Structural Transformation in High-Entropy Alloys

4.1 Introduction

Alloying has been central to the progress of human civilization since the Bronze age. In conventional alloys, small amounts of secondary elements are mixed with primary ones. The resulting alloy is named based on the primary element like ferrous, aluminum, copper, and nickel alloys. The last two decades [25, 26, 153, 43, 29, 30, 154] have witnessed an unconventional method of alloy design with equiatomic mixing of four or more elements. Stability of such alloy is assumed to be dominated by configurational entropic contributions, and hence they are named high-entropy alloys (HEAs). Beginning with the work of Yeh et al. [25] and Cantor et al. [26], HEAs have stimulated intense research to develop understanding of their phase stability and superb mechanical behavior [153, 43, 29, 30, 32].

Four *core effects* [42] govern the stability and behavior of HEAs: (1) high configurational entropy of mixing attributed to stabilizing solid solution phase, (2) severe lattice distortions due to mismatch in the chemistry of alloying elements, (3) sluggish diffusion kinetics, and (4) emergence of exceptional properties due to mutual interactions among randomly distributed atoms (known as cocktail effect). While the enhanced configurational entropy lowers the Gibbs

49

free energy, it is not the sole factor responsible for forming a single-phase (if at all) solid-solution [155, 156, 157] in preference to competing phases such as intermetallics, precipitates, multiphase, and amorphous structures [158, 159, 40]. It is implicitly evident from the existence of limited single-phase solid-solution HEAs.

According to Hume-Rothery rules [160], a substitutional solid-solution forms if the constituent mixing elements have similar atomic sizes (radii difference $\leq$ 15%), electronegativities, valencies, and the same crystal structure. These empirical rules are the design principle of binary alloys, but their applications to HEAs encounter some complications and exceptions. For example, the formation of single-phase (FCC) Cantor alloy [26] with constituent elements of different crystal structures is against one of these rules. Researchers still use the size and electronegativity difference rules to design single-phase solid solution HEAs [156, 161, 162], with marked deviations from the ideal lattice structure [163]. These structural deviations, termed internal lattice distortions (ILDs), are the combined effect of the size mismatch, differences in constituent elemental crystal structures and their valencies, and bond-heterogeneities among mixing elements.

In this work, we demonstrate that the BCC structure of $Nb_x(HfZrTi)_y$ gets stabilized with increasing Nb-concentration, marking an HCP→BCC transition. We show that the associated structural changes and variation in average number of valence electrons with the addition of Nb result in large fluctuations in ILDs. Through comparative analysis of Gibbs free energy of quaternary HEAs $Nb_x(HfZrTi)_y$ and $Nb_aMo_bW_cTa_d$, we find that the entropy stabilizes the former while the enthalpy of formation ensures the stability of the latter.

4.2 Computational details

We use special quasirandom structures (SQS) [164, 165, 166] of HEAs to approximately model their chemical disorder. For each alloy, we generate SQS with $3\times3\times2$ periodic supercell (36 atoms) of the conventional unit cells of BCC or HCP structures (see Appendix for SQS details). We considered BCC and HCP host lattices of $Nb_x(HfZrTi)_y$ alloys and only the BCC lattice of $Nb_aMo_bW_cTa_d$. As the reference ideal solid solution for comparison, we chose SQS of completely miscible BCC Mo_pW_q alloys for which the heat of mixing at any composition vanishes [167, 168]. Lattice parameters of SQS configurations were estimated using Vegard's

law [169], which were optimized through structural relaxation to an energy minimum.

We perform full structural relaxation of these model SQS within the density functional theory (DFT) methods incorporated in the Quantum ESPRESSO package [138]. We used a generalized gradient approximation (GGA) [139] and Perdew-Burke-Ernzerhof [140] functional of electronic exchange-correlation energy. We preferred GGA over local density approximation (LDA) due to its closer estimate of lattice parameter (3.428 Å, this work) of BCC NbHfZrTi to the experimental one (3.444 Å) [170, 171, 35], in contrast with LDA estimated 3.345 Å (this work). We employ projector augmented wave potentials [172] and represent the electronic wave functions and charge density with plane wave basis sets truncated at energy cutoffs of 60 Ry and 500 Ry respectively. Uniform meshes of $3 \times 3 \times 4$ and $3 \times 3 \times 3$ k-points were used in sampling integrations over Brillouin zones of BCC and HCP-based supercells respectively. Using Hellmann-Feynman forces and Broyden Fletcher Goldfarb Shanno (BFGS) scheme, each alloy SQS is relaxed till the force components on each atom $\vec{F}$ becomes less than 10^{-3} Ry/Bohr. Total energy was converged within 10^{-8} Ry to achieve electronic self-consistency. Fermi-Dirac distribution with a width of $k_{\mathrm{B}}T = 0.002$ Ry is used for smoothening the discontinuity in occupation numbers of electronic states.

We use the Debye model to estimate vibrational entropy. The Debye temperature (θ_{D}) of each alloy SQS was extracted from their elastic moduli matrix obtained from the thermo_pw package [173]. θ_{D} is used as a single parameter within Debye model to estimate the vibrational entropy of each alloy.

To analyze the local structure of relaxed SQS lattices of HEAs, we investigate (a) the nearest-neighbor bond alignments of each atom through bond-orientational order parameters using a recently developed python library *pyscal* [174], and (b) geometric features of the Voronoi cell constructed around each atom using *Voro++* library [175] for Voronoi analysis.

4.3   Results and Discussion

Our motivation for analysis of the relative stability of BCC and HCP structures of $Nb_x(HfZrTi)_y$ comes from the distinct crystal structures taken by its constituent elements at ambient conditions: Nb occurs in BCC structure, and Hf, Zr, and Ti occur in HCP structure. Secondly, Hf, Zr, and Ti

undergo structural transformation to BCC structure at high temperature from their stable low-temperature HCP structure [176].

In the periodic table, elements {Hf, Zr, Ti} belong to group 4, and Nb belongs to group 5. A. R. Natarajan *et al.* [177] studied 36 refractory binary alloys formed by elements of groups 4, 5, and 6 and classified their phase diagrams into six distinct types (see Figure 14 of [177]). They show that group 4 elements respond very differently from groups 5 and 6 under tetragonal distortion. The strain energy surface peaks at the BCC phase for group 4 elements, while for group 5 and 6 elements dip at the BCC phase (see Figure 4 and 5 of [177]). When elements of groups 4 and 5 are mixed together, the resulting alloy will have a narrow region of HCP, and the remaining region is BCC solid solution on the binary phase diagram. These observations from refractory binary phase diagrams help understand the phase stability in HEAs.

Experimentally, the equiatomic NbHfZrTi alloy occurs in the BCC structure [170, 171, 35]. Our calculations (Figure 4.1(a)) also support this as we find that at equiatomic and higher Nb-concentrations, SQS of $Nb_x(HfZrTi)_y$ of BCC lattice is more stable than that of HCP lattice. We find this structural preference in randomized structural models as well. With increasing Nb-concentration, Zhang et al. [178] report $\omega (P6/mmm) \rightarrow$ BCC transformation rather than HCP $(P6_3/mmc) \rightarrow$ BCC, which poses the question of the structure of low Nb-concentration $Nb_x(HfZrTi)_y$ alloys. To address this, we simulated a few SQS models of $(HfZrTi)_{12}$ considering HCP and ω lattices, and found that SQS on the HCP lattices were more stable than those on the ω ones (see Appendix Table A4.1 and Appendix Figure A4.2) by more than 15 meV/atom. Thus, we analyze here HCP to BCC transformation.

In Figure 4.1(a), we report a structural transformation equiatomic composition of $Nb_x(HfZrTi)_y$ based on the relative DFT energies of SQS corresponding to HCP and BCC lattices. We find significant changes in the atomic positions of relaxed SQS from their ideal lattice structure; thus, ILDs help lower the energy. As these atomic displacements developed during relaxation severely distort the ideal lattice, we require local structural descriptors to ascertain the true phase of relaxed HEAs. At nonzero temperature, any crystalline material exhibits dynamic ILDs due to thermal vibrations. However, heterogeneous static displacements (i.e. ILDs) are present in HEAs even at $T = 0$ K due to differences among their atomic constituents. In a recent study [179], root mean squared displacement of atoms in BCC structure of NbHfZrTi at $T = 0$ K

was estimated at 9% of its lattice parameter. Such large ILDs make identification of the lattice structure challenging. X-ray diffraction (XRD) measurement averages out these displacements and does not show any significant peak broadening, but the intensity of Bragg peaks reduces due to diffused scattering by off-lattice atoms [163, 180]. The atom-resolved imaging techniques like transmission electron microscopy (TEM) facilitate observing the chemical ordering and ILDs in a medium-entropy alloy [181].

4.3.1 Local structure and identification of the underlying lattice

(a) Voronoi analysis   To examine the local structure at the atomic scale, we first use Voronoi decomposition involving the construction of a polyhedron around each lattice point (atomic site) known as Voronoi cell (or Wigner-Seitz cell in crystallography). Here, we construct Voronoi cells within $3\times3\times2$-size supercell considering periodic boundary conditions. ILDs differ from one supercell to another, but their distribution converges with large-size cells. This may result in a slight variation between the geometries of Voronoi cells drawn around each atom in two different-sized supercells of a given HEA. Since the atomic radii of constituent atoms in HEAs are similar, we treated each atom as a point particle in Voronoi decomposition. The Voronoi cell of a BCC lattice point is a *truncated octahedron* (see Figure 4.1(d)) that has 6 square and 8 hexagonal faces. The Voronoi cell of an HCP lattice point is a *trapezo-rhombic dodecahedron* (see Figure 4.1(e)) that has 6 trapezium- and 6 rhombus-shaped faces. The order of a vertex in a graph is the number of edges incident into it. Each Voronoi vertex of a BCC lattice is of order 3, which is topologically stable (type-**A**). In contrast, some Voronoi vertices of the HCP lattice are of order 4, which are topologically unstable (type-**B**). With a slight perturbation, topologically unstable vertices modify the Voronoi cell characteristics by creating new faces [103]. We demonstrate this for supercell of BCC and HCP lattices by adding random displacements to the positions of their lattice points. While the Voronoi cells of the BCC lattice does not evolve to have any new polygonal face, pentagonal and hexagonal faces appear in the Voronoi polyhedra of randomly perturbed HCP lattice originating at the unstable vertices of order 4 (see Appendix Figure A4.1(b)).

We use this feature of geometric instability of Voronoi vertices to identify BCC and HCP lattices of minimum energy SQS of $Nb_x(HfZrTi)_y$ alloys (see Table contained in Figure 4.1),

which exhibit significant ILDs. Voronoi cells with only quadrilaterals and hexagonal faces reveal that alloys with significant Nb-concentration ($x \geq 6$) optimize to a BCC lattice structure. We claim that at low Nb-concentration ($x = 0$ and 3), SQS optimize to HCP-based structures where pentagonal and hexagonal Voronoi faces originate at type-**B** Voronoi vertices due to ILDs.

(b) Bond-orientational order parameters We chose another class of structural descriptors called bond-orientational order parameters to confirm our claim of structural transition. The local bond-orientational order parameters (q_l) proposed by Steinhardt [104] reflect the symmetry of the local structure; and coordination number reveals packing within the lattice. For each atom, q_l is written in terms of spherical harmonics of θ_{ij} and ϕ_{ij} of orientational unit bond vectors joining neighboring sites i and j:

$$q_{lm}(i) = \frac{1}{n(i)} \sum_{j=1}^{n(i)} Y_{lm}(\theta_{ij}, \phi_{ij}) \Rightarrow q_l(i) = \sqrt{\frac{4\pi}{2l+1} \sum_{m=-l}^{l} |q_{lm}(i)|^2}, \qquad (4.1)$$

where $n(i)$ is the number of neighbor atoms around ith atom.

These local bond-orientational parameters are sensitive to the symmetry of the crystal and help identify simple phases such as BCC, FCC, and HCP. For different ideal crystals, q_l values are distinct except for q_l of odd l (see Appendix Table A4.2). ILDs or thermal noise disturb the crystal's local structure symmetry, and result in changes in q_l values and complicate the identification of the average lattice structure. Lechner and Dellago [99] showed that locally averaged $\bar{q}_l$s:

$$\bar{q}_{lm}(i) = \frac{1}{n(i)} \sum_{k=0}^{n(i)} q_{lm}(k) \Rightarrow \bar{q}_l(i) = \sqrt{\frac{4\pi}{2l+1} \sum_{m=-l}^{l} |\bar{q}_{lm}(i)|^2}, \qquad (4.2)$$

work better in identifying the Bravais lattice of distorted crystals (see Supplementary Figure A4.3). For an ideal lattice, $\bar{q}_l$ coincides with q_l, and the separation between the two measures the loss of structural order. In resolution of the lattice structure, here, we use $(\bar{q}_8, \bar{q}_{12})$ plane in which ideal BCC and HCP lattices are well separated at points (0.429, 0.405) and (0.317, 0.565), respectively.

In $(\bar{q}_8, \bar{q}_{12})$ plane (Figure 4.1(c)), relaxed SQS of $Nb_aMo_bW_cTa_d$ and Mo_pW_q alloys always fall on to the point representing BCC lattice structure. In $Nb_x(HfZrTi)_y$ alloys, SQS of HCP lattices with low Nb-concentration ($x = 0$ and 3) optimize to a structure that is close to the perfect HCP structure (here $c/a = 1.60$) with moderate distribution in $\bar{q}_l$, confirming that their relaxed lattices are distorted HCP structure. On the other hand, alloys with high Nb-concentration ($x \geq 9$) represented with SQS of BCC or HCP lattices converge upon relaxation to the same domain in $(\bar{q}_8, \bar{q}_{12})$ plane (see also Appendix Figure A4.4), and exhibit distorted BCC structures as revealed earlier here in the Voronoi analysis in Figure 4.1(b).

Thus, we have explicitly shown with local structural analysis that $Nb_x(HfZrTi)_y$ alloys undergo a structural change from distorted HCP lattices (for $x = 0$, and 3) to distorted BCC lattices (for $x \geq 6$) at 16% Nb-concentration (since $100 \times 6/36 \simeq 16$). Our work reveals an Nb-driven phase transformation in SQS-modeled configurations, consistent with the experimental observations [178, 182]. It is interesting that HCP lattice spontaneously transforms to BCC lattice through structural relaxation without having to cross any energy barrier. Secondly, this transformation has a signature in the electronic structures (see Appendix Figure A4.5). At high Nb-concentration ($x \geq 9$), d-orbitals of Nb dominate the electronic states near the Fermi energy, explaining how Nb is a BCC-stabilizer.

In this work, we showed that Nb plays the role of β-stabilizer of $Nb_x(HfZrTi)_y$. It is interesting to note that if Nb is replaced by another BCC element like Ta, the structural effect remains qualitatively similar. Experiments of Huang et al [183] show that the decreasing content of Ta leads the destabilization of BCC phase of $Ta_xHfZrTi$ and promotes the formation of HCP phase. The onset of HCP phase is detected at 16.7% atomic concentration of Ta (at the same concentration we report BCC→HCP transformation in $Nb_xHfZrTi$) and the fractional share of HCP phase enhances with further reduction in Ta content (see XRD patterns and EBSD images in Figure 1 of ref. [183]). In an another report by Wang et al. [184], $Ta_{0.5}HfZrTi$ exhibits a martensitic transformation from BCC→HCP beyond 6% tensile strain (see Figure 6 of ref. [184]).

(a) (with ILDs) — Ideal lattice (inset)

$E_{BCC} - E_{HCP}$ (meV/atom)

- SQS (●—●)
- Random (○—○)

(c)

HCP □ ... BCC ◉

- ○ BCC (x = 0)   ● HCP (x = 0)
- ◇ BCC (x = 3)   ◆ HCP (x = 3)
- △ BCC (x = 6)   ▲ HCP (x = 6)

$Nb_aMo_bW_cTa_d$ and Mo_pW_q (total 10)

BCC and HCP of $x \geq 9$

$\bar{q}_{12}$ vs $\bar{q}_8$

(d) BCC — A

(e) A, B, HCP

(b) x	BCC SQS (n_3, n_4, n_5, n_6)	HCP SQS (n_3, n_4, n_5, n_6)	Voro+$\bar{q}_l$ low energy phase
0	(3, 212, 9, 279)	(3, 234, 161, 63) close to HCP on $\bar{q}_l$-plane	HCP
3	(2, 214, 4, 284)	(2, 176, 144, 162) close to HCP on $\bar{q}_l$-plane	HCP
6	(2, 214, 4, 284)	(0, 216, 0, 288)	BCC
9	(0, 216, 0, 288)	(2, 214, 4, 284)	BCC
12	(0, 216, 0, 288)	(0, 216, 0, 288)	BCC
15	(0, 216, 0, 288)	(0, 216, 0, 288)	BCC

Figure 4.1: Structural transition in $Nb_x(HfZrTi)_y$ with $x + 3y = 36$ and analysis with Voronoi tessellation (b) and bond-orientational order parameters (c). In (a), relative energies of relaxed special quasirandom and randomized HCP and BCC structures of $Nb_x(HfZrTi)_y$ reveal stabilization of the BCC phase beyond 25% Nb concentration (i.e; $x \geq 9$), corresponding to equiatomic composition. Unrelaxed SQS with ideal lattice (inset) also reveals the same. In (b), n_k is the the number of k-sided Voronoi faces. Voronoi cell of an ideal BCC lattice point has squares and hexagons (d), while that of an HCP lattice point has only quadrilaterals (e). Voronoi vertex of order 3 (type-**A**) is stable and robust against internal lattice distortions (ILDs), while of the higher order (type-**B**) is unstable as new polygons appear there under distortion (see Appendix Figure A4.1). From the Voronoi faces analysis (b) of energetically favorable SQS configurations as seen in (a), we find that a distorted BCC structure of $Nb_x(HfZrTi)_y$ is stabilized for $x \geq 6$, corresponding to 16% Nb-concentration rather than equiatomic concentration (c). The plane of bond orientational parameters $(\bar{q}_8, \bar{q}_{12})$ facilitates identification of the lattice structure having low ILDs. It is clear that structures of $Nb_aMo_bW_cTa_d$ and Mo_pW_q optimize to perfect BCC lattice with not much ILDs while $Nb_x(HfZrTi)_y$ exhibit severe ILDs as evident in a wide spread in their $\bar{q}_l$ values. The HCP SQS of low Nb-concentration ($x = 0$ and 3) alloys optimize to points rather close to that of perfect HCP lattice on $(\bar{q}_8, \bar{q}_{12})$ plane. Thus we identify HCP→BCC transition in $Nb_x(HfZrTi)_y$ at 16% Nb-concentration.

4.3.2 ILDs peak at the HCP to BCC transition

Wide distribution of $\bar{q}_l$ (Figure 4.1(c)) reflects on the presence of significant ILDs in HEAs $Nb_x(HfZrTi)_y$. For a quantitative measure of ILDs, we use [185]

$$\text{ILD} = \frac{1}{N} \sum_{i=1}^{N} \sqrt{(x_i - x_i')^2 + (y_i - y_i')^2 + (z_i - z_i')^2} \qquad (4.3)$$

where (x_i, y_i, z_i) and (x_i', y_i', z_i') are reduced coordinates of unrelaxed sites (ideal/reference lattice points) and relaxed atomic positions of the ith atom, respectively and N is the total number of atoms. We note that ILDs in binary Mo_pW_q, quaternary $Nb_aMo_bW_cTa_d$, and $Nb_x(HfZrTi)_y$ alloys are of order of $10^{-4}, 10^{-3},$ and 10^{-2}, respectively (see Figure 4.2(a) and Appendix Table A4.4). In contrast to BCC $(MoW)_{18}$ (Figure 4.2(c)), a sideview of the relaxed SQS lattice of BCC $(NbHfZrTi)_9$ (Figure 4.2(d)) shows significant atomic perturbations from their ideal lattice sites. On increasing x in $Nb_x(HfZrTi)_y$, ILDs of their energetically favorable SQS first increase, reach a maximum at $x = 6$ where HCP→BCC transformation is marked, and then decrease subsequently (see Figure 4.2(b)).

To understand the severe lattice distortions for the configuration at structural transformation (Figure 4.2(b)), we highlight the role of phonons. For the dynamical stability of a crystalline material, the frequencies of all the phonons must be real. We confirm the dynamical stability of the fully relaxed BCC NbHfZrTi and NbMoWTa at Γ-point of Brillouin zone of 3×3×2 sized supercell, as all phonons calculated using density functional perturbation theory are real (see Appendix Figure A4.6). G. D. Samolyuk *et al.* [179] showed that the ideal BCC configuration of NbHfZrTi is unstable, but static displacements introduced upon full relaxation stabilize the lattice; i.e., ILDs stabilize this alloy. Therefore, a maximum in ILDs at the HCP→BCC transition (Figure 4.2(b)) correlates with softening of phonons because large atomic displacements are associated with soft phonons. On either side of the transition (Figure 4.2(b)), continuous decline in ILDs weakens the softening of modes, in principle.

ILDs in HEAs originate from various factors such as atomic size mismatch, dissimilar crystal structures, and difference in valence electrons of their constituent elements. Multi-elemental
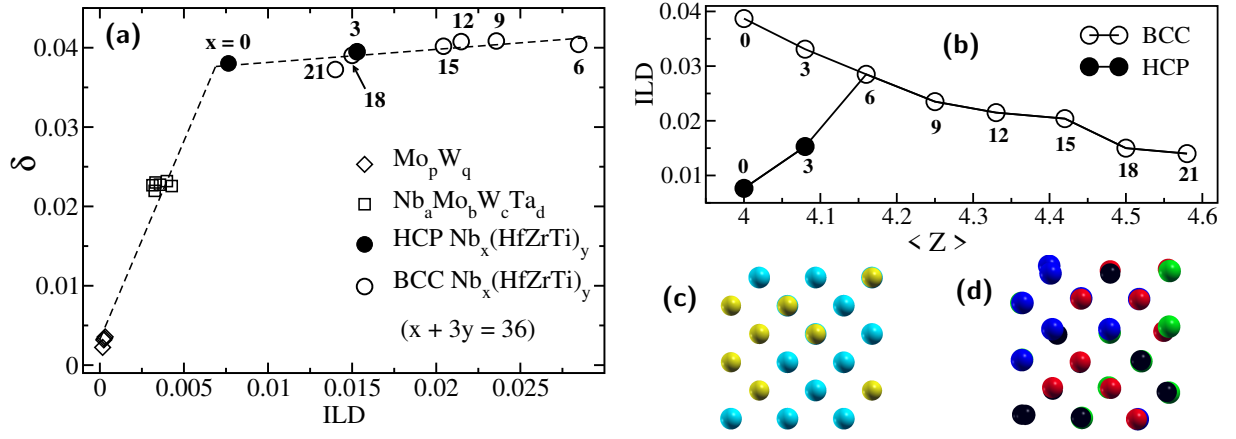
Figure 4.2: Factors of ILDs: (a) In binary Mo_pW_q (four different compositions), quaternary $Nb_aMo_bW_cTa_d$ (six different compositions), and $Nb_x(HfZrTi)_y$ (x is written near the symbols) alloys, internal lattice distortions (ILDs) are of the order of $10^{-4}, 10^{-3},$ and 10^{-2} respectively. The z-axis view of relaxed SQS of MoW (c) and NbHfZrTi (d) show significant presence of ILDs in the latter. Although atomic size mismatch (δ) is a primary factor of ILDs, the significant variation in ILDs across different compositions of $Nb_x(HfZrTi)_y$ without any remarkable change in their δ values asks for another possible factor. In contrast to HEAs $Nb_aMo_bW_cTa_d$, the structural differences among the constituent elements of $Nb_x(HfZrTi)_y$ and associated HCP→BCC transition at x = 6 where ILDs also peak (b) explains for the variation in their ILDs. For BCC lattice SQS, ILDs decrease with increase in average valency ($<Z>$) and that occurs when Nb-concentration (x) increases.

mixing always suffer from atomic size mismatch (δ) which is quantified as [155]

$$\delta^2 = \sum_{i=1}^{n} c_i(1 - r_i/\bar{r})^2 \ \text{ with } \ \bar{r} = \sum_{i=1}^{n} c_i r_i, \tag{4.4}$$

where n is the number of types of elements being mixed, c_i and r_i are the atomic concentration and radius of ith element, and $\bar{r}$ is the average radius. δ is considered the primary factor relevant to ILDs [185, 186]. Figure 4.2(a) depicts this for BCC Mo_pW_q, $Nb_aMo_bW_cTa_d$, and HCP $(HfZrTi)_{12}$ alloys as their ILDs linearly increase with δ. However, taking $Nb_x(HfZrTi)_y$ alloys as an example, we demonstrate that rather than δ, the elemental structural differences among their constituents and their average valence electrons (Figure 4.2(b)) strongly influence ILDs. An increase in the number of average valence electrons $<Z>$ within BCC $Nb_x(HfZrTi)_y$ — achieved by the gradual rise of Nb-concentration — lowers ILDs. This mechanism of control over ILDs by tuning $<Z>$ is consistent with a recent work reported only for BCC HEAs [179]. Therefore, ILDs of $Nb_x(HfZrTi)_y$ alloys peak at the HCP→BCC transition (see Figure 4.2(b)), and thus, ILDs in these alloys exhibit a dual effect of valency and crystal structures of constituent

elements. The role of crystal structures of constituents on ILDs is further highlighted by another set of quaternary HEAs, $Nb_aMo_bW_cTa_d$ (composed of only BCC structural elements), which does not show noticeable variation in ILDs with compositions.

The impact of valency on ILDs is simple to understand because change in valence state affects electronegativity (χ) of an element [187]. Transition metals often exhibit multiple valencies, and a higher valency state of a given element will have a larger electronegativity than its lower valency state [187]. The valency state of Nb is 5 while that of {Hf, Zr, Ti} is 4, hence the continuous rise of Nb-concentration increases the average valency of atoms in $Nb_x(HfZrTi)_y$. As expected, ILDs decrease with rise in $<Z>$ or χ as it strengthens the intermetallic formation tendency. Monte Carlo simulations reveal chemical short-range order (SRO) in NbHfZrTi [188], where Nb-Hf and Zr-Ti prefer to form nearest-neighbor pairs. While some degree of chemical SRO features in most of the HEAs [189], the present alloy configurations lack any kind of ordering since the generation of SQS aims for true disordered state [166]. A large $\Delta\chi$ between pair of constituent atoms causes charge transfer too, which in turn, alters their atomic sizes slightly [190, 191]. The atoms donating electrons shrink in size while the acceptors enlarge in their sizes. Thus, the charge transfer has marginal effect on the atomic size mismatch and ILDs [190, 191].

4.3.3 ILDs and configurational entropy

For a qualitative measure of ILDs, we generated and relaxed 50 distinct SQS configurations for each equiatomic BCC NbHfZrTi, NbMoWTa, and MoW alloys and analyzed them with histograms of their $\bar{q}_8$ values and Voronoi volumes (see Figure 4.3(a)). For NbHfZrTi, the distribution exhibits a very broad peak, while it is quite narrow for NbMoWTa, and MoW has a single sharp peak. The width of these peaks in distributions, similar to Bragg peak width in XRD, serves as a measure of ILDs. Thus, ILDs are negligible in MoW and notably significant in NbHfZrTi. Here, $\bar{q}_8$ of MoW corresponds to that of an ideal BCC structure ($\bar{q}_8 = q_8 = 0.429$).

To analyze the effects of ILDs on configurational energy of HEAs, we consider these equiatomic SQS configurations, each with a different chemical arrangement. We find that SQS configurations of HEAs span a range of energy while the configurations of a solid-solution (MoW) have almost the same energy (Figure 4.3(b) inset). Lower energy SQS configurations

of HEAs are more favorable, and hence this energy fluctuation signifies a departure from the *ideal* mixing condition that requires each configuration to have the same energy [156]. Clearly, HEAs with higher ILDs display large fluctuations in their configurational energies.

From the distribution of energy of these SQS configurations, we estimate configurational entropy. If energy of ith configuration be E_i among chosen Ω_{config} configurations, then at temperature T its probability will be

$$p_i = \frac{\exp(-\beta E_i)}{\sum_1^{\Omega_{\text{config}}} \exp(-\beta E_i)} \tag{4.5}$$

where $\beta = 1/(k_{\text{B}}T)$. Configurational entropy is deduced as

$$S_{\text{config}} = -k_{\text{B}} \sum_{i=1}^{\Omega_{\text{config}}} p_i \ln p_i. \tag{4.6}$$

We note that S_{config} of NbMoWTa and NbHfZrTi rises with temperature (see Figure 4.3(b)) and saturates to the Boltzmann entropy $k_{\text{B}} \ln \Omega_{\text{config}}$ (here, $k_{\text{B}} \ln 50 = 3.912 k_{\text{B}}$ which corresponds to MoW). In the ideal mixing of n types of elements,

$$S_{\text{config}} = S_{\text{ideal}}^{\text{mix}} = -N_{\text{atom}} k_{\text{B}} \sum_{i=1}^{n} c_i \ln c_i, \tag{4.7}$$

where c_i is the atomic concentration of ith element, and it becomes $S_{\text{config}} = N_{\text{atom}} k_{\text{B}} \ln n$ for the equiatomic case. The computed configurational entropy for a finite number of SQS configurations will be lower than their ideal mixing entropy (for equiatomic quaternary systems, $N_{\text{atom}} k_{\text{B}} \ln n = 36 k_{\text{B}} \ln 4 = 49.90 k_{\text{B}} >> k_{\text{B}} \ln 50$), but it captures the thermal effect that the configurational entropy approaches the Boltzmann entropy as the temperature rises. It is noteworthy that before saturation, the increase in S_{config} with temperature is slower in HEAs exhibiting stronger ILDs (see Figure 4.3(b)). Thus, we demonstrate that it is reasonable to approximate the configurational entropy of HEAs as the entropy of ideal mixing since each configuration becomes equiprobable even at a fairly low T (such as 300 K).

Some degree of chemical short-range order (CSRO) exists in most of the high-entropy alloys [189]. In the presence of CSRO, the configurational entropy must be lower than $S_{\text{ideal}}^{\text{mix}}$ (since configurations with CSRO will have much lower energies than SQS ones). CSRO means
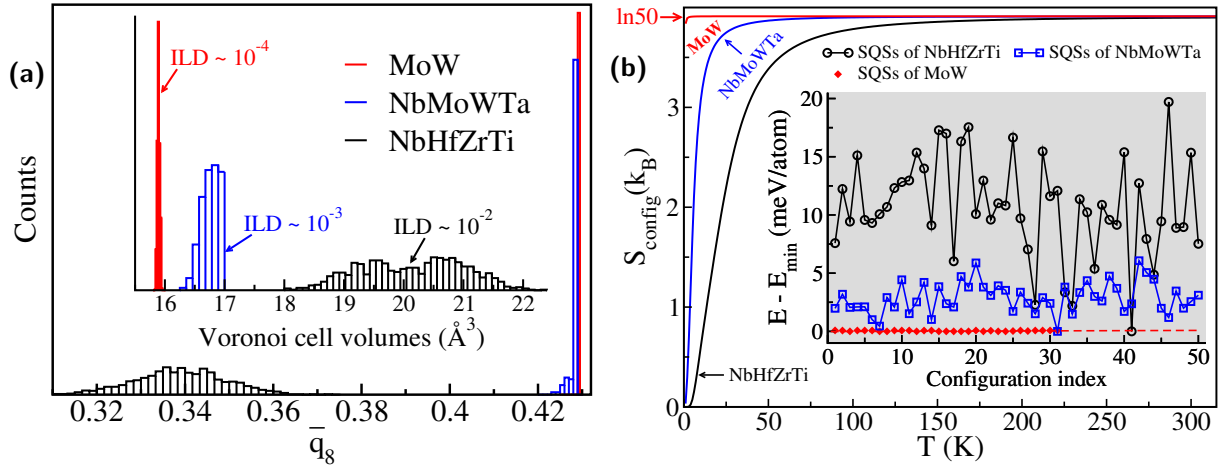
Figure 4.3: Internal Lattice Distortions, energetics and configurational entropy. Histograms (a) of bond orientational parameter $\bar{q}_8$ and Voronoi cell volumes (inset) obtained from the relaxed structures of 50 SQS configurations of each of the equiatomic BCC alloys. A sharp peak in $\bar{q}_8$ of MoW marks the ideal BCC structure, a slight deviation for NbMoWTa reveals relatively weak ILDs. In contrast, notably broad and shifted peak in $\bar{q}_8$ of NbHfZrTi reveals its severe ILDs, and distributions of Voronoi volumes confirms this trend in ILDs and the local structure. (b) Configurational entropy approaches the entropy of ideal mixing, (Boltzmann entropy $k_B \ln 50$) at fairly low temperatures, though slower in NbHfZrTi due to larger fluctuations in the energy of their distinct SQS configurations (shown in inset) than of NbMoWTa and MoW.

preferential configurations of HEA. This reduces the number of possible configurations and hence lowers configurational entropy i.e. $S_{\text{config}} < S_{\text{ideal}}^{\text{mix}}$. At high temperature, S_{config} approaches $S_{\text{ideal}}^{\text{mix}}$ (see Figure 4.3(b)) as expected, and approximating configurational entropy by $S_{\text{ideal}}^{\text{mix}}$ is justified. Simulations with SQS configurations of an HEA prevent the formation of CSRO on its lattice, and hence, the estimated configurational entropy should be $S_{\text{ideal}}^{\text{mix}}$. In Chapter 5 (subsection 5.3.5), we reveal CSRO in NbMoWTa HEA using DFT-based Swap Monte Carlo simulation. There, we find that atomic pairs Ta-Ta and Mo-Mo avoid bonding, while Mo-Ta, Nb-W, Nb-Mo, and W-Ta prefer bonding. Appearance of such preferential bondings termed CSRO decrease the configuration entropy of an HEA.

4.3.4 Estimation of vibrational entropy

A chemical disorder associated with site occupation requires large system sizes in high-entropy alloys making phonon calculations challenging. Chemical disorder underpinned by random distributions of atoms introduces glassy behavior like local fluctuations in masses, force constants, and atomic displacements. In disordered systems, Brillouin zone folding causes extra modes of vibration, which constitute a peak (called "Boson peak") in the phonon density

of states $g(\omega)/\omega^2$ profile at low frequency. Boson peak is the universal feature of disordered systems, and it arises in HEAs, owing to chemical disorder and ILDs [192]. In HEAs, ILDs disrupt the symmetry of the local structure, but the long-range lattice is consistent with either BCC, HCP, or FCC structures. The presence of chemical disorder and ILDs make HEAs intermediate between crystalline and amorphous materials [193]. In Debye theory, $g(\omega)/\omega^2$ is constant, but having a Boson peak thus raises a concern in the use of the Debye model for disordered systems [194, 195].

We still resorted to the Debye model because of the challenges posed by chemical disorder modeled with special quasirandom structures (supercells) and computational cost of phonon calculations scaling as the fourth power of the number of atoms in the supercell. The appearance of the Boson peak is a low-temperature phenomenon, and our analysis with the Debye model to determine thermal properties at high temperatures is reasonable because the overall number of modes is correctly accounted for. To estimate vibrational entropy under Debye model [173, 196], we used

$$S_{\mathrm{vib}}(V,T) = Nk_{\mathrm{B}} \left[4D\left(\frac{\theta_{\mathrm{D}}}{T}\right) - 3\ln\left(1 - \exp\left(\frac{\theta_{\mathrm{D}}}{T}\right)\right) \right] \tag{4.8}$$

and

$$\theta_{\mathrm{D}} = \frac{h}{k_{\mathrm{B}}} \left(\frac{3N}{4\pi V}\right)^{1/3} v_m, \tag{4.9}$$

where the supercell of volume V contains N atoms. $D(x)$ is the third-order Debye function and θ_{D} is the Debye temperature. To determine θ_{D} of material, we extracted average sound velocity (v_m) from the DFT-calculated elastic constants tensor. Thus, we estimate the vibrational entropy of each alloy configuration of $\mathrm{Nb}_x(\mathrm{HfZrTi})_y$ (see Appendix Table A4.5) at $T = 300$ K by inserting θ_{D} in eq 4.8.

4.3.5 Entropic stabilization

Entropic stabilization is long-standing concept used in a wide class of materials [197, 198, 199]. Binary alloys with a positive but small enthalpy of mixing, which causes a miscibility gap in the phase diagram, also get stabilized if sufficient thermal entropy is acquired [200]. The configurational entropy per atom in equiatomic binary, ternary, and quaternary alloys are 0.69 k_{B}, 1.09 k_{B} and 1.38 k_{B}, respectively. But in multicomponent systems such as HEAs, the postulate that high configurational entropy alone stabilizes the

single-phase solid-solution [25] has been a topic of controversy [157, 196]. Other kinds such as vibrational, electronic, and magnetic entropies can also be important to the stability of HEAs, while major contributions come from vibrational and configurational ones [196]. In HEAs $Nb_x(HfZrTi)_y$, we find that vibrational entropy contributes more than the configurational one (see Appendix Table A4.5) to the total entropy. We take the total entropy comprised of vibrational entropy estimated within Debye approximation and configurational entropy approximated as the entropy of ideal solid-solution mixing. In Figure 4.4(top), we show that the total entropy of non equiatomic $Nb_6(HfZrTi)_{10}$ is greater than that of equiatomic $(NbHfZrTi)_9$ peaking at $x = 6$. It is interesting to note that $x = 6$ marks the structural transformation from HCP to BCC too, where ILDs and total entropy reach their maxima.
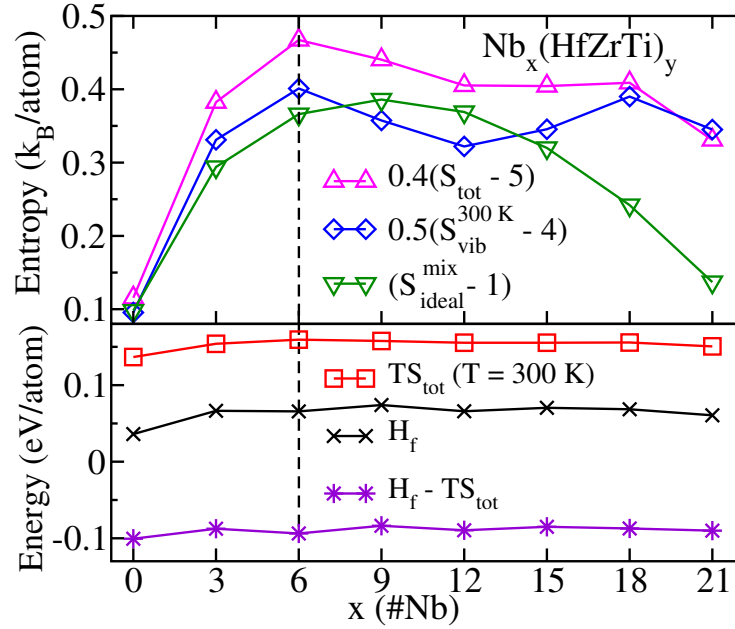
Figure 4.4: Entropic stabilization of favorable phase $Nb_x(HfZrTi)_y$ where $x+3y=36$. The total entropy comprised of Debye vibrational entropy and ideal mixing entropy reaches a maximum for BCC $Nb_6(HfZrTi)_{10}$ in contrast to configurational entropy (S_{ideal}^{mix}) that peaks at equiatomic $(NbHfZrTi)_9$ (top). Here, entropies have been scaled and shifted to facilitate comparison (see Appendix Table A4.5 for actual values). Entropic stabilization of $Nb_x(HfZrTi)_y$ HEAs (bottom) is clear from the fact that their formation energies (H_f) are positive and entropic term, particularly with dominance of vibrational contribution (top), is needed to have favorable free energy of formation (bottom).

We estimate Gibbs free energy to assess the competition between formation energy (i.e., the heat of mixing) and entropy. For the formation energy (H_f) of alloys $Nb_x(HfZrTi)_y$, we subtract its concentration-weighted elemental energies in their most stable bulk crystalline phase from the energy of the alloy. The formation energy of $Nb_x(HfZrTi)_y$ is positive (sign of

instability) while for $Nb_aMo_bW_cTa_d$ it is negative (see Appendix Table A4.4 and A4.5). It means that the former is unfavorable, and the latter is favorable energetically. However, inclusion of entropy makes Gibbs free energy of formation $(H_f - TS_{tot})$ negative and stabilizes $Nb_x(HfZrTi)_y$ (see Figure 4.4(bottom)). For instance, H_f of $(NbHfZrTi)_9$ is 0.074 eV/atom and at $T = 300$ K, alone $TS_{config} = k_BT \ln 4 = 0.036$ eV/atom is insufficient to stabilize and needed a major contribution from vibration as TS_{tot} is 0.158 eV/atom to achieve the overall stability (see Appendix Table A4.5). Hence, with precise quantification, we reinforce the fundamental assumption that entropy stabilizes HEAs. The impact of temperature rise on the structural transformation in $Nb_x(HfZrTi)_y$ has been given at the end of Appendix (see Figure A4.7).

4.4 Conclusions

In conclusion, we have shown that $Nb_x(HfZrTi)_y$ undergoes a structural transformation from HCP to BCC at 16% Nb-concentration. Voronoi analysis and bond-orientational order parameters are tools to help identify the average lattice structure of HEAs exhibiting large ILDs and mark this transformation. The structural differences across constituent elements and their low numbers of valence electrons are dominant factors that cause ILDs in addition to atomic size mismatch in BCC HEAs. At an HCP→BCC transition, ILDs peak and maximize the total entropy. We showed that entropy stabilizes $Nb_x(HfZrTi)_y$, but with a larger share of the vibrational entropy than of the configurational entropy. Taking BCC NbHfZrTi as an example, we highlighted that ILDs ensure the local or dynamical stability of the lattice (Appendix Figure A4.6). However, the overall thermodynamic stability (in terms of free energy) is accomplished by the vibrational entropy.

4.5 Appendix

Special Quasirandom Structures (SQS)

Using *mcsqs* code implemented in Alloy Theoretic Automated Toolkit (ATAT) [165, 166], we generated special quasirandom structures (SQS) of various compositions of alloys Mo_pW_q, $Nb_aMo_bW_cTa_d$, and $Nb_x(HfZrTi)_y$. We kept supercell size and shape fixed at $3 \times 3 \times 2$ of conventional BCC and HCP unit cells. The steps we used to generate SQS strctures are

1. To generate clusters within a given range, we use the following command

   corrdump -l=rndstr.in -ro -noe -nop -clus -2=6.0 -3=5.0 -4=5.0.

   It means that pair, triplet, and quadruplet clusters were made upto 6 Å, 5 Å, and 5 Å respectively. File *rndstr.in* contains the information of unit cell. For instance, for BCC NbHfZrTi it will have

   a a a 90 90 90 $\rightarrow$ Cell parameters

   -0.5 0.5 0.5

   0.5 -0.5 0.5 $\rightarrow$ These three lines are BCC primitive lattice vectors

   0.5 0.5 -0.5

   0.0 0.0 0.0 Nb=0.25, Hf=0.25, Zr=0.25, Ti=0.25 $\rightarrow$ Atoms with their concentrations.

2. Then we ran the command

   mcsqs -n 36.

   It generates 36-atomic SQS structures of automatically chosen supercell shape. We interrupt this command and specify the fixed supercell shape in file *sqscell.out* as below

   1

   3 0 0

   0 3 0

   0 0 2

3. Finally, we run the command

   mcsqs -rc

   and let it running for long time (we ran for 72 hours) to get SQS structures having sufficiently weak site-site correlation.

HCP versus ω phase stability of HfZrTi: We generated three SQS of $(HfZrTi)_{12}$ considering HCP (spacegroup $P6_3/mmc$) and ω (spacegroup $P6/mmm$) lattices. The size of supercell of HCP and ω phases were taken $3 \times 3 \times 2$ and $2 \times 2 \times 3$ respectively of their conventional unit cells. After structural relaxation of these SQS, we find that HCP initialized lattices were more stable than the ω ones (see Table A4.1) by $\Delta E > 16$ meV/atom.

The conventional unit cell of the ω structure has three lattice points, and q_l values of the two lattice points are degenerate (see Figure A4.2). Below I have given the details of conventional unit cells of HCP and ω phases of Ti:

HCP Ti: cell parameters (Å)

$$
\begin{bmatrix}
2.934 & 0 & 0 \\
-1.467 & 2.541 & 0 \\
0 & 0 & 4.657
\end{bmatrix}
$$

Atomic positions (reduced coords.)

Ti   2/3   1/3   3/4

Ti   1/3   2/3   1/4

ω **Ti:**   cell parameters (Å)

$$
\begin{bmatrix}
4.577 & 0 & 0 \\
-2.288 & 3.964 & 0 \\
0 & 0 & 2.829
\end{bmatrix}
$$

Atomic positions (reduced coords.)

Ti_1 0   0   0

Ti_2 1/3   2/3   1/2

Ti_2 2/3   1/3   1/2

Voronoi Analysis

The geometry of the Voronoi cell provides structural insights into particle arrangement on a plane or in space. For particles in space, the Voronoi cell is constructed around each particle

Table A4.1: Energy of HCP and ω lattice SQS configurations of $(HfZrTi)_{12}$. We note that SQS with HCP lattice is more stable than SQS with ω lattice.

	E_{HCP}^{DFT} (eV/atom)	E_{ω}^{DFT} (eV/atom)	$E_{\omega}^{DFT} - E_{HCP}^{DFT}$ (meV/atom)
SQS-1	-5383.865	-5383.849	16
SQS-2	-5383.866	-5383.847	19
SQS-3	-5383.866	-5383.846	20

such that its all faces are closer to the particle within it than any other particle. The Voronoi cell of BCC lattice point is *truncated octahedron* having 24 vertices, 36 edges, and 6 square and 8 hexagonal faces. The Voronoi cell of a HCP lattice point is *trapezo-rhombic dodecahedron* having 14 vertices, 24 edges, and 6 trapezoidal and 6 rhombic faces (see Figure A4.1(**a**)).

Stability of Voronoi vertex: The order of a vertex in a graph is the number of edges incident into that vertex. Each Voronoi vertex of the BCC lattice is of order 3, which is topologically stable, while some Voronoi vertices of the HCP lattice are of order 4, which are topologically unstable [103] (see Figure A4.1(**a**)). To test this, we created $3 \times 3 \times 2$ size supercells of conventional unit cells of BCC (Nb) and HCP (Hf) lattices. Then, we added random perturbation/noise to each lattice point $(\vec{r}_0)$ using $\vec{r} = \vec{r}_0 + \Delta\vec{R}$, where $\vec{R}$ is a vector which components are of random value in (-1,1). We kept lattice vectors of supercell fixed and did not perform any kind of structural optimization. After executing Voronoi construction of these distorted lattices (see Figure A4.1(**b**)), we note that Voronoi cells of BCC supercell do not yield any new polygonal face. In contrast, cells corresponding to HCP supercell have triangular, pentagonal, and hexagonal faces. The appearance of new polygonal faces in addition to quadrilaterals is attributed to order 4 *unstable* vertices.

Bond-orientational Order Parameters

c/a ratio dependence of q_l for HCP elements: q_l also varies with c/a ratio of HCP lattice. In ideal HCP lattice this ratio equals to $\sqrt{8/3} \simeq 1.633$ but c/a of HCP structural elements varies from 1.58-1.65. Mg is nearest to the ideal HCP with c/a = 1.62. In Table A4.3, we show the variation in q_8 and q_{12} with c/a ratio.
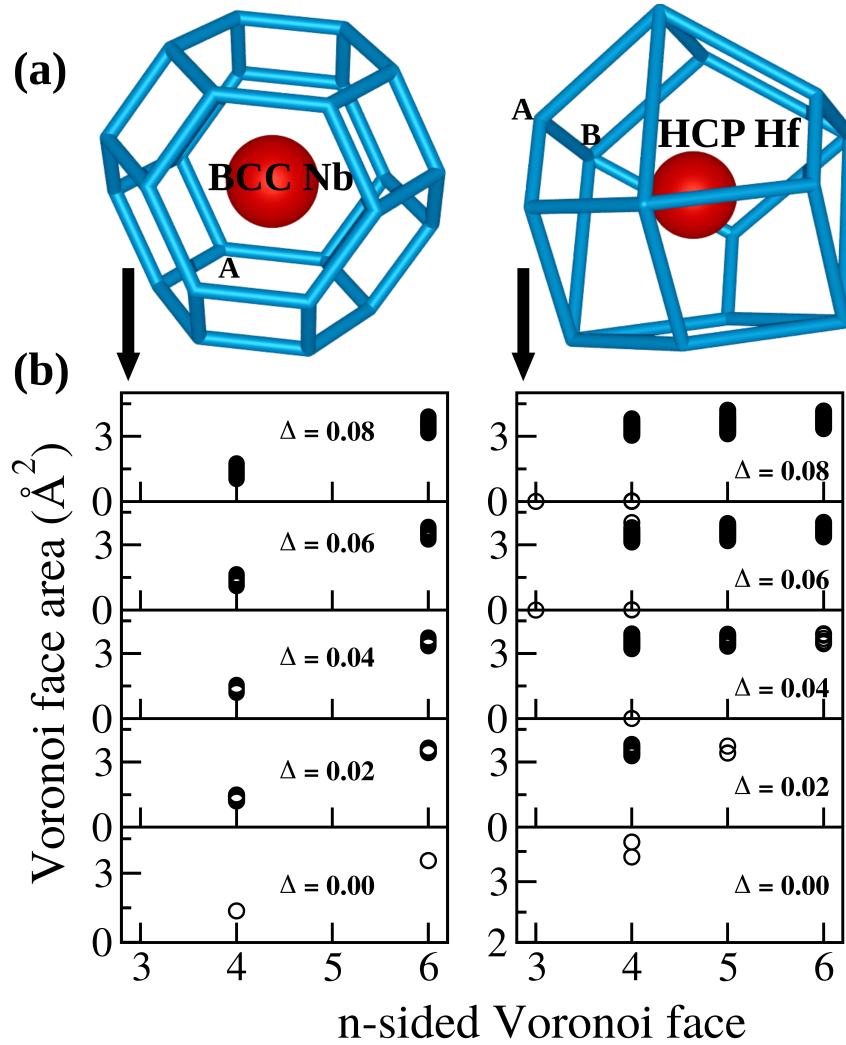
Figure A4.1: **(a)** The Voronoi cell of perfect BCC lattice point has six squares and eight hexagonal faces, and the Voronoi cell of HCP lattice point has six trapeziums and six rhombuses. **(b)** Voronoi faces of slightly perturbed HCP lattice (here Δ is the strength of random perturbation) can have 4, 5, or 6 sides since some of its Voronoi vertices are of order 4 (marked B, which are topologically unstable). However, Voronoi faces of BCC lattice do not yield new faces under slight perturbation since its all Voronoi vertices are of order 3 (marked A, which are topologically stable).

Table A4.2: Values of q_l of ideal crystals: **n** is the number of nearest neighbors. In BCC structure, 8 nearest neighbors are at distance $\frac{\sqrt{3}a}{2} = 0.866a$ and 6 next nearest neighbors are at distance a, where a is its lattice parameter. In distorted BCC, a clear distinction between nearest and next nearest neighbors is difficult and hence we search bonds upto next nearest neighbors (**n = 14**) for q_l estimation. To differentiate between BCC and HCP lattices of HEAs, we choose $(\bar{q}_8, \bar{q}_{12})$ plane.

q_l	BCC	BCC	HCP (c/a = 1.633)	FCC
	Im$\bar{3}$m	Im$\bar{3}$m	P6$_3$/mmc	Fm$\bar{3}$m
	n = 8	**n = 14**	**n = 12**	**n = 12**
q_2	0	0	0	0
q_3	0	0	0.076	0
q_4	0.509	0.036	0.097	0.190
q_5	0	0	0.252	0
q_6	0.629	0.511	0.484	0.575
q_7	0	0	0.311	0
q_8	0.213	**0.429**	**0.317**	**0.404**
q_9	0	0	0.138	0
q_{10}	0.650	0.195	0.010	0.013
q_{11}	0	0	0.123	0
q_{12}	0.415	**0.405**	**0.565**	**0.600**

Table A4.3: Variation of q_8 and q_{12} with c/a ratio of HCP lattice.

c/a	1.633	1.62	1.61	1.60	1.59	1.58
q_8	0.317	0.320	0.323	0.326	0.329	0.332
q_{12}	0.565	0.563	0.562	0.561	0.560	0.558
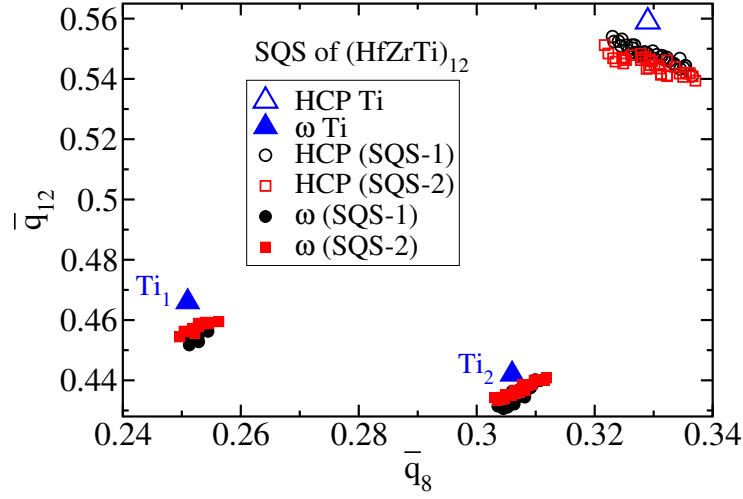
Figure A4.2: On $(\bar{q}_8, \bar{q}_{12})$ plane, optimized SQS of ω lattice $(HfZrTi)_{12}$ and of HCP lattice $(HfZrTi)_{12}$ stand apart.

Variation of $\bar{q}_l$ with ILDs: To see the variation of $\bar{q}_l$ with ILDs, we considered elements BCC Nb, HCP Hf, and FCC Al. We took $3 \times 3 \times 2$ size supercell of BCC and HCP conventional unit cells $2 \times 2 \times 2$ size supercell of FCC conventional unit cell. Then, we added random perturbation/noise to each lattice point ($\vec{r_0}$) using $\vec{r} = \vec{r_0} + \Delta\vec{R}$, where $\vec{R}$ is a vector which components are of random value in (-1,1). We kept lattice vectors of supercell fixed and did not perform any kind of structural optimization. In Figure A4.3, we show the trend of $\bar{q}_l$ and q_l with noise in such distorted lattices and find that these values decrease with increase in noise (Δ or ILDs). We note that $(\bar{q}_8, \bar{q}_{12})$ points get grouped into distinct clusters according to the strength of noise while points (q_8, q_{12}) of different noise values get mixed. For the better resolution, we chose $(\bar{q}_8, \bar{q}_{12})$ plane instead of $(\bar{q}_4, \bar{q}_6)$ plane (see Table A4.2).
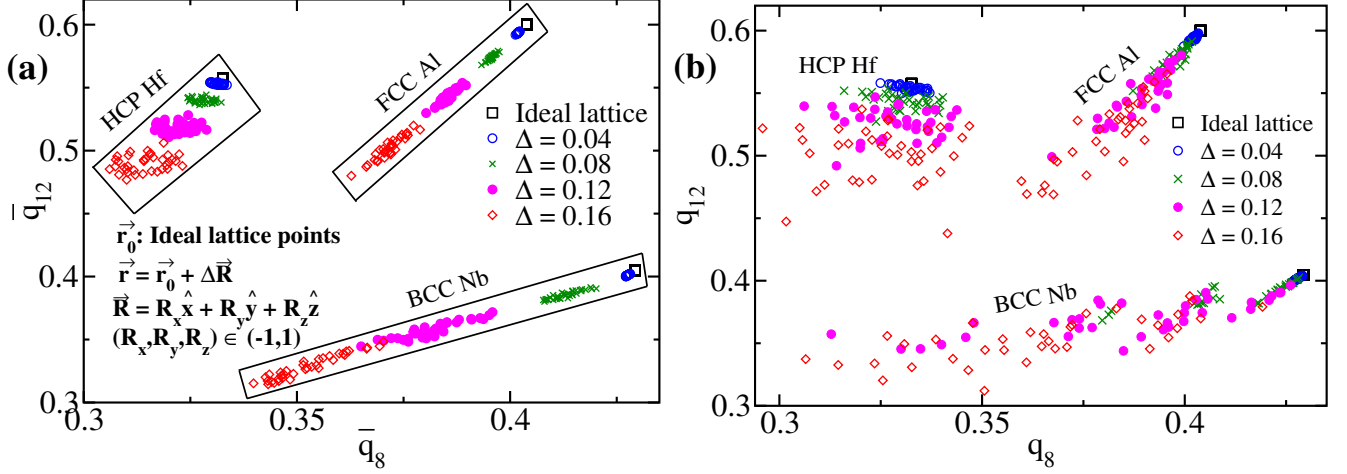
Figure A4.3: Variation of $\bar{q}_l$ with random noise (Δ) in simple crystals. **(a)** We note that $\bar{q}_l$ decreases from its ideal crystalline value with increase in noise. These ($\bar{q}_8$, $\bar{q}_{12}$) points group together in different clusters depending on the strength of noise. **(b)** But points (q_8, q_{12}) do not form such distinct clusters with varying degree of noise. Hence, we prefer $\bar{q}_l$ values rather than q_l in case of distorted crystals.
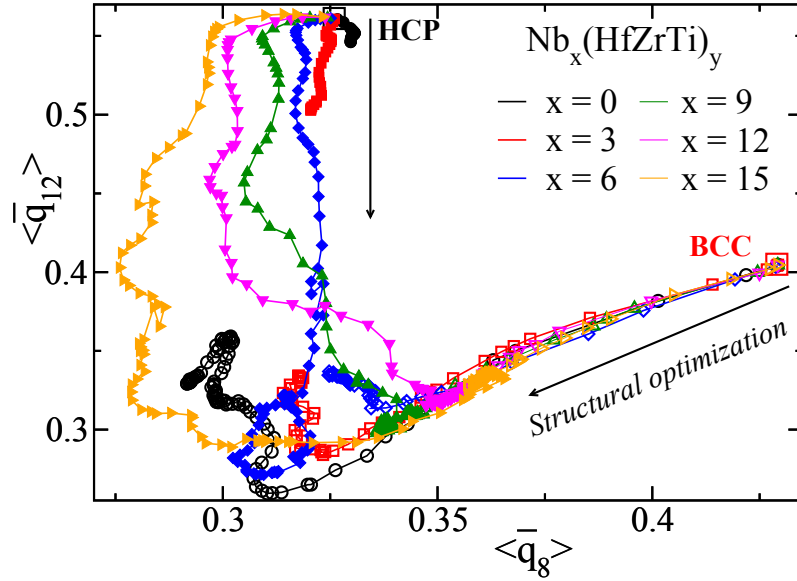
Figure A4.4: Pathway of structural optimization of 36-atomic $Nb_x(HfZrTi)_y$ in terms of $< \bar{q}_l >$ ($= \frac{1}{N} \sum_{i=1}^{N} \bar{q}_{l,i}$ which is averaged $\bar{q}_l$ per atom). Here, $< \bar{q}_l >$ is calculated at each BFGS step of structure optimization. For $x = (0, 3)$ Nb, $< \bar{q}_l >$ values of both BCC and HCP lattice SQS after structural optimization terminate at different ($< \bar{q}_8 >, < \bar{q}_{12} >$) coordinates indicating dissimilar optimized structures whereas for $x = (9, 12, 15)$ Nb, $< \bar{q}_l >$ values of both BCC and HCP lattice SQS terminate at almost same coordinates confirming similar optimized structures which are in fact distorted BCC structures.
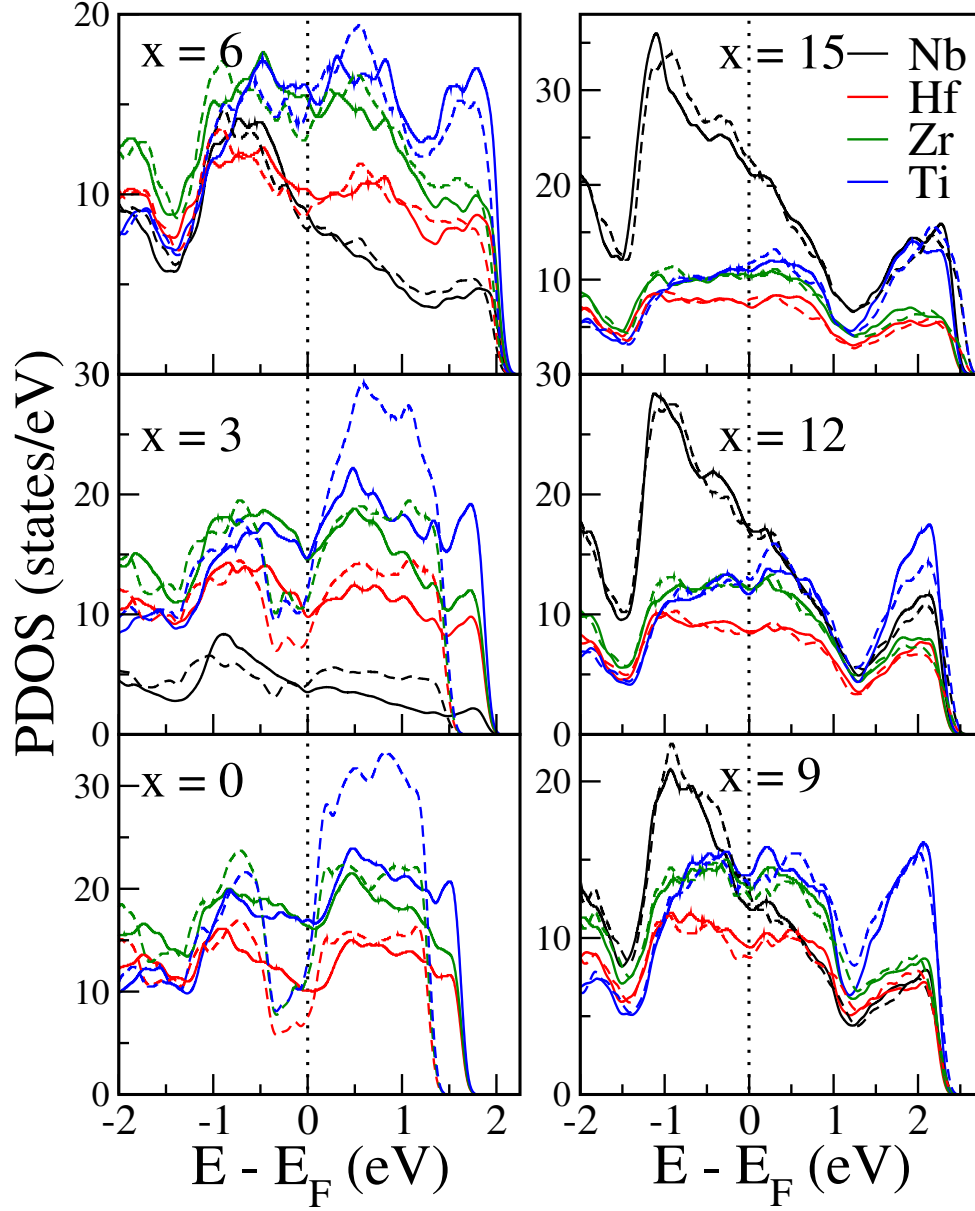
Figure A4.5: Atomwise projected density of electronic states of optimized BCC (solid lines) and HCP (dashed lines) lattice SQS $Nb_x(HfZrTi)_y$ alloys; $x + 3y = 36$: For $x > 6$, the PDOS of the two phases are almost identical hinting the same crystal structure as well. With rise in Nb-concentration, electronic states of Nb dominate near Fermi level which may explain for the stabilization of BCC phase.

Formation Energy

We estimate the formation energy (or, enthalpy of formation) of Mo_pW_q as follows

$$H_f = \frac{E_{Mo_pW_q} - pE_{Mo} - qE_W}{p + q}$$

where E_{Mo} and E_W are the energies of the constituent elements in their most stable phase, and $E_{Mo_pW_q}$ is the DFT optimized energy of the alloy. The same expression has been extended to the quaternary alloys to estimate their formation energies (see Table A4.4).
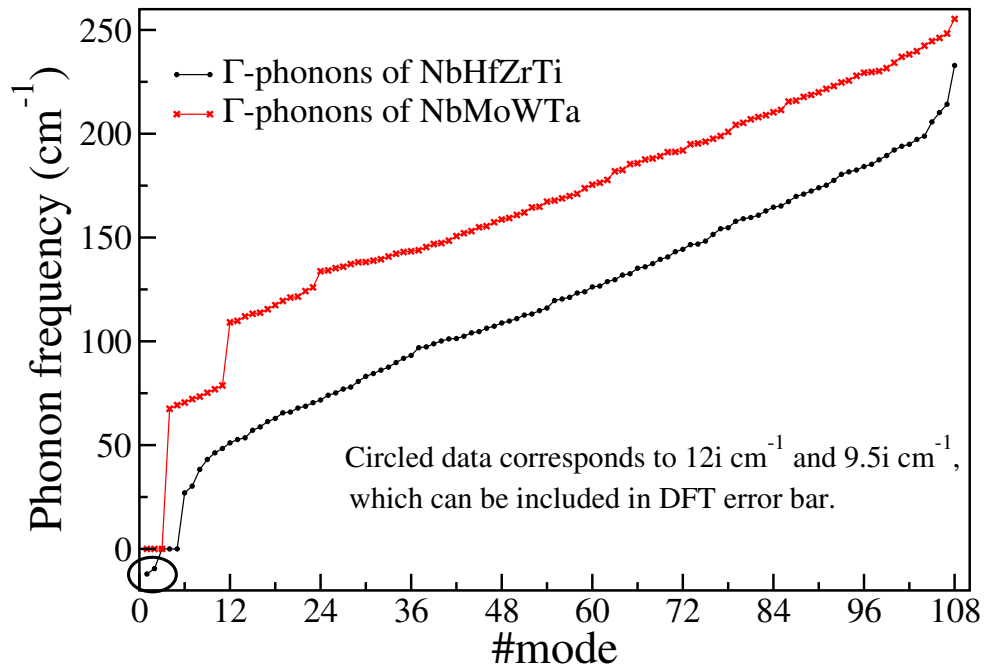
Figure A4.6: Γ-point phonons of fully relaxed (i.e. ILDs≠0) BCC lattice of NbHfZrTi and NbMoWTa of 3×3×2 sized supercell. Frequencies of NbHfZrTi are softer than those of NbMoWTa, and appearance of two imaginary but fairly weak phonon frequencies can be under DFT error bar.

Table A4.4: The formation energies (H_f) of any composition of Mo_pW_q alloys stand at 0 eV/atom, a criterion needed to hold to form the ideal solid solution. Negative H_f makes $Nb_aMo_bW_cTa_d$ alloys favorable to form while positive H_f makes $Nb_x(HfZrTi)_y$ enthalpically unfavorable but entropy stabilize them (see Table A4.5). Across the three sets of alloys, internal lattice distortions (ILDs) increase with rise in their atomic size mismatch (δ) as we go from simple (binary) to complex ones (one quaternary is composed of only BCC elements while another exhibits HCP to BCC transition and contain three HCP elements). In these alloys, the average number of valence electrons per atom $< Z >$ is estimated by taking $Z = 6$ (Mo, W), 5 (Nb, Ta), and 4 (Hf, Zr, Ti) of their constituent elements. We note a decrease in ILDs with rising $< Z >$ in BCC structured alloys.

Alloys	Structure	H_f (eV/atom)	δ (10^{-2})	ILD (10^{-4})	$< Z >$
Mo_4W_{32}	BCC	0	0.223	1.6	6
$Mo_{10}W_{26}$	"	0	0.318	2.3	6
$(MoW_{18}$	"	0	0.356	3.1	6
$Mo_{24}W_{12}$	"	0	0.336	2.7	6
$(NbMoWTa)_9$	BCC	-0.068	2.267	31.3	5.50
$(NbMoW)_{10}Ta_6$	"	-0.078	2.196	32.6	5.55
$(NbWTa)_8Mo_{12}$	"	-0.078	2.302	33	5.55
$Nb_8Mo_{11}W_{12}Ta_5$	"	-0.075	2.274	36	5.64
$Nb_{10}Mo_{13}W_7Ta_6$	"	-0.081	2.319	40	5.55
$Nb_{12}Mo_8W_9Ta_7$	"	-0.079	2.257	43	5.47
$(HfZrTi)_{12}$	HCP	0.036	3.802	77	4.0
$Nb_3(HfZrTi)_{11}$	HCP	0.066	3.949	153	4.08
$Nb_6(HfZrTi)_{10}$	BCC	0.066	4.042	285	4.16
$(NbHfZrTi)_9$	"	0.074	4.085	236	4.25
$Nb_{12}(HfZrTi)_8$	"	0.066	4.077	215	4.33
$Nb_{15}(HfZrTi)_7$	"	0.070	4.018	204	4.41
$Nb_{18}(HfZrTi)_6$	"	0.069	3.903	150	4.50
$Nb_{21}(HfZrTi)_5$	"	0.061	3.725	140	4.58

Table A4.5: Formation energies (H_f), Debye temperature (θ_D), Debye vibrational entropy at $T = 300$ K ($S_{\text{vib}}^{300\,\text{K}}$), ideal mixing entropy ($S_{\text{config}} = -k_B \sum_{i=1}^{n} c_i \ln c_i$, c_i is the concentration of ith component), total entropy ($S_{\text{tot}} = S_{\text{vib}}^{300\,\text{K}} + S_{\text{config}}$), and free energy ($H_f - TS_{\text{tot}}$) of favorable SQS of $Nb_x(HfZrTi)_y$ alloys ($x + 3y = 36$).

x	H_f (eV/atom)	θ_D (K)	$S_{\text{vib}}^{300\,\text{K}}$ (k_B/atom)	S_{config} (k_B/atom)	TS_{tot} (eV/atom)	$H_f - TS_{\text{tot}}$ (eV/atom)
0	0.036	289.3	4.191	1.098	0.137	-0.100
3	0.066	246.7	4.662	1.294	0.154	-0.088
6	0.066	234.0	4.802	1.366	0.160	-0.094
9	0.074	241.3	4.715	1.386	0.158	-0.084
12	0.066	247.3	4.644	1.369	0.155	-0.090
15	0.070	243.3	4.691	1.320	0.155	-0.085
18	0.069	236.0	4.780	1.242	0.156	-0.087
21	0.061	243.0	4.690	1.137	0.150	-0.090

Impact of Temperature on the Structural Transformation in $Nb_x(HfZrTi)_y$ HEAs

Here all the DFT calculations have been run at $T = 0$ K temperature. I have studied here the effect of Nb-concentration on the lattice structure of alloys within family $Nb_x(HfZrTi)_y$. We observe a phase transformation from HCP to BCC as the Nb-concentration is raised.

Elements {Hf, Zr, Ti} exist in HCP phase at low temperatures but they transform to BCC at high temperature [176], while Nb maintains BCC phase until it melts. Therefore, the ternary alloy HCP HfZrTi should also transform into BCC phase with increase in temperature (see Figure A4.7). The addition of Nb (x) should expedite the process of structural transformation by reducing the HCP→BCC transition temperature (T_C) of $Nb_x(HfZrTi)_y$. An increase in the concentration of Nb (x) should lower the transition temperature (T_C). We marked an HCP→BCC structural transformation in $Nb_x(HfZrTi)_y$ at 16.7% Nb-concentration at $T = 0$ K. But with increase in temperature, the required concentration of Nb (x) should decrease for an HCP→BCC transition to occur. Structural evolution of equiatomic NbHfZrTi with temperature [201] demonstrates its thermal stability in single phase BCC solid solution upto 673 K and then multiple structural transitions into different cubic symmetries are noted. Under

the extreme conditions, *in-situ* high-temperature and high-pressure synchrotron radiation X-ray diffraction measurements by Ahmad et al. [202] showed that NbHfZrTi HEA remains stable in a single BCC phase upto 1100 K and 80 GPa.
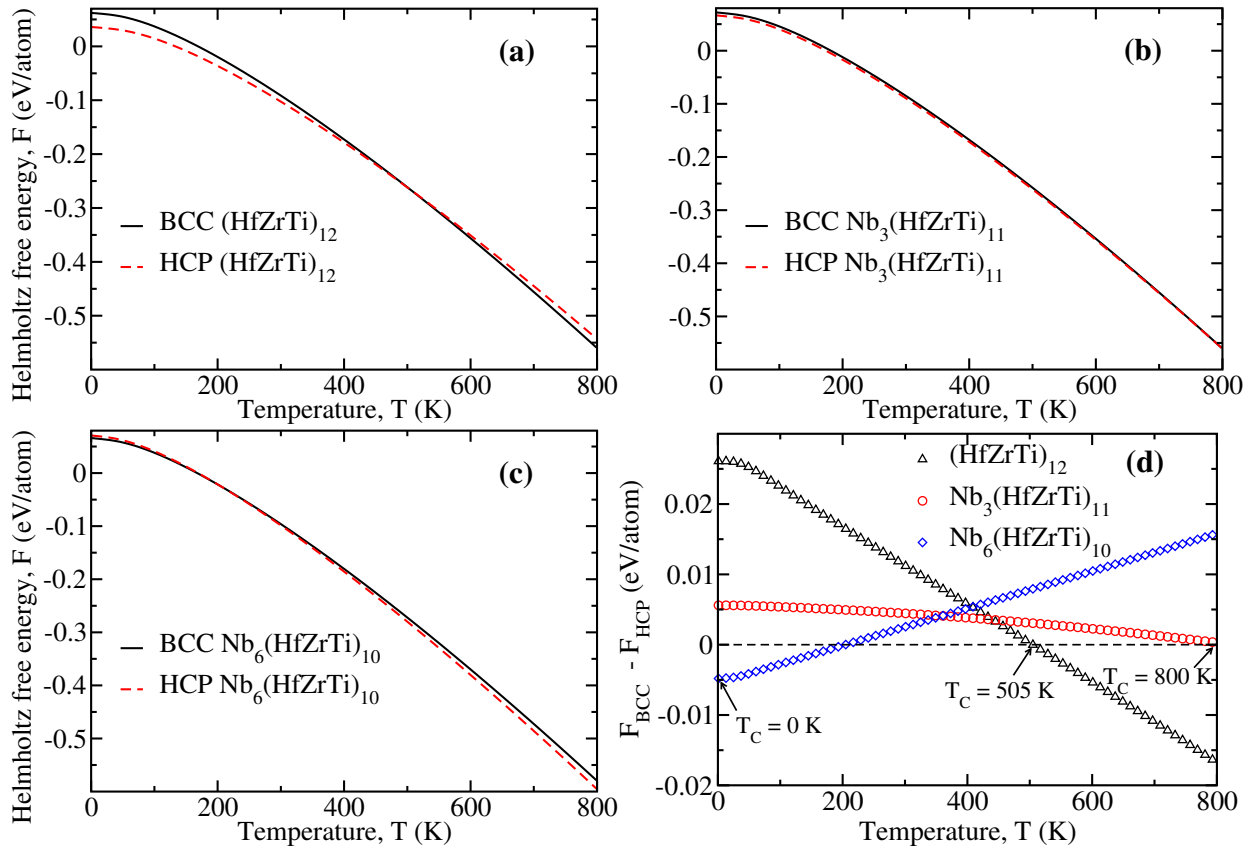
Figure A4.7: Helmholtz free energy ($F(T) = H_f - TS_{tot}(T)$) profiles of HCP and BCC structural special quasirandom configurations of HEAs. **(a,b)** $(HfZrTi)_{12}$ and $Nb_3(HfZrTi)_{11}$ are stable in HCP phase at low temperatures but eventually transform into BCC phase at particular temperatures. **(c)** $Nb_6(HfZrTi)_{10}$ is stable in BCC phase at $T = 0$ K and BCC structure is recovered on full ionic relaxation even if the host lattice of SQS is HCP (see Figure 4.1). **(d)** The relative Helmholtz free energies of BCC and HCP initialized SQS configurations of HEAs estimate their transition temperatures. HCP HfZrTi transforms into a BCC structure above 505 K.

Chapter 5

Anomalous Elastic Anisotropy and Mechanical Behavior of Nb$_x$(HfZrTi)$_y$ High-Entropy Alloys

5.1 Introduction

Alloys, the remarkable fusion of metals, have played an indispensable role in shaping the modern world, revolutionizing industries, and advancing technology. High-entropy alloys (HEAs) are a recent discovery that has stunned the materials science community. Comprising multiple principal elements in near equimolar proportions, HEAs possess an atomic-level complex environment that gives rise to their exceptional mechanical behavior [33, 34, 30]. HEAs have emerged as a remarkable class of materials that challenge traditional alloy design principles and offer an alternate route of materials design wherein stability is ensured by the high entropy of mixing [25]. The high-entropy design approach behind HEAs has also led the materials discovery in other fields such as ceramics[203, 204, 205, 206, 207, 208], metal-organic frameworks[209, 210], composites[211, 212], energy storage materials[213, 214], and others.

HEAs exhibit exceptional mechanical properties that distinguish them from conventional alloys [215, 28, 29, 30, 31, 32, 33, 34]. The inherent chemical complexity within HEAs causes solute-solution strengthening. The presence of complex, multi-component compositions, and

their structural diversity, which can include various crystal structures and phases, complicates the accurate modelling of HEAs [153]. Additionally, a large number of possible phases due to the Gibbs phase rule makes it computationally intensive to explore the entire composition space comprehensively [25, 26, 30]. Chemical disorder introduces computational challenges in the modelling of HEAs [216, 41]. Mechanical strength is the response of multi-scale effects [44, 45]. In this, crystal structure is the most essential criterion in determining the strength of a material. For example, BCC HEAs display higher yields but fail in a brittle manner, while FCC HEAs are ductile. The brittleness in BCC structural materials is caused by high energy slip planes which activate at high temperatures and ductile to brittle transition occurs. Then comes the kind of defects such as precipitate hardening, twinning, and ultimately phase transformation. The multicomponent nature of HEAs adds substitutional defects naturally in the lattice which causes internal lattice distortions and an inhomogeneous environment makes the atomic diffusion sluggish and dislocation dynamics *wavy* to strengthen the HEAs [41]. Under external loading, an HEA can show a cascade of events comprising stacking fault, twinning, structural transformation, and under the extreme load, amorphization [44, 45, 46, 47]. In the single-crystal HEAs, the primary mode of deformation which is marked first is through slip planes which can be analyzed theoretically using mechanical stability analysis given by Max Born [15, 108, 217].

In this work, we study the impact of Nb-concentration on the mechanical behavior of HEAs $Nb_x(HfZrTi)_y$ using first-principles theoretical analysis. We show that a continuous rise in Nb-concentration causes anomalous variation in elastic anisotropy and changes the failure mode from tetragonal shear to mixed to pure shear. We find a strength-ductility trade-off in single-crystals of $Nb_x(HfZrTi)_y$ as a function of Nb-concentration. We apply the mechanical stability analysis to estimate the actual tensile strengths of these HEAs and others. We trace a BCC to FCC Bain transformation path on the bond-orientational order parameters $(\bar{q}_8, \bar{q}_{12})$ plane.

5.2 Computational details

We simulate special quasirandom structures (SQS) [164, 165] of a few quaternary HEAs of $3 \times 3 \times 2$-size supercell of the conventional unit cell of BCC. The host lattice of only two alloys $(HfZrTi)_{12}$ and $Nb_3(HfZrTi)_{11}$ is chosen to be HCP due to their stability preference over the

BCC structure. We perform full structural relaxation of these model SQS alloys within the density functional theory (DFT) methods as implemented in the Quantum ESPRESSO software[138]. We used a generalized gradient approximation [139] and Perdew-Burke-Ernzerhof [140] functional of electronic exchange-correlation energy. We employ projector augmented wave potentials [172] and represent the electronic wave functions and charge density with plane wave basis sets truncated at energy cutoffs of 60 Ry and 500 Ry respectively. Uniform meshes of $3 \times 3 \times 4\,k$ -points and $3 \times 3 \times 3\,k$-points were used in sampling integrations over Brillouin zones of BCC- and HCP-based supercells respectively. We relax each structure using Hellman-Feynman forces and the Broyden Fletcher Goldfarb Shenno (BFGS) scheme till the force on each atom $\vec{F}$ is less than 10^{-3} Ry/Bohr. The energy convergence criterion for the electronic self-consistency was chosen as 10^{-8} Ry. Fermi-Dirac distribution with a width of $k_{\mathrm{B}}T = 0.002$ Ry is used for smearing the discontinuity in occupation of numbers of electronic states near Fermi energy.

Elastic properties of each alloy were extracted from their elastic constants matrix (**C**) obtained from the thermo_pw package [173]. Symmetry reduces the number of independent elastic constants [218] but intrinsic ILDs in HEAs [163] break the underlying symmetries and hence we assumed the lattice to be triclinic for elastic constants calculation. We strain the lattice by ∓ 1.5 % and ∓ 0.5 % for each six independent strain components ($\varepsilon_{11}, \varepsilon_{22}, \varepsilon_{33}, \varepsilon_{23}, \varepsilon_{13}$ and ε_{12}) and relax the atomic positions to get the optimized stress. The independent elastic constants are then estimated as the least-squares solution to a linear system of equations $\boldsymbol{\sigma} = \mathbf{C}\boldsymbol{\varepsilon}$. Since ILDs break the local symmetry of HEAs, we obtained 21 elastic constants (C_{ij} corresponding to a triclinic crystal [218]) which were further used for elastic moduli estimation following the Voigt-Reuss-Hill scheme [219] (see also Table 1 of reference [220]).

We used the universal elastic anisotropy index (A^U) [221] which is applicable for each crystal class to quantify anisotropy in a given alloy. A^U [221] requires the Voigt and Reuss estimates of shear ($G^{\mathrm{V}}, G^{\mathrm{R}}$) and bulk moduli ($B^{\mathrm{V}}, B^{\mathrm{R}}$) which are extracted from the elastic constants matrix (**C**) [219].

$$A^U = 5\frac{G^{\mathrm{V}}}{G^{\mathrm{R}}} + \frac{B^{\mathrm{V}}}{B^{\mathrm{R}}} - 6 \geq 0. \tag{5.1}$$

The departure of A^U from zero marks the degree of anisotropy in the material. An alternative way of qualitative understanding of elastic anisotropy is to determine the direction-dependent

sound speeds. We solve the Christoffel equation [222, 223] to get the group velocity of sound along a given direction.

We performed first-principles calculations to understand the mechanical behavior of HEAs. To estimate the tensile strength, we strained the BCC lattice kept in [100][010][001] coordinate frame along $<100>$ direction and relaxed the lattice along directions orthogonal to the strained axis to account for the Poisson effect. The strain is gradually increased and the optimized stress is noted to draw a stress-strain curve whose maximum stress is the tensile strength of a material. BCC crystals display minimum tensile strength along $<100>$ direction and their cleavage plane is $\{100\}$ [224].

To analyze the local structural evolution under uniaxial strain (ε_{11}), we characterize the geometries using the Voronoi cell construction around each atom and also examine the nearest-neighbor bonds alignment. For Voronoi analysis, we used the well-known Voro++ library [175]. The Voronoi cell constructed around an ideal BCC lattice point has 8 hexagons and 6 squares. We have unfolded a few Voronoi cells using JavaView visualization software [225] for better presentation. To examine the packing symmetry within the strained lattice, we calculated bond-orientational order parameters (q_l) for each atom using a recently developed Python library [174]. An ideal BCC lattice subjected to uniaxial strain transforms into a body-centered tetragonal and eventually into a face-centered cubic (FCC) lattice at a critical strain. The corresponding transformation path of BCC-BCT-FCC is known as the Bain path often represented with an energy landacape with varying strain [97]. Here, We trace the Bain transformation path in the bond-orientational order parameters ($\bar{q}_8, \bar{q}_{12}$) plane.

Some degree of chemical short-range ordering (CSRO) does exist in most of the high-entropy alloys [189]. By construction, the special quasirandom structures should have the least CSRO [164, 166]. We employ a swap Monte-Carlo (SwapMC) simulation to explore CSRO within a given HEA. The steps followed in this approach are: (i) start from a special quasirandom configuration, (ii) pick two distinct atoms at random and swap their positions, (ii) now relax the lattice to get the optimized energy, and (iv) if the swapping of the atoms lowers the energy then update the configuration else recover previous configuration and go to step (ii). We continue the swapping until the energy saturates at the ultrastable configuration. The degree of CSRO is determined by counting the first nearest-neighbor bonds formed between

various pairs of constituents within an HEA.

5.3 Results & Discussions

5.3.1 Elastic anisotropy

In general, crystalline materials exhibit anisotropy in a given property, in contrast, liquids and amorphous materials are isotropic. The lowering of continuous symmetry of liquids to discrete one of crystals leads to anisotropy. Although monatomic crystals are anisotropic, the chemical disorder present in the crystalline phase of HEA may induce isotropy due to random scattering sites. Thus knowledge of elastic anisotropy i.e. the direction-dependent mechanical response of HEAs is fundamentally interesting and essential for their optimal performance in application.

(1) Elastic anisotropy index

Elastic anisotropy can be quantified by measuring and characterizing the material's elastic constants along different directions, which have a tensorial form. The symmetries of a given crystal constrain the number of independent elastic constants [218, 226]. For example, at the extreme ends of symmetry classes, isotropic material has only two independent elastic constants μ and λ (known as Laḿe coefficients), and triclinic material requires full 21 componenets of elastic constants [218, 226]. Zener anisotropy index [227], a single-valued quantity defined only for cubic crystals with three elastic constants $\{C_{11}, C_{12}, C_{44}\}$, is not applicable to measure anisotropy of HEAs. Most of the existing HEAs are of either cubic (requiring 3 elastic constants) or hexagonal symmetry (requiring 5 elastic constants). Still, the intrinsic "internal lattice distortions" (ILDs) in HEAs [163] break the symmetry and make the underlying lattice triclinic (but close to cubic) on the finer atomic-level resolution. Thus, a singular measure of anisotropy applicable to each symmetry class is desired, and the "universal elastic anisotropy index" (A^U) [221] being one such measure. The definition of A^U [221] (see eq 5.1) considers the ratio of the upper (Voigt) and lower (Reuss) bounds on the shear (G^V, G^R) and bulk modulus (B^V, B^R) to infer anisotropy as both bounds converge for an isotropic material [219]. The degree of anisotropy depends on the extent of departure of A^U from zero.

Interestingly, BCC Nb is elastically quite anisotropic (see Figure 5.1(a)). Anomalous elastic anisotropy of Nb is caused by softening of C_{44} [228]. Ternary alloy HfZrTi of HCP structure is

nearly isotropic with its $A^U = 0.05$. We already know that $Nb_xHfZrTi$ HEAs exhibit a structural transformation from HCP to BCC phase with increase in Nb-concentration [178]. With the gradual increment in Nb-concentration (x), we expect a monotonic rise in elastic anisotropy of $Nb_xHfZrTi$ due to the high anisotropic nature of Nb. On the contrary, we observe a continuous decline of A^U with x after the structural transition till $Nb_{21}(HfZrTi)_5$ configuration, and then it rises again (see Figure 5.1(a)). The structural transition from HCP→BCC first controls this anomalous variation in anisotropy, and then the expected rise in A^U is observed once the atomic concentration of Nb exceeds 60% (i.e $x > 21$). Thus, the elastic anisotropy in $Nb_x(HfZrTi)_y$ is an entangled effect of structural transition and anomalous elastic behavior of Nb.
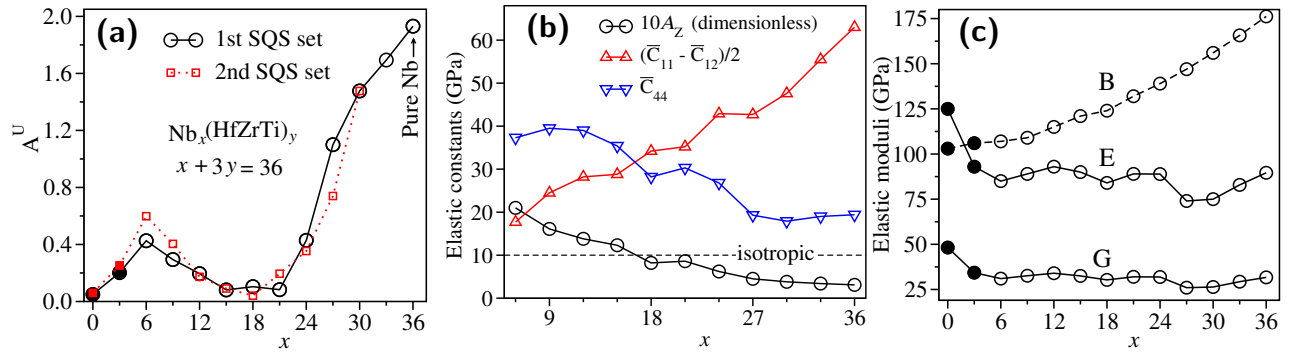
Figure 5.1: Effect of Nb-concentration (x) on the elastic properties of $Nb_x(HfZrTi)_y$: (a) Universal elastic anisotropy index decreases ($A^U = 0$ means isotropy) on either side of HCP (filled symbol)→BCC (open symbol) transition at $x = 6$, but it increases again at higher Nb-concentration ($x > 21$). This anomalous variation in anisotropy is also seen through (b) the Zener ratio, $A_Z = 2C_{44}/(C_{11} - C_{12})$), which is defined only for cubic crystals (here, $x \geq 6$ configurations are BCC). Similar to A^U, A_Z also grows on the either side of $Nb_{18}(HfZrTi)_6$ as it deviates from 1 (isotropic). Increasing Nb-concentration softens C_{44} which makes the system prone to a pure shear failure. (c) Young's modulus (E) and shear modulus (G) decrease drastically before saturating in the BCC phase while bulk modulus (B) displays a monotonic rise with x.

(2) Direction dependent sound velocity

Another measure of elastic anisotropy is the directional sound velocities. In experiments, elastic anisotropy is measured using ultrasonic methods which involve the propagation of ultrasonic sound waves through a material to determine its elastic properties. By measuring the velocity of ultrasonic waves along different directions within the material, one derives elastic constants. Here, with the knowledge of elastic constants (calculated using first-principles calculations) of a material, we estimate directional sound velocities. In a solid, there exist two types of elastic waves. The primary wave tends the particle to vibrate in the direction along the wavevector, and

the secondary wave causes the particle to vibrate perpendicular to the wavevector. In general, the primary wave travels faster than the secondary wave. For instance, in an isotropic medium, the group velocities of primary and secondary waves are

$$v_{\text{iso}}^{\text{p}} = \sqrt{(B+4G/3)/\rho} \quad \text{and} \quad v_{\text{iso}}^{\text{s}} = \sqrt{G/\rho} \tag{5.2}$$

respectively. Here, B is the bulk modulus, G is the shear modulus, and ρ is the density of isotropic material. In an anisotropic material, group velocities of sound in each direction are determined after solving the Christoffel equation [223, 222] for dispersion relation as given below

$$\sum_{ij} \left[M_{ij} - \rho\omega^2\delta_{ij} \right] \alpha_i = 0 \quad \text{where} \quad M_{ij} = \sum_{mn} q_m C_{imnj} q_n \tag{5.3}$$

and q is wavevector of elastic wave having frequency ω and polarization $\hat{\alpha}$ in a material with density ρ. It is routine to write elasticity tensor $\mathbf{C}$ in Voigt notation of 6×6 matrix, but here $\mathbf{C}$ is the 4th rank tensor wherein each index runs from 1 to 3. The solution of eq 5.3 gives three frequencies and polarizations (one belongs to the primary wave while the other two belong to secondary waves) for each q. Taking the derivative of the dispersion relation $\omega(q)$ with respect to the wavevector fetches the group velocity of sound (v_g).

In Figure 5.2, we show the deviation of calculated directional sound velocities in alloys $Nb_x(HfZrTi)_y$ from their corresponding isotropic sound velocities ($\Delta v = v_g - v_{\text{iso}}$) which highlights the elastic anisotropy qualitatively. We find that Nb-free configuration i.e. HCP $(HfZrTi)_{12}$ alloy which is composed of only HCP elements is close to an isotropic alloy as Δv stands within $\pm 4\%$ for primary and $\pm 7\%$ for secondary waves. The addition of Nb brings the anisotropy (A^U) in $Nb_3(HfZrTi)_{11}$ (Figure 5.1(a)), and develops maximum anisotropy for $Nb_6(HfZrTi)_{10}$ (Δv lies within $\pm 7\%$ for primary and $\pm 20\%$ for secondary waves). Interestingly, it has been shown that $Nb_6(HfZrTi)_{10}$ also marks the juncture of an HCP$\rightarrow$BCC transition accompanying a severely distorted lattice characterized by a large ILDs. Post transition, the anisotropy declines with growing Nb-concentration till the configuration $Nb_{21}(HfZrTi)_5$ whose anisotropy is similar to $(HfZrTi)_{12}$ (see Figures 5.1(a) and 5.2). When the Nb-concentration exceeds 60%, sound velocity becomes direction-dependent and for the case of bulk Nb (i.e $x = 36$) which is elastically anomalous [228], Δv varies within $\pm 7\%$ for

primary and $\pm 50\%$ for secondary waves. We notice that a large anisotropy in $Nb_x(HfZrTi)_y$ arises when the speed of secondary waves significantly deviates from that in an isotropic medium. A crude way to represent this may be $A^U \propto v^s - v_{iso}^s$. This anomalous variation in anisotropy is linked to two factors: i) HCP$\rightarrow$BCC transition at 16% Nb-concentration (i.e. $x = 6$), and ii) the anomalous elastic feature of bulk Nb. In general, the addition of Nb with highly anisotropic behavior should have increased the anisotropy of the alloy monotonically but the structural transition intercepts this trend as large ILDs in the vicinity of structural transition scatter the sound in random directions, making the alloy isotropic. Once the lattice distortions reduce significantly at higher Nb concentration, the role of Nb becomes apparent in causing enhancement in the overall anisotropy.
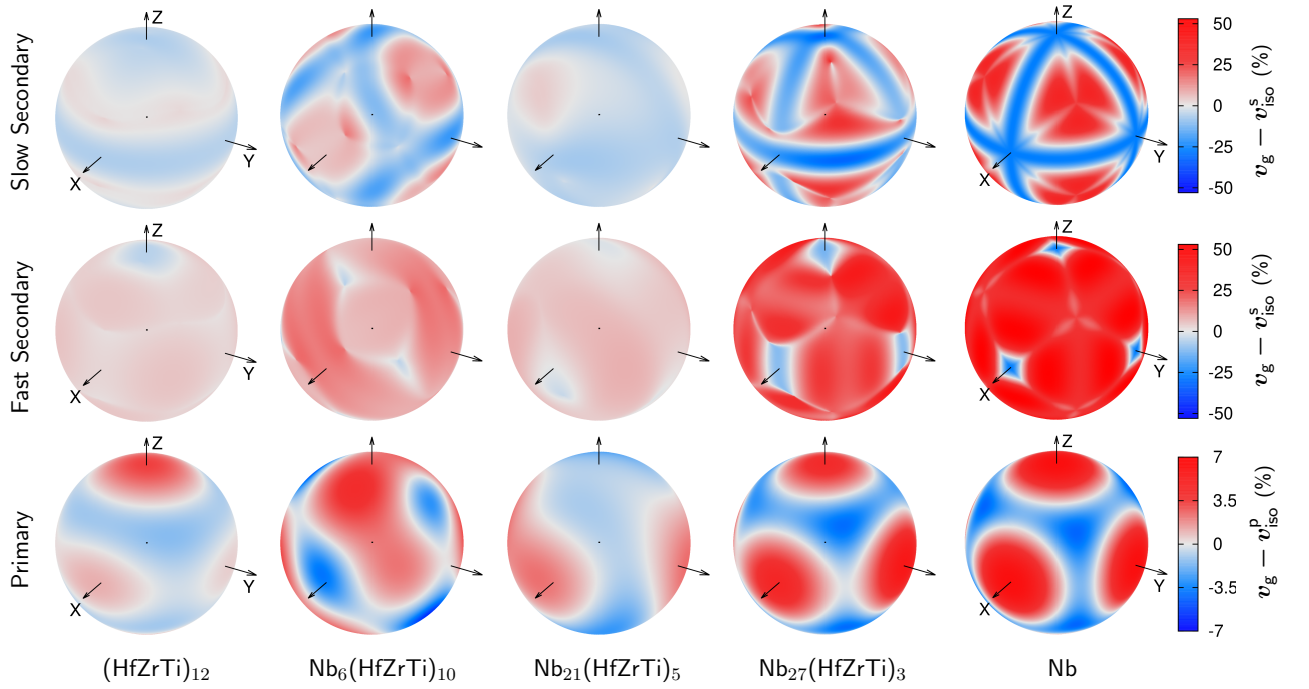
Figure 5.2: Anomalous variation of elastic anisotropy in Nb-Hf-Zr-Ti: Projection of longitudinal (primary) and two transverse (secondary) group velocities of sound on a sphere relative to their velocities in an isotropic same density solid characterizes anisotropy in alloys. Nb is elastically very anisotropic due to soft C_{44}, which addition to nearly isotropic $(HfZrTi)_{12}$ develops anisotropy in $Nb_6(HfZrTi)_{10}$. Then surprisingly, anisotropy decreases with increasing Nb-concentration and makes $Nb_{21}(HfZrTi)_7$ again nearly isotropic (see also Figure 5.1). Anisotropy increases monotonically beyond $Nb_{21}(HfZrTi)_5$ owing to anomalous elastic behavior of Nb.

(3) Elastic Property

In cubic materials, C_{11}, C_{12}, and C_{44} are the 3 independent components of their elastic constants matrix **C**. With loss of materials symmetries, the number of independent elastic

constants increases [218] up to 21 for the extreme case of a triclinic crystal. The elastic constants matrix $\mathbf{C}$ contains all the linear elastic properties of a material [220] as I discussed above the elastic anisotropy index and sound velocities derived from $\mathbf{C}$. Although the average structure of most of the HEAs is either BCC, FCC, or HCP, their intrinsic internal lattice distortions (ILDs) break the symmetry at the atomic scale and make the underlying lattice locally triclinic. The slight deviation in the internal from the reference ideal lattice (here BCC) modifies each element C_{ij} by a small amount from the elastic constants matrix of an ideal lattice giving a total of 21 independent terms. For example, we have given below the elastic constants matrix of BCC $(NbHfZrTi)_9$ modelled with $3 \times 3 \times 2$-size periodic supercell of BCC unit cell,

$$\mathbf{C} = \begin{bmatrix} 144 & 91 & 96 & 0 & 0 & 0 \\ 91 & 143 & 92 & 0 & 0 & -2 \\ 96 & 92 & 140 & 0 & 0 & 0 \\ 0 & 0 & 0 & 37 & 0 & 0 \\ 0 & 0 & 0 & 0 & 41 & 1 \\ 0 & -2 & 0 & 0 & 1 & 40 \end{bmatrix}$$

Sometimes, to mimic the elastic constants matrix of an ideal cubic material, we take the arithmetic mean of degenerate C_{ij}s.

Now, we investigate the effect of Nb-concentration on the elastic properties of HEAs $Nb_x(HfZrTi)_y$ (see Figure 5.1(b) and (c)). To estimate the Zener anisotropy ratio (A_Z) [227], which is the fractional difference between the two shear moduli C' and C_{44} of a cubic material, we write the averaged version of the three elastic constants of the BCC configurations ($x \geq 6$) of $Nb_x(HfZrTi)_y$ as follows

$$\bar{C}_{11} = \frac{C_{11} + C_{22} + C_{33}}{3}, \ \bar{C}_{12} = \frac{C_{12} + C_{13} + C_{23}}{3}, \text{ and } \bar{C}_{44} = \frac{C_{44} + C_{55} + C_{66}}{3}.$$

In Figure 5.1(b), we note that $C' = (C_{11} - C_{12})/2$ increases steadily while C_{44} reduces with increasing concentration of Nb. $C'(x)$ and $C_{44}(x)$ intersect each-other near $x = 18$ and the resultant alloy becomes isotropic with the ratio $A_Z = 1$. The switching of shear moduli from $C' < C_{44}$ to $C_{44} < C'$ should inflict a switching of their failure mechanisms too. At a lower concentration of Nb, the BCC phase of $Nb_x(HfZrTi)_y$ has a poor stability marked by a low

value of C' ($< C_{44}$). In a very recent study [229], the HCP to BCC phase transformation in $Nb_x(HfZrTi)_y$ as a function of increasing Nb-concentration has been discussed based on the Born's elastic stability analysis [15]. The crossover between C' and C_{44} has been found in several binary alloys as a function of the concentration of the alloying element. For example, the authors of ref. [97] present a similar trend in C' and C_{44} in BCC Zr-Nb-Mo binary solid solution series (Figure 34 of ref. [97]). Such a contrary variation in these two shear moduli causes the Zener ratio (A_Z) to have values $A_Z > 1$ and $A_Z < 1$. The extent of deviation of A_Z from 1 on either side represents the degree of anisotropy. Thus, A_Z quantitatively (but not as precise as A^U which is defined for any crystal class) shows the anomalous variation in elastic anisotropy within the BCC configurations of $Nb_x(HfZrTi)_y$ HEAs.

In Figure 5.1(c), we show that Young's modulus (E) and shear modulus (G) drops drastically near the HCP→BCC transition (i.e. $x = 6$) and thereafter decrease slowly with rising Nb-concentration. On the other hand, bulk modulus (B) continues to rise without showing any abrupt behavior across the structural transition. Pugh ratio (G/B) predicts the possible failure mode of a material [230, 231]. A high value of G/B implies brittle failure, while a low value (i.e. high B/G) implies the ductile failure associated with plastic deformation [230, 231]. Continuous rise in the bulk modulus and reduction in shear modulus with increasing Nb-concentration improves the ductility of $Nb_x(HfZrTi)_y$ (see Table 5.3). Such a strong dependence of elastic properties on the composition has not been seen in another set of quaternary HEAs Nb-Mo-W-Ta and binary alloys Mo-W which are composed of only the elements occuring in the BCC structure (see Table 5.3).

5.3.2 Tensile strength

Mechanical properties comprise both small and large strain responses of a given material. Elastic moduli are derived for responses at small strains, while mechanical strength is associated with a large strain, given by the extreme load a material can sustain before undergoing failure. Mechanical strength depends on the mode of deformation. Ultimate tensile strength is the stress needed to break a single-crystal material under uniaxial deformation and shear strength is the stress at which a material fails under shear deformation. Here, we present first-principles calculations to estimate the tensile strengths of a few BCC high-entropy alloys

mostly of the Nb-Hf-Zr-Ti family. The configurations under study are defect-free single-crystals and hence their strengths are expected to be much higher in comparison to the experimentally measured strengths.

We apply uniaxial tensile strain on an SQS configurations of BCC HEAs along $< 100 >$ in a quasi-static manner and relax the lattice orthogonal to $< 100 >$ to include Poisson's contraction. Figure 5.3 shows that the strained geometries of HEAs Nb-Hf-Zr-Ti can be easily optimized up to 20% strain, but those of Nb-Mo-W-Ta are hard to optimize for strains beyond 14%. From the Figure 5.3(a), we observe an improvement in the tensile strength (which is the peak engineering stress σ_{11}^{max}) of $Nb_x(HfZrTi)_y$ with increase in the Nb-concentration (x). On the contrary, HEAs Nb-Mo-W-Ta and binary alloys Mo-W whose constituents are pure BCC elements exhibit a weak dependence of tensile strength on their composition (see Figure 5.3(b)).
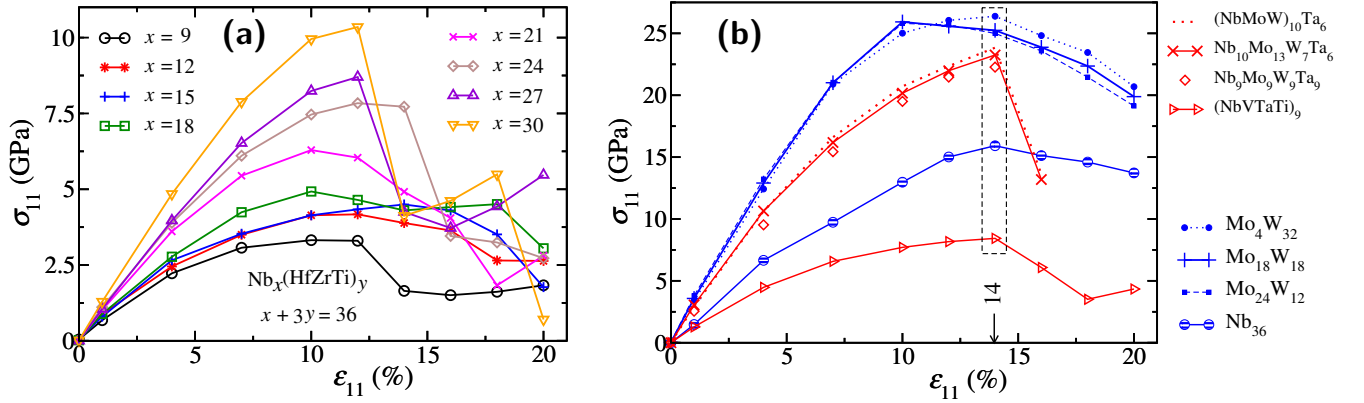
Figure 5.3: First-principles uniaxial deformation along $< 100 >$ of BCC (a) $Nb_x(HfZrTi)_y$, (b) other quaternary and binary alloys. These single-crystal BCC alloys exhibit peak stress (called tensile strength) somewhere between (10-14)% strain (ε_{11}). The tensile strength of $Nb_x(HfZrTi)_y$ strongly correlates with Nb-concentration, in contrast to HEAs Nb-Mo-W-Ta (composed of BCC elements) which trace identical stress-strain curves. Although we can elongate the lattice of these alloys theoretically up to a large strain, the elastic stability analysis needs to be done to reveal their actual pre-failure elongation and tensile strength.

To explain the strong dependency of Nb-content on the mechanical strength of $Nb_x(HfZrTi)_y$, we calculate the internal lattice distortions (ILDs) present in their stress-free configurations using equation (4.3) of Chapter 4. In Figure 5.4(a), we demonstrate that increase in Nb-concentration (i.e. x) causes a gradual reduction of ILDs within the resultant HEA (see inset) which in turn enhances their tensile strength. Thus, there exists a trade-off between the intrinsic ILDs and the strength of a material: an alloy with higher ILDs displays poor strength. It is further supported by the theories of melting such as Lindemann [232, 233] and the Born
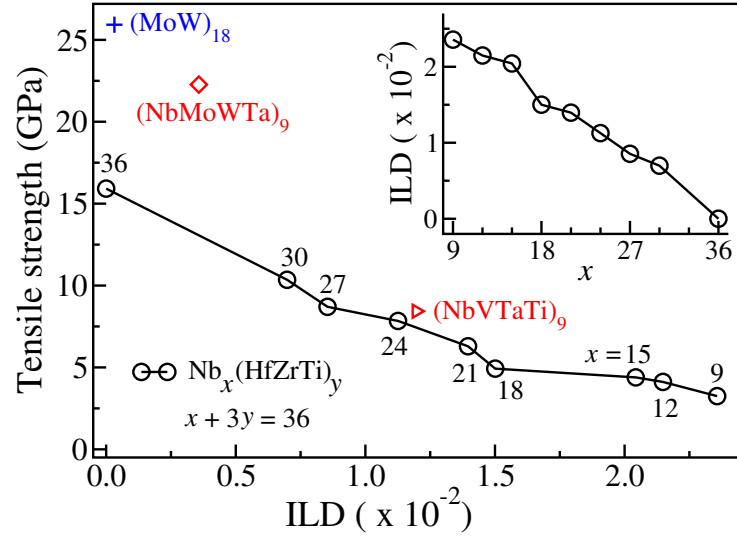
Figure 5.4: Impact of intrinsic lattice distortions on the tensile strength of BCC high-entropy alloys. The magnitude of ILDs can be regarded as an amorphization parameter that reduces the material's ideal strength. ILDs in BCC $Nb_x(HfZrTi)_y$ HEAs decrease with an increase in Nb-concentration(see inset) meaning the lattice is restoring to an ideal BCC structure, which in turn enhances their ideal tensile strengths.

criteria [15] of melting. According to the Lindemann criterion, a material melts when the average amplitude of atomic vibration around its equilibrium reaches about 10% of their interatomic separation, while the Born criterion states the vanishing of shear modulus (primarily C') near melting. The former theory refers to thermodynamical melting while the latter one is shear-induced, so termed mechanical, melting [234]. ILDs are similar to the thermally induced off-lattice displacements of atoms but are static in nature [163]. We should caution that ILDs are static displacements present in HEAs even at $T = 0$ K and these can approach to Lindemann limit while maintaining a solid phase [179].

ILDs can be regarded as the dilute limit of amorphization of a material. In high-entropy alloys, the multicomponent mixture of atoms of different radii and chemical properties cause off-lattice (nonaffine) displacements to bring the lattice in equilibrium by canceling out the internal forces [234, 235]. When the average displacement of such nonaffine perturbations of atoms reaches the Lindemann criterion, the materials become too soft and melt. In Figure 5.4, we show that with the rise in Nb-concentration in $Nb_x(HfZrTi)_y$, ILDs get gradually weaker due to restoration of underlying lattice towards an ideal BCC. Therefore, we see an improvement in the (tensile) strength with decreasing ILDs. Born's criterion of melting also explains why a rise in Nb-concentration improves the strength of $Nb_x(HfZrTi)_y$. As we see in

Figure 5.1(b), tetragonal shear modulus $C' = \dfrac{C_{11} - C_{12}}{2}$ (which vanishes near melting) continuously increases with Nb-concentration and makes those HEAs stronger. At the same time, the rhombohedral shear modulus C_{44} declines with x but slower than the increase in C'. The lower value of C' correlates with large ILDs within a given system as this shear modulus softens and is more relevant to melting in Born's criterion.

In Table 5.1, we compare the DFT estimated strength of BCC NbHfZrTi with a few experimentally measured strengths. We find that the computationally estimated failure strain (ε_f^*) is close to the experimental values, while calculated peak stress (UTS) is about four times higher than the experimental ones. The inclusion of crystallographic defects for disordered alloys such as HEAs will enormously enlarge the system size needed and will make the computation infeasible. Hence, the computed strength here will be a theoretical maximum of the strength exhibited by a defect-free specimen of a given material. The nanoscale specimen of materials which contain very few defects can achieve these thoretical strengths. For instance, nanoscale single-crystalline diamond deforms elastically upto 9% strain and corresponding ultimate tensile strength (UTS) reaches 95 GPa [236] which is the theoretical (ideal) tensile strength of diamond [237]. Our computed strengths of HEAs are thus the maximum limit of strength and become relevant to the HEAs designed on nanoscale.

Table 5.1: Comparison of computational mechanical properties of NbHfZrTi with experiments.

Method	a (Å)	E (GPa)	B (GPa)	G (GPa)	UTS (GPa)	ε_f^* (%)
DFT (This work)	3.428	89	109	32.6	3.3	14
Expt. [238]	3.444	69.7	105.7	25.1	—	—
Expt. [239]	—	—	—	—	0.8	14
Expt. [240]	—	—	—	—	0.97	14.9
Expt. [35]	3.444	—	—	—	0.82	14.2

5.3.3 Bain path: Mechanisms of Deformation

If the cubic unit cell of the BCC lattice is stretched by factors of $\sqrt{2}$, 1, 1 along crystallographic directions then the lattice transforms into a face-centered cubic (FCC) structure. It was first

pointed out by Bain around a hundred years ago [105]. Under the uniaxial deformation of BCC lattice, the orthogonal directions contract due to the Poisson effect, and the resultant structure becomes body-centered tetragonal and ultimately goes into an FCC lattice as illustrated in Figure 5.5(a). This geometrical constraint of Bain transformation is hardly achieved in practice due to the material's failure at a much lower strain. The corresponding strain energy landscape of BCC-BCT-FCC is called the Bain transformation path.

In Figure 5.5(b), we draw the Bain paths of a few BCC structured alloys for tensile strain along $< 100 >$-direction. In principle, the gradual rise in tensile strain should drive these BCC configurations toward FCC. As the FCC phase achieved by straining a stable BCC configuration is metastable, the strain energy will keep increasing. From Figure 5.5(b), we identify that HEA NbHfZrTi – composed of BCC (Nb) and HCP (Hf, Zr, Ti) elements – requires less energy than NbMoWTa whose each constituent is BCC element. It is the common routine in the synthesis of high-strength materials to mix BCC and HCP elements. Such a cross mixing overcomes the strength-ductility trade-off in HEAs too [27, 39, 241]. Therefore, a low Bain barrier caused by HCP elements in NbHfZrTi makes it prone to transformation-induced plasticity (TRIP), while NbMoWTa fails in a brittle manner marked by a sudden loss of stress (see Figure 5.3). The Bain barrier also decreases due to the amplification of ILDs within HEAs. For example, pure Nb has an ideal BCC lattice but the substitutional addition of HCP elements distorts the internal lattice (see inset of Figure 5.4). In Figure 5.5(b), niobium which has no ILDs requires a large energy barrier to adopt an FCC lattice, while HEAs $Nb_x(HfZrTi)_y$ with severe ILDs such as NbHfZrTi requires a much lower strain energy to transform into an FCC structure. In addition, the volume of an alloy constituted of only BCC structural elements increases with tensile strain (except Nb-Mo-W-Ta beyond 14% strain), but several strained configurations with volume drop than preceding configuration are noted for BCC and HCP mixed elements HEAs (see Figure 5.5(c)). To understand, the origin of volume drop at a few strained configurations, we characterize the underlying lattice using two structural descriptors – (1) face analysis of Voronoi cells and (2) bond-orientational order parameters (see appendix of Chapter 4 for a detailed description of these two descriptors).

We performed Voronoi partitioning of strained lattice configuration and analyzed the geometry of Voronoi cells around each atom. The face analysis is a strong identifier among different
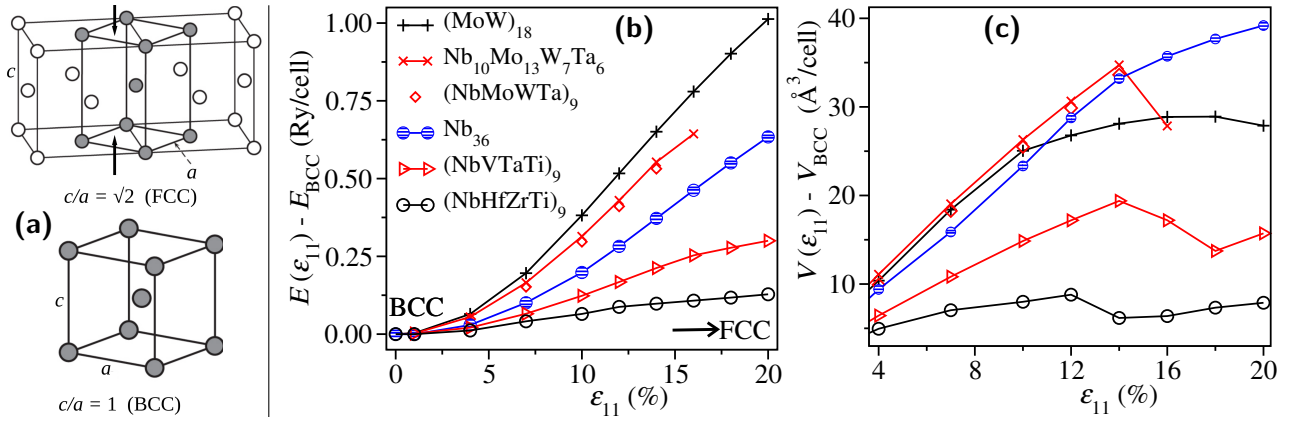
Figure 5.5: (a) The schematic of FCC→BCC (or vice-versa) Bain transformation under uniaxial compression (tension) via body-centered tetragonal structures (shown with filled sphere sublattice). The Bain transformation from BCC to FCC is complete once the geometrical constraint $c(\varepsilon) = \sqrt{2}a(\varepsilon)$ is satisfied at a tensile strain ε which depends on the Poisson's ratio of the material. (b) Bain path (energy versus strain curve) approaching an FCC lattice under uniaxial deformation of $3 \times 3 \times 2$-size supercell of BCC along $< 100 >$ direction. A low Bain energy barrier makes an alloy ductile possibly by transformation-induced plasticity (TRIP) effect evident by the appearance of Voronoi pentagons in Figure 5.6(b) for strained Nb-Hf-Zr-Ti. This explains the origin of a large failure strain of 14% in NbHfZrTi while pure Nb fails at 6% strain only (see Figure 5.8) as it has a large Bain barrier and no pentagonal Voronoi faces. (c) The emergence of pentagonal Voronoi faces makes the system densely packed [242]. Therefore, we note a volume drop once Voronoi pentagons appear in the strained configurations of HEAs.

crystal classes (see Figure 5.6(a)), for example, the Voronoi cell constructed around a BCC lattice point has 6 square and 8 hexagonal faces, that around an HCP lattice point has 6 trapeziums and 6 rhombic faces, and that of an FCC lattice point has 12 rhombic faces. The order of each Voronoi vertex in BCC is 3 (type-**A**) which is robust against any lattice perturbation and as a consequence of this, no new polygonal face emerges (only quadrilaterals and hexagons are present). While the Voronoi cells of strained HCP and FCC lattices yield pentagonal faces at the order 4 (type-**B**) Voronoi vertices [103]. Geometrically, it is obvious that the BCC lattice under uniaxial strain will be converted into an FCC lattice at a particular Bain strain. In terms of Voronoi face analysis, this BCC→FCC transformation corresponds to converting a truncated octahedron into a rhombic dodecahedron. For an ideal BCC lattice, the two faces of each Voronoi (octahedron) cell will be annihilated by shrinking their areas and hexagons will be converted into rhombuses with increasing strain to restore the Voronoi (dodecahedron) cell of an HCP lattice point (see the unfolded Voronoi cells in Figure 5.6(c)). In this BCC →FCC transformation, the Voronoi cell will evolve with strain but the face characteristics should remain invariant when the lattice is in the BCC regime, and intrinsic ILDs will produce pentagons at type-**B** Voronoi vertices once the FCC regime is close. On the contrary, we mark the onset of Voronoi pentagons near 12% strain for BCC $Nb_x(HfZrTi)_y$ HEAs and they grow in number with further strains, see Figure 5.6(b). Voronoi pentagons predominantly appear in those HEAs that comprise at least one HCP element (e.g. BCC NbVTaTi). Therefore, an HCP-like local rearrangement (HCP has type-**B** Voronoi vertices too) under strain can also cause the origins of pentagonal Voronoi faces.

We draw the Bain transformation path of BCC to FCC under uniaxial deformation on the $(\bar{q}_8, \bar{q}_{12})$ plane, see Figure 5.7. The negligible ILDs within a BCC system draw a smooth C-like Bain curve on the $(\bar{q}_8, \bar{q}_{12})$ plane. We see that binary MoW alloy (which have negligible ILDs and hence no pentagons) follows the expected BCC→FCC transformation path but high-entropy alloys deviate from this due to the appearance of pentagonal Voronoi faces (see Figure 5.7(b)). This deviation caused by ILDs which led to the origin of pentagons in near FCC regime (or in locally rearranged HCP region) highlights the TRIP effect in $Nb_x(HfZrTi)_y$ high-entropy alloys. On the other hand, Nb-Mo-W-Ta-based BCC HEAs have relatively lower ILDs and hence they follow the ideal Bain path up to 14% strain and suddenly distance away for 16% strain due to the appearance of pentagons in a huge number (see Figure 5.7(a)).
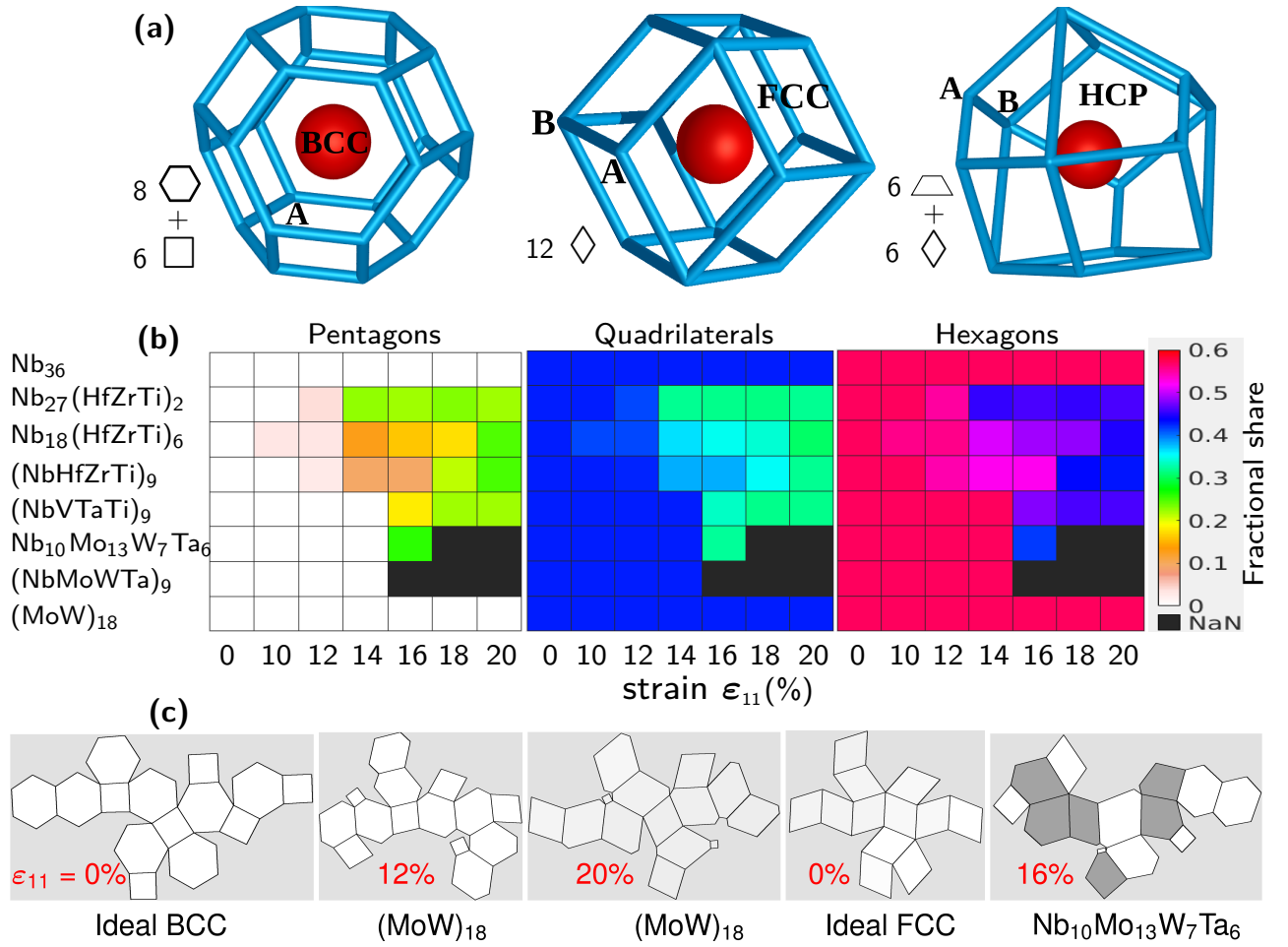
Figure 5.6: (a) Voronoi cells around an ideal BCC, FCC, and HCP lattice point. (b) Voronoi cell analysis of uniaxially strained structures of BCC high-entropy alloys. The Voronoi cell constructed around an ideal BCC lattice point has only regular squares and hexagons. The emergence of pentagonal Voronoi faces in uniaxially strained configurations of BCC lattice is unusual as their presence is not expected for the Voronoi cell of order 3 (type-**A**) vertices [103]. Even the presence of internal lattice distortions (ILDs) in BCC HEAs only makes the Voronoi faces irregular but does not produce any pentagon (see Figure A4.1). Under uniaxial deformation, a BCC lattice transforms to an FCC lattice which has order 4 (type-**B**) Voronoi vertices too. Order 4 Voronoi vertices are topologically unstable and pentagons emerge there in the presence of notable ILDs [103]. Therefore, (b) Pentagons emerge at lower strains in Voronoi cells of $Nb_x(HfZrTi)_y$, and their share rises while diminishing the shares of quadrilaterals and hexagons as we move towards FCC with increasing strain. Voronoi cells of HEAs (Nb-Mo-W-Ta) composed of only BCC elements do not have pentagons up to maximum stress configuration because of low ILDs in them (true for MoW and Nb too). (c) We unfolded a single Voronoi cell to see the effect of uniaxial strain on its face characteristics. The Voronoi cell around an ideal BCC lattice point has only regular squares and hexagons which eventually transform into regular rhombuses corresponding to the FCC phase [103] at the Bain strain. For instance, each Voronoi cell of BCC MoW (14 faces) smoothly progresses towards the Voronoi cell of an FCC lattice (12 faces) by shrinking two squares to annihilation and converting others into rhombuses.
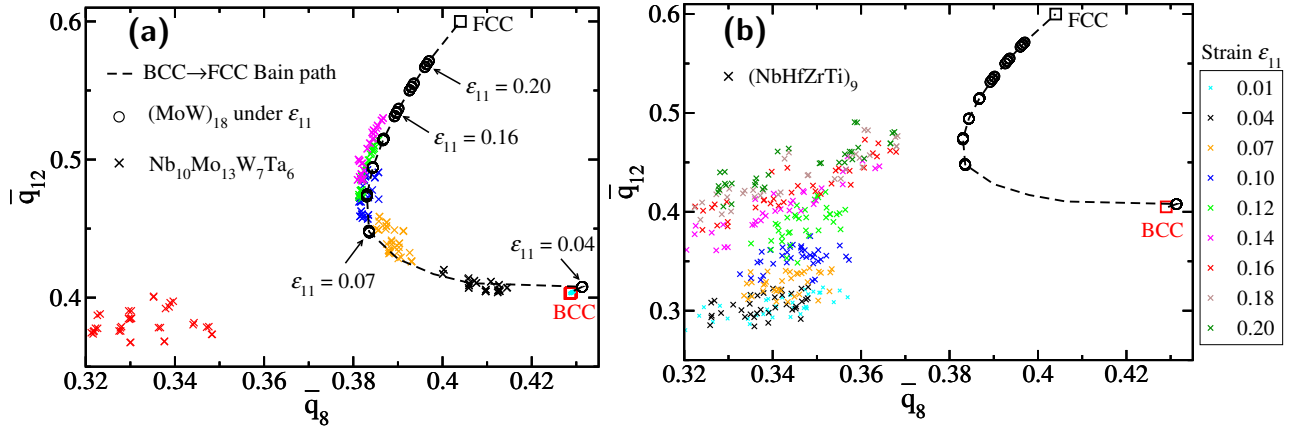
Figure 5.7: (a) Bain transformation path of an ideal BCC lattice to an FCC lattice via body-centered tetragonal structures traces a C-curve on the bond-orientational order parameters $(\bar{q}_8, \bar{q}_{12})$ plane. HEA $Nb_{10}Mo_{13}W_7Ta_6$, composed of only BCC elements, follow the Bain path up to the maximum stress configuration corresponding to $\varepsilon_{11} = 14\%$ (see Figure 5.3(b)) and then branches away due to an unprecedented emergence of pentagonal Voronoi faces in an enormous number (see Figure 5.6). On the other hand, (b) BCC configurations of HEAs $Nb_x(HfZrTi)_y$ (shown here for equiatomic configuration) which are composed of BCC and HCP elements distance away from the ideal C-type Bain path due to relatively larger intrinsic ILDs and the appearance of Voronoi pentagons at lower strains (Figure 5.6).

5.3.4 Mechanical stability test and failure mode analysis

To check whether the material is mechanically stable, we apply the well-known Born's criteria [15] which require each eigenvalue (λ_i) of the elastic constants matrix $\mathbf{C}$ to be positive and $\det|\mathbf{C}| > 0$. For example, the mechanical stability of a cubic crystal which has 3 independent elastic constants C_{11}, C_{12}, and C_{44}, requires the positive definiteness of each eigenvalue of $\mathbf{C}$ i.e. $\lambda_1 \rightarrow C_{11} + 2C_{12} > 0$, $\lambda_2 \rightarrow C_{11} > C_{12}$, and $\lambda_3 \rightarrow C_{44} > 0$. The associated eigenvectors with these three eigenvalues are $(1,1,1,0,0,0)\delta\eta$, $(\delta\eta_{xx}, \delta\eta_{yy}, \delta\eta_{zz}, 0, 0, 0)$, and $(0,0,0,\delta\eta_{yz},0,0)$ respectively, where $\delta\eta_{xx} + \delta\eta_{yy} + \delta\eta_{zz} = 0$ if the volume remains conserved under deformation. Therefore, the vanishing of C_{44} causes pure shear instability, while the vanishing of tetragonal shear modulus $C' = (C_{11} - C_{12})/2$ is termed Born's instability due to its disappearance near mechanical melting as defined by Max Born [108, 15].

Under external stress (σ), the Born's criteria get modified slightly to $\det|\mathbf{C} + \mathbf{\Delta}| > 0$ where $\mathbf{\Delta}(\sigma)$ is the linear function of stress tensor components [243, 108],

$$\Delta_{ijkl} = \frac{1}{2}(\delta_{ik}\sigma_{jl} + \delta_{jk}\sigma_{il} + \delta_{il}\sigma_{jk} + \delta_{jl}\sigma_{ik} - 2\delta_{kl}\sigma_{ij}).$$

In general, $\mathbf{B} = \mathbf{C} + \Delta(\sigma)$ will not have the symmetry of $\mathbf{C}$. If we adopt Voigt notation for $\mathbf{C}$, then the matrix $\mathbf{B}$ is

$$
\begin{bmatrix}
C_{11} + \sigma_{11} & C_{12} - \sigma_{11} & C_{13} - \sigma_{11} & C_{14} & C_{15} + \sigma_{13} & C_{16} + \sigma_{12} \\
C_{12} - \sigma_{22} & C_{22} + \sigma_{22} & C_{23} - \sigma_{22} & C_{24} + \sigma_{23} & C_{25} & C_{26} + \sigma_{12} \\
C_{13} - \sigma_{33} & C_{23} - \sigma_{33} & C_{33} + \sigma_{33} & C_{34} + \sigma_{23} & C_{35} + \sigma_{13} & C_{36} \\
C_{14} - \sigma_{23} & C_{24} & C_{34} & C_{44} + \dfrac{\sigma_{22} + \sigma_{33}}{2} & C_{45} + \dfrac{\sigma_{12}}{2} & C_{46} + \dfrac{\sigma_{13}}{2} \\
C_{15} & C_{25} - \sigma_{13} & C_{35} & C_{45} + \dfrac{\sigma_{12}}{2} & C_{55} + \dfrac{\sigma_{11} + \sigma_{33}}{2} & C_{56} + \dfrac{\sigma_{23}}{2} \\
C_{16} & C_{26} & C_{36} - \sigma_{12} & C_{46} + \dfrac{\sigma_{13}}{2} & C_{56} + \dfrac{\sigma_{23}}{2} & C_{66} + \dfrac{\sigma_{11} + \sigma_{22}}{2}
\end{bmatrix}
$$

Sometimes, to mimic $\mathbf{C}$, a symmetric matrix $\mathbf{A} = (\mathbf{B} + \mathbf{B}^{\mathrm{T}})/2$ is defined and then $\det|\mathbf{A}| > 0$ ensures mechanical stability. Under uniaxial strain and relaxation of the lattice perpendicular to the strained axis, only uniaxial stress (σ) remains in the lattice which will be added to write the modified elasticity matrix $\mathbf{B}$. For BCC lattice under tension along $< 100 >$, most of the components of $\mathbf{B}$ and $\mathbf{C}$ are same except $B_{12} = C_{12} - \sigma$, $B_{13} = C_{13} - \sigma$, $B_{55} = C_{55} + \sigma/2$, $B_{66} = C_{66} + \sigma/2$.

We apply the mechanical stability test on the uniaxially strained configurations to mark the actual theoretical strength of an alloy. In tensile test, the theoretical tensile strength corresponds to the peak engineering stress but the mechanical instability may arise earlier than that stress [244, 245, 246]. The theoretical strength of a material is the critical value of stress beyond which the mechanical instability arises. Even under uniaxial loading, a material may fail through a shear mode of deformation before reaching the peak tensile stress [106]. Then the corresponding pre-failure uniaxial stress is the *actual* tensile strength of that material. Following Schmid's law which refers to the projection of tensile strength along the slip direction, we can estimate the corresponding shear strength (τ_{crss}) too [107].

We identify shear instabilities in BCC HEAs under tension by applying mechanical stability analysis through (modified) Born's criteria, see Tables 5.4 and 5.5. We note that the extent of Nb-concentration in BCC $Nb_x(HfZrTi)_y$ determines the failure mode of their deformation. For equiatomic NbHfZrTi, the failure strain (where instability arises) is $\varepsilon_{11} = 14\%$. With the rise in Nb-concentration, the failure strain decreases (see Tables 5.4, 5.5, and 5.6) but the strength (pre-failure stress) enhances, see Figure 5.8. In other words, the increase of Nb-concentration

causes ductility loss but strengthens the resultant alloy. This is an open issue in materials science to simultaneously optimize both strength and ductility and known as *strength-ductility trade-off* [35, 36, 37, 38, 39]. Therefore, for the practical application, a single crystal of $Nb_{21}(HfZrTi)_5$ should be preferred over other configurations of $Nb_x(HfZrTi)_y$ (see Figure 5.8).
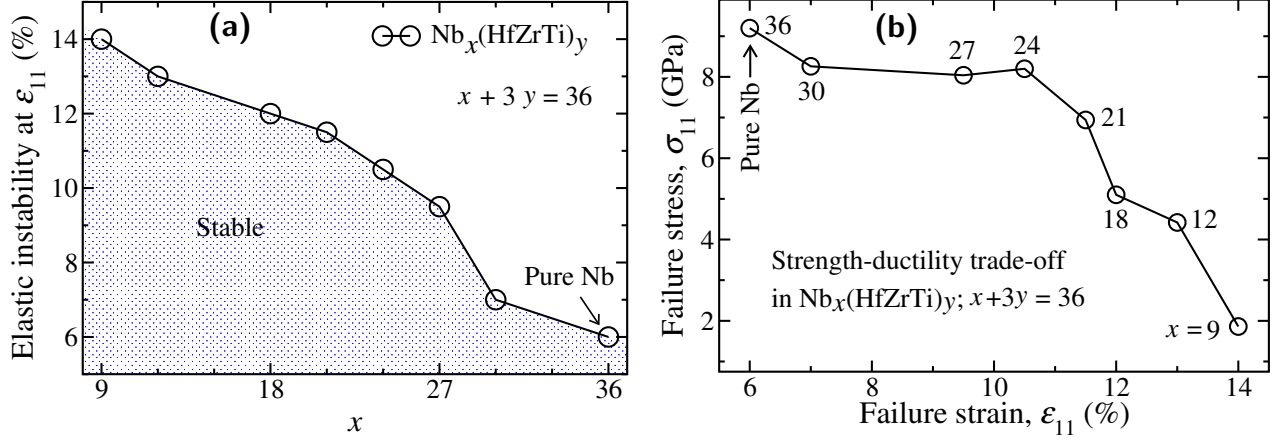
Figure 5.8:   (a) Elastic stability test of $Nb_x(HfZrTi)_y$ and (b) their strength-ductility trade-off. Born's criteria of elastic stability are the positive definiteness of each eigenvalue of the elastic constants matrix $\mathbf{C}$. (a) We show that the continuous increase of Nb-concentration in $Nb_x(HfZrTi)_y$ elastically destabilizes the resultant alloy at a lower strain (see also Table 5.4). (b) As seen in Figure 5.3, the failure stress corresponding to the (failure) strain where instability first arises improves with the rise in Nb-concentration but at the cost of losing ductility. This phenomenon so-called strength-ductility trade-off is observed in HEAs $Nb_x(HfZrTi)_y$ as a function of Nb-concentration. Therefore, for the practical application, a single-crystal of $Nb_{21}(HfZrTi)_5$ should be preferred among the other compositions of $Nb_x(HfZrTi)_y$ due to an optimal strength-ductility trade-off.

To determine the failure mode of a material, we evaluate the eigenvector corresponding to the first appeared negative eigenvalue of elastic constants matrix $\mathbf{C}$. The failure mode is evident by the eigenvector of $\mathbf{C}$ associated with a negative eigenvalue of $\mathbf{C}$ (see Table 5.6). We note from Table 5.6 that HEAs $Nb_x(HfZrTi)_y$ ($x + 3y = 36$) for $x = 9$ and 12 fail due to vanishing of tetragonal shear modulus, $C' = C_{11} - C_{12} < 0$, along $\{\eta_{xx}, \eta_{yy}, \eta_{zz}, 0, 0, 0\}$ where $\eta_{xx} + \eta_{yy} + \eta_{zz} = 0$. This is called Born's instability which is the case near melting where $C' \to 0$ faster than C_{44}. With further increment in Nb-concentration, the failure occurs through a mixed mode which combines normal strain and predominant shear strain. This is the case for $x = 15, 18$, and 21 where C' and C_{44} disappear together near the failure strain, see Table 5.6. While other compositions with higher Nb-concentrations ($x > 21$) fail through a pure shear instability as $C_{44} < 0$ along the eigenvector $\{0, 0, 0, \pm 1, 0, 0\}$. Instability arises at lower strains as the Nb-

concentration rises (see Figure 5.8) which also switches the failure mode of deformation from tetragonal shear to mixed to pure shear. This switching of the deformation pathway is in sync with the observation of a crossover from $C' < C_{44}$ to $C_{44} < C'$ at $x = 18$ with a continuous increase in Nb-concentration (x) (see Figure 5.1(b)).

5.3.5 Effect of CSRO on the mechanical behavior of HEAs

Short-range order (SRO) refers to the regular appearance of a particular arrangement of atoms (or molecules) in solids and liquids over distances comparable to interatomic (intermolecular) distances. The strength of pairwise interaction between atoms dictates the kind of range order, either short or long, within a given material. In case of solids, at one extreme, a very strong interaction energy between specific pairs of atoms tends to form a fixed stochiometry ordered-structure compound or intermetallic compound. On the other extreme, the vanishing limit of interaction strength between each pair of constituent atoms produces an ideal solid solution.

In the Table A4.4 of Chapter 4, we have estimated the formation energies of several alloys. We note that binary alloys Mo_pW_q are ideal as their formation energies (H_f) vanishes, and HEAs $Nb_x(HfZrTi)_y$ are enthalpically unstable as their $H_f > 0$. In contrast, the HEAs $Nb_aMo_bW_cTa_d$ are enthalpically stable with $H_f < 0$. When the electronegativity differences among the elements being mixed are large, a large negative value of H_f is seen suggesting that strong preferential bonds within a material gives rise to short-range ordering. This should give rise to a stronger *chemical* short-range order (CSRO) in NbMoWTa ($H_f < 0$) and weaker in NbHfZrTi ($H_f > 0$).

Chemical short range ordering (CSRO) is not uncommon in high-entropy alloys (HEAs) [189]. S. D. Wang et al. [247] have given a detailed account of CSRO in refractory HEAs and its impact on their strength. Here, we reveal the CSRO in BCC NbMoWTa and NbHfZrTi based on the SwapMC simulation method. The steps involved in this setup are as follows

1. We start from a special quasirandom configuration (by construction, the SQS configuration should have the least CSRO).

2. In the MC loop, we pick two distinct atoms at random and swap their positions.

3. Now relax the lattice to get the energy.

4. If the lattice energy drops then allow the swapping to update the configuration else go to

step 2.

5. We keep swapping atoms until the energy saturates and the configuration converges to the right local chemical environment.
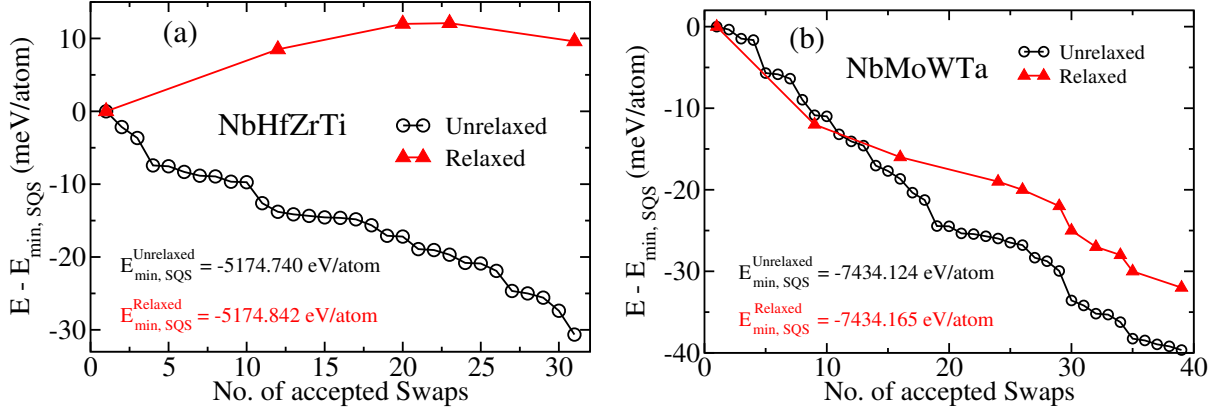
Figure 5.9: (a) SwapMC simulation of NbHfZrTi with frozen ionic sites (unrelaxed and unrealistic) sequentially lowers the energy but on full relaxation of the corresponding configuration which takes ILDs into account increases the energy than that of SQS configuration. This finding highlights the significance of ILDs on the lattice energy of HEAs in addition to the right internal chemical environment. In contrary to NbHfZrTi, a relatively weaker ILDs in NbMoWTa allowed us to run SwapMC on a fixed lattice structure with only chemical tuning at each MC step. Rise in energy than that of SQS configuration with swap of constituent elements demonstrates HEA NbHfZrTi to be close to an ideal solid solution. An *ab initio* simulation [201] reveals weak chemical ineraction within NbHfZrTi and confirms its robustness to maintain single-phase solid solutions at various temperatures and pressures [202]. But DFT-based MC simulation by Zhang et al. [248] discover CSRO in this alloy as Nb-Hf and Zr-Ti favored to be nearest-neighbor pairs. (b) SwapMC simulation of NbMoWTa with frozen ionic sites lowers the energy and the same trend is seen on the full relaxation of the corresponding configuration too.

We should note that the last configuration fetched by SwapMC will depend on the considered supercell size, but the chemical ordering will be qualitatively the same even for a modest size supercell we have chosen.

In Figure 5.10(a), we demonstrate an increase of CSRO in NbMoWTa with each SwapMC step. More precisely, the shares of Mo-Ta, Nb-W, Nb-Mo, and W-Ta bonds grow while the share of Ta-Ta and Mo-Mo bonds diminishes with the progress of the SwapMC loop which began from an SQS configuration. Increased CSRO brings lattice stability as we note a 40 meV/atom energy drop from the initial SQS configuration. In the case of BCC NbHfZrTi, we noted a energy variation of only 20 meV/atom among 50 sets of SQS configurations (see Figure 4.3(b)) which indicates the presence of a weak CSRO. Monte Carlo simulations of Zhang

et al. [248] reveal CSRO in NbHfZrTi with Nb-Hf and Zr-Ti favored to be nearest-neighbor atomic pairs. Later, the research of Ryltsev et al. [201], based on AIMD simulations reveal weak chemical interactions within NbHfZrTi which tends this alloy to form single-phase solid solutions at varied temperatures and pressures [202]. Therefore, BCC NbHfZrTi is close to being an ideal solid solution, consistent with that our SwapMC simulation did not reveal any conclusive evidence of ordering in this alloy (see Figure 5.9(a)). On the other hand, NbMoWTa comprising elements with large electronegativity differences (see Table 5.2) shows strong CSRO since enegy decreases and preferential bonds grow with each MC step (see Figures 5.9(b) and 5.10(a)). The observed CSRO in NbMoWTa is consistent with the reported negative cohesive energy profiles of a few binay refractory alloys (see Figure 2 of ref. [249]).

Table 5.2: Pauling electronegativities (χ) of a few refractory elements.

Element	Nb	Hf	Zr	Ti	Mo	W	Ta
χ	1.60	1.30	1.33	1.54	2.16	2.36	1.50
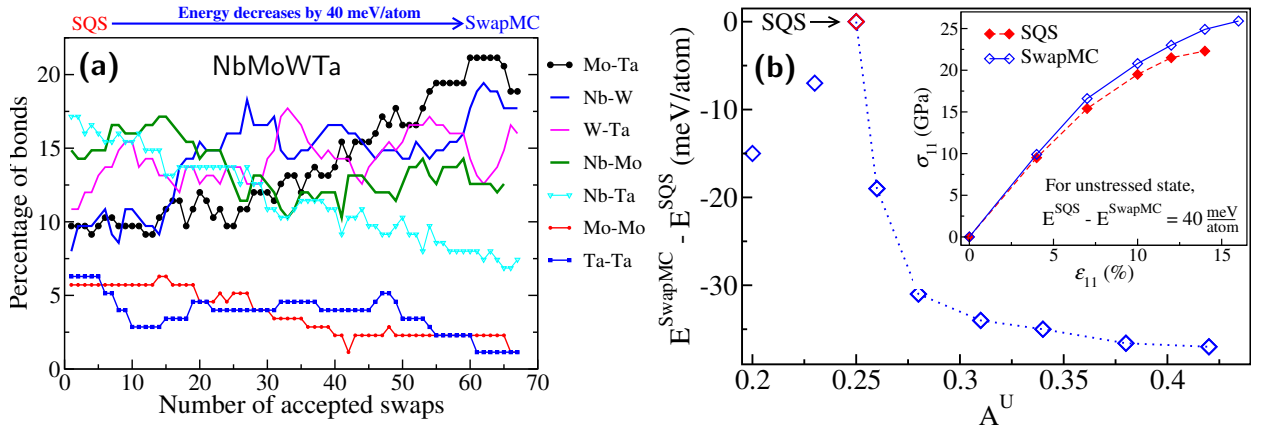
Figure 5.10: Swap Monte-Carlo study to reveal (a) chemical short-range order (CSRO) in HEA NbMoWTa and (b) their impact on the elastic anisotropy and tensile behavior. By construction, the special quasirandom structures (SQS) have low CSRO and hence physically meaningful only at high temperatures. SwapMC gives ultrastable configurations of HEAs by converging to the right local chemical order through multiple swaps of atomic sites. (a) In NbMoWTa, CSRO is marked by increased Mo-Ta, Nb-W, Nb-Mo, and W-Ta preferential bondings while avoiding Ta-Ta and Mo-Mo pairs. (b) An increased degree of CSRO magnifies elastic anisotropy (A^U) and strengthens NbMoWTa (see inset).

It is well known that the properties especially the mechanical properties of an annealed (slow-cooled) sample and a quenched (fast-cooled) sample of a given material differ significantly. This thermal effect is widely used in the steel industry and has keywords such as 'hot working and

cold working'. Such heat treatment processes control (promote) the dynamics of dislocation to enhance (soften) the strength. It is reported that an increased degree of CSRO in HEAs promotes strengthening effect [247, 189, 39, 250]. We also observe an enhanced strength and ductility in the single-crystal NbMoWTa (see inset of Figure 5.10(b)). The SQS configuration of NbMoWTa could not have been stretched beyond 14% in computation, but the end configuration obtained by SwapMC setup (which is lower in energy by 40 meV/atom) was easily stretched by 16% (see inset of Figure 5.10(b)). It shows the improvement of ductility and strength with an increasing degree of CSRO. At the same time, the elastic anisotropy also enhances with an increase in CSRO. Figure 5.10(b) shows that the elastic anisotropy index A^U of NbMoWTa increases from 0.25 to 0.42 as we go from an SQS configuration to the end SwapMC configuration.

5.4   Conclusions

In summary, we studied the impact of Nb-concentration on the mechanical behavior of HEAs $Nb_x(HfZrTi)_y$ using first-principles calculations. We show that a continuous rise in Nb-concentration causes anomalous variation in elastic anisotropy and switches the failure mode from tetragonal shear to mixed to pure shear. We find a strength-ductility trade-off in single-crystals of $Nb_x(HfZrTi)_y$ as a function of Nb-concentration. Based on this, we recommend using single-crystal $Nb_{21}(HfZrTi)_5$ for the practical applications. We apply mechanical stability analysis to estimate the actual tensile strengths and failure mechanisms of these HEAs and others. We trace a BCC to FCC Bain transformation path in the plane of bond-orientational order parameters $(\bar{q}_8, \bar{q}_{12})$ which looks like a C-curve for an ideal lattice. Intrinsic ILDs and the emergence of Voronoi pentagons within strained configurations of BCC HEAs cause deviation from the ideal Bain path. In the end, we discuss the impact of chemical short-range order (CSRO) on the mechanical behavior of BCC NbMoWTa high-entropy alloy.

Table 5.3: Elastic properties data: We list below Young's modulus (E), bulk modulus (B), and shear modulus (G), Poisson's ratio (ν), Debye sound speed (c_s), universal elastic anisotropy index (A^U), and inverse of Pugh ratio (B/G) of Nb-Hf-Zr-Ti, Nb-Mo-W-Ta, and Mo-W alloys of different compositions. Interestingly, Nb-concentration dictates the elastic properties of $\text{Nb}_x(\text{HfZrTi})_y$ as increase in x raises the bulk modulus (B), Poisson's ratio (ν) and ductility (B/G), and brings anomalous variation in anisotropy (A^U) (see Figure 5.1). On the contrary, varying composition does not display such a significant trend in Nb-Mo-W-Ta, and Mo-W alloys.

BCC alloys	E (GPa)	B (GPa)	G (GPa)	ν	c_s (km/s)	A^U	B/G
HCP $(\text{HfZrTi})_{12}$	125	103	48.2	0.297	2.68	0.05	2.13
HCP $\text{Nb}_3(\text{HfZrTi})_{11}$	93	106	34.3	0.353	2.20	0.20	3.08
$\text{Nb}_6(\text{HfZrTi})_{10}$	85	107	31.0	0.368	2.15	0.43	3.46
$(\text{NbHfZrTi})_9$	89	109	32.6	0.364	2.20	0.29	3.36
$\text{Nb}_{12}(\text{HfZrTi})_8$	93	115	34.0	0.366	2.25	0.19	3.40
$\text{Nb}_{15}(\text{HfZrTi})_7$	90	121	32.5	0.376	2.20	0.08	3.72
$\text{Nb}_{18}(\text{HfZrTi})_6$	84	124	30.3	0.387	2.13	0.10	4.10
$\text{Nb}_{21}(\text{HfZrTi})_5$	89	132	32.0	0.388	2.18	0.08	4.14
$\text{Nb}_{24}(\text{HfZrTi})_4$	89	139	32.0	0.393	2.17	0.43	4.34
$\text{Nb}_{27}(\text{HfZrTi})_3$	74	147	26.0	0.415	1.98	1.10	5.65
$\text{Nb}_{30}(\text{HfZrTi})_2$	75	156	26.4	0.420	1.96	1.48	5.91
$\text{Nb}_{33}(\text{HfZrTi})_1$	83	166	29.3	0.415	2.05	1.70	5.66
Nb_{36}	90	176	31.7	0.413	2.11	1.93	5.56
Unit cell of Nb_2	69	168	24.0	0.430	1.86	1.75	7.02
$(\text{NbMoWTa})_9$	210	232	78.0	0.349	2.68	0.25	2.97
$(\text{NbMoWTa})_{10}\text{Ta}_6$	237	236	88.8	0.332	2.88	0.32	2.65
$(\text{NbWTa})_8\text{Mo}_{12}$	229	235	85.7	0.337	2.84	0.28	2.74
$\text{Nb}_8\text{Mo}_{11}\text{W}_{12}\text{Ta}_8$	271	246	103.0	0.316	3.06	0.20	2.38
$\text{Nb}_{10}\text{Mo}_{13}\text{W}_7\text{Ta}_6$	243	233	91.6	0.326	3.01	0.27	2.54
$\text{Nb}_{12}\text{Mo}_8\text{W}_9\text{Ta}_7$	201	226	74.5	0.351	2.67	0.32	3.02
Mo_4W_{32}	347	297	133.0	0.305	3.03	0.003	2.23
$\text{Mo}_{10}\text{W}_{26}$	346	294	132.6	0.304	3.16	0.05	2.22
$\text{Mo}_{18}\text{W}_{18}$	322	282	123.0	0.310	3.23	0.15	2.29
$\text{Mo}_{24}\text{W}_{12}$	311	276	118.7	0.310	3.35	0.18	2.32

Table 5.4: **Born's elastic stability test of uniaxially strained $Nb_x(HfZrTi)_y$ where $x + 3y = 36$ and others:** Born's criteria state that a specimen of material is elastically stable if each eigenvalue $(e_1, e_2, \cdots, e_6)$ of its elastic matrix ($\mathbf{C}$) is positive [15]. We compute the eigenvalues of $\mathbf{C}$ at stress-free, pre-failure, and failure strain configurations of several alloys. We note that alloys $Nb_x(HfZrTi)_y$ become unstable (as $e_1 < 0$) at lower strains with increasing Nb-concentration. For instance, $3 \times 3 \times 2$-size supercell of Nb becomes elastically unstable only at $\varepsilon_{11} = 6\%$ while $(NbHfZrTi)_9$ high-entropy alloy becomes unstable at $\varepsilon_{11} = 14\%$. Equiatomic HEAs exhibit superior ductility over an elemental metal as they fail at $\varepsilon_{11} = 14\%$.

BCC alloys	ε_{11} (%)	e_1	e_2	e_3	e_4	e_5	e_6
	0	37	39	42	45	53	328
$(NbHfZrTi)_9$	12	3.7	15	35	49	42	313
	14	**-5.1**	20	35	37	40	320
	0	36	37	43	49	65	346
$Nb_{12}(HfZrTi)_8$	12	5.6	12	31	33	38	322
	13	**-4.2**	9.2	32	33	38	326
	0	31	37	38	57	59	363
$Nb_{15}(HfZrTi)_7$	16	0.1	0.8	32	38	49	345
	16.5	**-9.1**	**-1.1**	32	37	43	345
	0	25	28	31	61	76	373
$Nb_{18}(HfZrTi)_6$	10	3.6	6.4	25	31	33	359
	12	**-1.4**	0.1	27	28	39	360
	0	27	30	34	66	75	398
$Nb_{21}(HfZrTi)_5$	11	1.9	7.7	24	27	33	370
	11.5	**-7.4**	5.5	23	26	31	368
	0	20	29	31	78	94	416
$Nb_{24}(HfZrTi)_4$	10	0.2	21	26	31	45	390
	10.5	**-1.6**	19	24	28	42	391
	0	13	21	23	78	92	441
$Nb_{27}(HfZrTi)_3$	9	0.1	21	24	44	62	412
	9.5	**-1.8**	21	24	40	58	411
	0	13	18	22	94	96	470
$Nb_{30}(HfZrTi)_2$	6	2.1	21	28	78	88	447
	7	**-1.9**	22	27	78	85	442
	0	15	15	15	93	93	506
Nb_{36}	5	4.1	12	30	68	118	502
	6	**-4.9**	11	23	63	98	497
	0	36	37	40	92	104	482
$(NbVTaTi)_9$	12	5.8	20	34	36	59	450
	14	**-3.0**	2.6	32	38	55	445
	0	62	66	68	183	222	695
$(NbMoWTa)_9$	13	24	25	37	42	218	600
	14	**-40**	16	21	36	209	597
	0	98	118	118	247	331	845
$(MoW)_{18}$	12	0.3	58	67	67	270	736
	13	**-15**	52	56	60	257	726

Table 5.5: **Modified Born's elastic stability test of a uniaxially strained specimen:** A material under finite strain is elastically stable if each eigenvalue ($e_1, e_2, \cdots, e_6$) of its modified elastic matrix ($\mathbf{A} = (\mathbf{B} + \mathbf{B}^T)/2$ where $\mathbf{B} = \mathbf{C} + \Delta(\sigma)$) be positive [243, 108]. For tensile stress $\sigma_{11} = \sigma$, most of the components of $\mathbf{B}$ and $\mathbf{C}$ are same except $B_{11} = C_{11} + \sigma$, $B_{12} = C_{12} - \sigma$, $B_{13} = C_{13} - \sigma$, $B_{55} = C_{55} + \sigma/2$, and $B_{66} = C_{66} + \sigma/2$. We note that the modified stability criteria fail to identify a few unstable configurations (gray colored rows) which instabilities also marked by negative elastic moduli (C', C_{44}, E, G are in GPa) were successfully detected by Born's criteria (Table 5.4).

BCC alloys	ε_{11} (%)	e_1	e_2	e_3	e_4	e_5	e_6	C'	C_{44}	E	G
(NbHfZrTi)$_9$	0	37	39	42	45	53	328	26	37	89	32.6
	12	8.0	15	36	43	44	311	5.2	15	43	15.2
	14	**-2.8**	20	36	38	41	319	-0.04	20	-3.0	0.4
Nb$_{12}$(HfZrTi)$_8$	0	36	37	43	49	65	346	31	41	93	34
	12	11	13	32	34	40	320	1.4	12	41	14.4
	13	1.7	9.2	33	34	40	325	-5	9.2	-5.1	-0.64
Nb$_{15}$(HfZrTi)$_7$	0	31	37	38	57	59	363	29	37	90	32.5
	14	5.9	11	35	41	49	339	2.2	7.0	38	14.0
	16	0.3	6.8	34	40	46	343	0.8	0.3	27	9.5
Nb$_{18}$(HfZrTi)$_6$	0	25	28	31	61	76	373	32	27	84	30.3
	10	5.2	11	28	32	34	357	-0.14	6.1	33	11.3
	12	**-1.1**	6.1	29	31	40	358	-0.5	-1.0	22	7.5
Nb$_{21}$(HfZrTi)$_5$	0	27	30	34	66	75	398	38	31	89	32
	11	5.9	12	27	31	34	367	-2.4	6.8	28	9.65
	11.5	0.6	6.3	25	29	33	366	-5.6	5.2	103	39
Nb$_{24}$(HfZrTi)$_4$	0	20	28	31	78	94	416	39	27	89	32
	10	0.3	24	31	39	47	387	8.0	0.7	27	9.3
	10.5	**-1.5**	23	30	36	44	388	6	-1.0	4.4	2.0
Nb$_{27}$(HfZrTi)$_3$	0	13	21	23	78	92	441	41	18	74	26
	9	0.2	25	29	51	66	409	13	0.6	30	10.4
	9.5	**-1.7**	26	28	49	58	411	10	-1	7.2	3
Nb$_{30}$(HfZrTi)$_2$	0	13	18	22	94	96	470	49	15	75	26.3
	6	2.1	25	31	79	98	444	38	2.2	50	17.6
	7	**-1.9**	26	31	79	95	439	35	-1.8	17	6.6
Nb$_{36}$	0	15	15	15	93	93	506	50	19	90	31.7
	5	4.1	16	34	72	125	499	32	4.1	58	20
	6	**-4.9**	16	27	68	106	493	26	-5.0	-690	-109
	14	**-38**	12	21	32	110	459	20	-38	7.0	2.4
(NbVTaTi)$_9$	0	36	37	40	92	104	482	45	40	116	42
	12	5.9	31	39	41	59	446	-1.0	6.0	53	18.6
	14	**-3.0**	15	36	42	56	442	-9.0	-3.0	42	14.5
(NbMoWTa)$_9$	0	62	66	68	183	222	695	110	68	210	78
	13	24	37	52	71	218	592	-8	24	104	37
	14	**-8.9**	17	33	48	210	589	-54	16	120	42
(MoW)$_{18}$	0	98	118	118	247	331	845	165	118	322	123
	13	23	52	70	73	257	716	-29	52	-32	-6
	14	**-8.3**	50	58	59	232	724	-49	50	278	109

Table 5.6: **Eigenmode of failure deformation in Nb$_x$(HfZrTi)$_y$ where $x + 3y = 36$ and others:** The eigenvector corresponding to the negative eigenvalue of elastic constants matrix **C** determines the failure mode of a material. In a material with cubic symmetry, the eigenmode of deformation for vanishing tetragonal shear modulus (i.e. $C' = (C_{11} - C_{12})/2 < 0$) is $(\delta\eta_{xx}, \delta\eta_{yy}, \delta\eta_{zz}, 0, 0, 0)$ and the eigenmode of deformation for pure shear failure ($C_{44} < 0$) is $(0, 0, 0, \delta\eta_{yz}, 0, 0)$. Therefore, we see in the table below that a continuous rise in Nb-concentration in Nb$_x$(HfZrTi)$_y$ changes the failure mode from tetragonal shear to mixed to pure shear. This variation in failure mode is consistent with the observation made in Figure 5.1(b) where we noted a crossover between C' and C_{44} as a function of Nb-concentration.

BCC alloys	ε_{11} (%)	e_1	C'	C_{44}	η_{xx}	η_{yy}	η_{zz}	η_{yz}	η_{zx}	η_{xy}	Failure mode
Nb$_6$(HfZrTi)$_{10}$	16	**-4.9**	3.5	19	0.77	-0.10	-0.63	0	0	0	Tetragonal shear
(NbHfZrTi)$_9$	14	**-5.1**	-0.04	20	-0.80	0.18	0.57	0	0	0	Tetragonal shear
Nb$_{12}$(HfZrTi)$_8$	13	**-4.2**	-5	9	-0.83	0.37	0.40	0	0	0	Tetragonal shear
Nb$_{15}$(HfZrTi)$_7$	16.5	**-9.1**	-1.4	-1.7	0.24	0	-0.15	-0.95	0	0	Mixed
Nb$_{18}$(HfZrTi)$_6$	12	**-1.4**	-0.5	-1	-0.4	0	0.3	0.9	0	0	Mixed
Nb$_{21}$(HfZrTi)$_5$	11.5	**-7.4**	-5.5	5	0.8	-0.2	-0.5	0.2	0	0	Mixed
Nb$_{24}$(HfZrTi)$_4$	10.5	**-1.6**	6	-1	0	0	0	-1	0	0	Shear
Nb$_{27}$(HfZrTi)$_3$	9.5	**-1.8**	10	-1	0	0	0	1	0	0	Shear
Nb$_{30}$(HfZrTi)$_2$	7	**-1.9**	35	-2	0	0	0	1	0	0	Shear
Nb$_{36}$	6	**-4.9**	26	-5	0	0	0	1	0	0	Shear
(NbVTaTi)$_9$	14	**-3.0**	-9	-3	0	0	0	-1	0	0	Shear
(NbMoWTa)$_9$	14	**-40**	-54	16	-0.9	0.4	0.2	0	0	0	Tetragonal shear
(MoW)$_{18}$	13	**-15**	-29	52	-0.8	0.4	0.3	0	0	0	Tetragonal shear

Chapter 6

Summary & Future Outlook

Summary

In this thesis, we employed machine-learning and first-principles modelling to understand complex phenomena involving processes at multiple scales in materials science. Dielectric breakdown in solids, proton conduction in cubic perovskite oxides, and structural stability & mechanical behavior of high-entropy alloys are the topics I have worked on during my Ph.D. tenure. These phenomena are complex as they lack microscopic theories. We rely on phenomenological or mean field theories to understand dielectric breakdown, phase transition, proton conduction and mechanical failure in materials. The complexity arises due to their highly nonlinear behavior and spanning multiple scales. The complexity and multiscale nature of the studied phenomena is the linking thread of this thesis.

In Chapter 2, we presented an integrated framework of machine learning (ML), scaling laws, and dimensional analysis to get a simple interpretable model and illustrated it in the analysis of dielectric breakdown in solids. Our model needs two material descriptors bandgap (E_g) and nearest-neighbor distance (d_{nn}) which are easily accessible. The predictive ability of our model, particularly for new materials (which are distinct from those used in ML training) is superior to the other existing models of the dielectric breakdown field. In Chapter 3, we aimed at an ML model of proton conductivity in perovskite oxides which could later be used to discover a better proton conductor for an electrolyte within fuel cell application. We have listed out the descriptors relevant to proton conduction in cubic ABO_3 perovskite oxides. We estimated

energy barriers for proton transfer in a few perovskite oxides too, which can be modeled with the proposed ML framework.

In Chapters 4 and 5, we studied multi-elemental metallic alloys. An equiatomic configuration of such an alloy called high-entropy alloy (HEA) has high configurational entropy due to inherent chemical substitutional disorder. Despite the mixture of multiple (≥ 4) elements, the lattice structures of most of the HEAs are still BCC, FCC, or HCP. In Chapter 4, we reported an HCP$\rightarrow$BCC phase transition in $Nb_x(HfZrTi)_{36-x}$ at $x = 6$ composition with increasing Nb-concentration (x). Local structure was analyzed through the construction of Voronoi cells and bond-orientational order parameters to mark the structural transformation. Internal lattice distortions peak at the transition and can be regarded as an indicator of the first-order transition. We also demonstrated that alloys in this family are enthalpically unfavorable, and the entropy stabilizes them.

In the final work Chapter (5), we computed the mechanical properties of BCC-structured high-entropy alloys. We noted an anomalous variation in elastic anisotropy as a function of Nb-concentration in $Nb_x(HfZrTi)_{36-x}$. Bulk Nb is elastically anomalous due to soft C_{44} which causes a large anisotropy ($A_Z = C'/C_{44}$). The anomalous variation in anisotropy with x is first controlled by the HCP$\rightarrow$BCC transition and then by the effects of Nb. Next, we estimated the ideal tensile strength of $Nb_x(HfZrTi)_{36-x}$ by uniaxially deforming the lattice along the $< 100 >$ direction. Mechanical stability analysis revealed that the failure mode switches from tetragonal shear to mixed to pure shear with increasing Nb-concentration. The alloys in this family exhibit a strength-ductility trade-off as a function of Nb-concentration (x). We also simulated a few binary alloys and other quaternary HEAs to juxtapose the results with those obtained for $Nb_xHfZrTi_{36-x}$.

Future outlook

In Chapter 2, we presented a *simple* and *interpretable* ML model from a *small* dataset of dielectric breakdown – a multi-scale process. Dimensional analysis and existing scaling laws made the model physically interpretable. This kind of ML model development is generic in nature and can be applied to predict other material properties too, for example, proton conductivity in fuel cells (ongoing work in Chapter 3).

Prediction of *mechanical failure* is given high importance in structural engineering applications. A computational guideline for the synthesis of high-strength materials is the core of part II of my thesis. I am sure that my thesis will help other researchers in the materials science community to check the structural stability and mechanical behavior of high-entropy alloys. We have used a robust set of descriptors for local structural analysis to infer the phase transformation in internally distorted lattices of HEAs. These descriptors can be used in identifying the local crystalline phases within any distorted structures. For example, the presence of multiphases within HEAs (in accordance with Gibbs phase rule) can be detected using our proposed set of descriptors.

We simulated single-crystalline bulk phases of HEAs using DFT at 0 K. To study the effect of temperature, system size, and crystallographic defects on the mechanical strength of an HEA, one should run *ab-initio* or *molecular* dynamics simulations (MD). AIMD is accurate but computationally expensive and limited to system-size having a few thousands of atoms. On the other hand, classical potentials used in MD are inaccurate and empirical in nature. Therefore, one can learn DFT-based interatomic potential energy through machine learning. Such ML trained interatomic potential (MLIP) is accurate and fast for MD simulations and often used to study the properties of systems at a large scale. Finite element method is an another way to look at the mechanical behavior of HEAs at microscale.

There are many open questions in high-entropy alloys. I am listing a few of them which we are currently studying.

1. Single-phase HEAs are limited. How to predict the composition of a single-phase HEA? This question is also rephrased as the structural stability of HEAs.

2. What is the origin of ILDs in HEAs and how does ILDs affect their mechanical strength? We answered it to some extent in Chapters 4 and 5 but a complete understanding is missing.

3. What are the mechanical failure mechanisms of HEAs? We noted a switching of failure mechanism from *Born's* instability to *shear* instability in $Nb_xHfZrTi$ with increasing Nb-content. What causes this switching is not yet understood.

Bibliography

[1] Paul Adrien Maurice Dirac and Ralph Howard Fowler. Quantum mechanics of many-electron systems. *Proceedings of the Royal Society of London. Series A, Containing Papers of a Mathematical and Physical Character*, 123(792):714–733, 1929.

[2] Walter Kohn, Axel D Becke, and Robert G Parr. Density functional theory of electronic structure. *The journal of physical chemistry*, 100(31):12974–12980, 1996.

[3] Richard M Martin. *Electronic structure: basic theory and practical methods*. Cambridge university press, 2020.

[4] Gang Zhang and Charles B Musgrave. Comparison of DFT methods for molecular orbital eigenvalue calculations. *The journal of physical chemistry A*, 111(8):1554–1561, 2007.

[5] Kurt Lejaeghere, Veronique Van Speybroeck, Guido Van Oost, and Stefaan Cottenier. Error estimates for solid-state density-functional theory predictions: an overview by means of the ground-state elemental crystals. *Critical reviews in solid state and materials sciences*, 39(1):1–24, 2014.

[6] Feliciano Giustino. *Materials modelling using density functional theory: properties and predictions*. Oxford University Press, 2014.

[7] Igor S. Aranson and Lorenz Kramer. The world of the complex Ginzburg-Landau equation. *Rev. Mod. Phys.*, 74:99–143, Feb 2002.

[8] P.C. Hohenberg and A.P. Krekhov. An introduction to the Ginzburg-Landau theory of phase transitions and nonequilibrium patterns. *Physics Reports*, 572:1–42, 2015. An introduction to the Ginzburg-Landau theory of phase transitions and nonequilibrium patterns.

[9] Pawan Kumar and Umesh V. Waghmare. First-principles phonon-based model and theory of martensitic phase transformation in niti shape memory alloy. *Materialia*, 9:100602, 2020.

[10] Herbert Fröhlich. Theory of electrical breakdown in ionic crystals. *Proceedings of the Royal Society of London. Series A-Mathematical and Physical Sciences*, 160(901):230–241, 1937.

[11] Artur Von Hippel. Electric breakdown of solid and liquid insulators. *Journal of Applied Physics*, 8(12):815–832, 1937.

[12] Y Sun, SA Boggs, and R Ramprasad. The intrinsic electrical breakdown strength of insulators from first principles. *Applied Physics Letters*, 101(13), 2012.

[13] Noam Agmon. The grotthuss mechanism. *Chemical Physics Letters*, 244(5):456–462, 1995.

[14] Alan Arnold Griffith. Vi. the phenomena of rupture and flow in solids. *Philosophical transactions of the royal society of london. Series A, containing papers of a mathematical or physical character*, 221(582-593):163–198, 1921.

[15] Max Born. Thermodynamics of Crystals and Melting. *The Journal of Chemical Physics*, 7(8):591–603, 12 2004.

[16] Jack A Collins. *Failure of materials in mechanical design: analysis, prediction, prevention*. John Wiley & Sons, 1993.

[17] Shigenobu Ogata, Ju Li, and Sidney Yip. Ideal pure shear strength of aluminum and copper. *Science*, 298(5594):807–811, 2002.

[18] Seung-Hoon Jhi, Jisoon Ihm, Steven G Louie, and Marvin L Cohen. Electronic mechanism of hardness enhancement in transition-metal carbonitrides. *Nature*, 399(6732):132–134, 1999.

[19] R.J. Asaro and J.R. Rice. Strain localization in ductile single crystals. *Journal of the Mechanics and Physics of Solids*, 25(5):309–338, 1977.

[20] Ting Zhu and Ju Li. Ultra-strength materials. *Progress in Materials Science*, 55(7):710–757, 2010.

[21] Easo P George, Dierk Raabe, and Robert O Ritchie. High-entropy alloys. *Nature reviews materials*, 4(8):515–534, 2019.

[22] Indranil Basu and Jeff Th M De Hosson. Strengthening mechanisms in high entropy alloys: fundamental issues. *Scripta Materialia*, 187:148–156, 2020.

[23] Yuntian T Zhu and Xiaozhou Liao. Retaining ductility. *Nature materials*, 3(6):351–352, 2004.

[24] Robert O Ritchie. The conflicts between strength and toughness. *Nature materials*, 10(11):817–822, 2011.

[25] J.-W. Yeh, S.-K. Chen, S.-J. Lin, J.-Y. Gan, T.-S. Chin, T.-T. Shun, C.-H. Tsau, and S.-Y. Chang. Nanostructured high-entropy alloys with multiple principal elements: Novel alloy design concepts and outcomes. *Adv. Eng. Mater.*, 6(5):299–303, 2004.

[26] B. Cantor, I.T.H. Chang, P. Knight, and A.J.B. Vincent. Microstructural development in equiatomic multicomponent alloys. *Mater. Sci. Eng. A*, 375-377:213–218, 2004.

[27] Zhiming Li, Konda Gokuldoss Pradeep, Yun Deng, Dierk Raabe, and Cemal Cem Tasan. Metastable high-entropy dual-phase alloys overcome the strength–ductility trade-off. *Nature*, 534(7606):227–230, 2016.

[28] Bernd Gludovatz, Anton Hohenwarter, Dhiraj Catoor, Edwin H. Chang, Easo P. George, and Robert O. Ritchie. A fracture-resistant high-entropy alloy for cryogenic applications. *Science*, 345(6201):1153–1158, 2014.

[29] S. Gorsse, M.H. Nguyen, O.N. Senkov, and D.B. Miracle. Database on the mechanical properties of high entropy alloys and complex concentrated alloys. *Data in Brief*, 21:2664–2678, 2018.

[30] Easo P George, Dierk Raabe, and Robert O Ritchie. High-entropy alloys. *Nat. Rev. Mater.*, 4(8):515–534, 2019.

[31] E.P. George, W.A. Curtin, and C.C. Tasan. High entropy alloys: A focused review of mechanical properties and deformation mechanisms. *Acta Materialia*, 188:435–474, 2020.

[32] Zezhou Li, Shiteng Zhao, Robert O. Ritchie, and Marc A. Meyers. Mechanical properties of high-entropy alloys with emphasis on face-centered cubic alloys. *Progress in Materials Science*, 102:296–345, 2019.

[33] Weidong Li, Di Xie, Dongyue Li, Yong Zhang, Yanfei Gao, and Peter K. Liaw. Mechanical behavior of high-entropy alloys. *Progress in Materials Science*, 118:100777, 2021.

[34] Dong Liu, Qin Yu, Saurabh Kabra, Ming Jiang, Paul Forna-Kreutzer, Ruopeng Zhang, Madelyn Payne, Flynn Walsh, Bernd Gludovatz, Mark Asta, et al. Exceptional fracture toughness of CrCoNi-based medium-and high-entropy alloys at 20 kelvin. *Science*, 378(6623):978–983, 2022.

[35] Zhifeng Lei, Xiongjun Liu, Yuan Wu, Hui Wang, Suihe Jiang, Shudao Wang, Xidong Hui, Yidong Wu, Baptiste Gault, Paraskevas Kontis, et al. Enhanced strength and ductility in a high-entropy alloy via ordered oxygen complexes. *Nature*, 563(7732):546–550, 2018.

[36] Yu Zou, Huan Ma, and Ralph Spolenak. Ultrastrong ductile and stable high-entropy alloys at small scales. *Nature communications*, 6(1):7748, 2015.

[37] TW Zhang, SG Ma, D Zhao, YC Wu, Y Zhang, ZH Wang, and JW Qiao. Simultaneous enhancement of strength and ductility in a NiCoCrFe high-entropy alloy upon dynamic tension: Micromechanism and constitutive modeling. *International Journal of Plasticity*, 124:226–246, 2020.

[38] Yeqiang Bu, Yuan Wu, Zhifeng Lei, Xiaoyuan Yuan, Honghui Wu, Xiaobin Feng, Jiabin Liu, Jun Ding, Yang Lu, Hongtao Wang, Zhaoping Lu, and Wei Yang. Local chemical fluctuation mediated ductility in body-centered-cubic high-entropy alloys. *Materials Today*, 46:28–34, 2021.

[39] Ruixin Wang, Dabo Duan, Yu Tang, Zhifeng Lei, Shun Li, Rong Chen, Chao Ma, Yuan Wu, Shuxin Bai, and Zhaoping Lu. Evading dynamic strength and ductility trade-off in

a high-entropy alloy via local chemical ordering. *Communications Materials*, 4(1):25, 2023.

[40] Y. F. Ye, Q. Wang, J. Lu, C. T. Liu, and Y. Yang. High-entropy alloy: challenges and prospects. *Mater. Today*, 19(6):349–362, 2016.

[41] WA Curtin, SI Rao, and C Woodward. Progress and challenges in the theory and modeling of complex concentrated alloys. *Mrs Bulletin*, 47(2):151–157, 2022.

[42] E. J. Pickering and N. G. Jones. High-entropy alloys: a critical assessment of their founding principles and future prospects. *Int. Mater. Rev.*, 61(3):183–202, 2016.

[43] D.B. Miracle and O.N. Senkov. A critical review of high entropy alloys and related concepts. *Acta Mater.*, 122:448–511, 2017.

[44] Muhammad Naeem, Haiyan He, Fan Zhang, Hailong Huang, Stefanus Harjo, Takuro Kawasaki, Bing Wang, Si Lan, Zhenduo Wu, Feng Wang, Yuan Wu, Zhaoping Lu, Zhongwu Zhang, Chain T. Liu, and Xun-Li Wang. Cooperative deformation in high-entropy alloys at ultralow temperatures. *Science Advances*, 6(13):eaax4002, 2020.

[45] Easo P George and Robert O Ritchie. High-entropy materials. *MRS Bulletin*, 47(2):145–150, 2022.

[46] Shiteng Zhao, Zezhou Li, Chaoyi Zhu, Wen Yang, Zhouran Zhang, David E. J. Armstrong, Patrick S. Grant, Robert O. Ritchie, and Marc A. Meyers. Amorphization in extreme deformation of the CrMnFeCoNi high-entropy alloy. *Science Advances*, 7(5):eabb3108, 2021.

[47] Hao Wang, Dengke Chen, Xianghai An, Yin Zhang, Shijie Sun, Yanzhong Tian, Zhefeng Zhang, Anguo Wang, Jinqiao Liu, Min Song, Simon P. Ringer, Ting Zhu, and Xiaozhou Liao. Deformation-induced crystalline-to-amorphous phase transformation in a CrMnFeCoNi high-entropy alloy. *Science Advances*, 7(14):eabe3105, 2021.

[48] W. Kohn and L. J. Sham. Self-consistent equations including exchange and correlation effects. *Phys. Rev.*, 140:A1133–A1138, Nov 1965.

[49] Partha Pratim Ray. Chatgpt: A comprehensive review on background, applications, key challenges, bias, ethics, limitations and future scope. *Internet of Things and Cyber-Physical Systems*, 3:121–154, 2023.

[50] Jessica Vamathevan, Dominic Clark, Paul Czodrowski, Ian Dunham, Edgardo Ferran, George Lee, Bin Li, Anant Madabhushi, Parantu Shah, Michaela Spitzer, et al. Applications of machine learning in drug discovery and development. *Nature reviews Drug discovery*, 18(6):463–477, 2019.

[51] Joseph A Cruz and David S Wishart. Applications of machine learning in cancer prediction and prognosis. *Cancer informatics*, 2:117693510600200030, 2006.

[52] Geert Litjens, Thijs Kooi, Babak Ehteshami Bejnordi, Arnaud Arindra Adiyoso Setio, Francesco Ciompi, Mohsen Ghafoorian, Jeroen Awm Van Der Laak, Bram Van Ginneken, and Clara I Sánchez. A survey on deep learning in medical image analysis. *Medical image analysis*, 42:60–88, 2017.

[53] Gregory Koch, Richard Zemel, Ruslan Salakhutdinov, et al. Siamese neural networks for one-shot image recognition. In *ICML deep learning workshop*, volume 2. Lille, 2015.

[54] Ge Wang, Jong Chu Ye, Klaus Mueller, and Jeffrey A Fessler. Image reconstruction is a new frontier of machine learning. *IEEE transactions on medical imaging*, 37(6):1289–1296, 2018.

[55] Bo Zhu, Jeremiah Z Liu, Stephen F Cauley, Bruce R Rosen, and Matthew S Rosen. Image reconstruction by domain-transform manifold learning. *Nature*, 555(7697):487–492, 2018.

[56] Xiao Xiang Zhu, Devis Tuia, Lichao Mou, Gui-Song Xia, Liangpei Zhang, Feng Xu, and Friedrich Fraundorfer. Deep learning in remote sensing: A comprehensive review and list of resources. *IEEE geoscience and remote sensing magazine*, 5(4):8–36, 2017.

[57] Aaron E Maxwell, Timothy A Warner, and Fang Fang. Implementation of machine-learning classification in remote sensing: An applied review. *International journal of remote sensing*, 39(9):2784–2817, 2018.

[58] David Rolnick, Priya L Donti, Lynn H Kaack, Kelly Kochanski, Alexandre Lacoste, Kris Sankaran, Andrew Slavin Ross, Nikola Milojevic-Dupont, Natasha Jaques, Anna Waldman-Brown, et al. Tackling climate change with machine learning. *ACM Computing Surveys (CSUR)*, 55(2):1–96, 2022.

[59] Yaguo Lei, Bin Yang, Xinwei Jiang, Feng Jia, Naipeng Li, and Asoke K. Nandi. Applications of machine learning to machine fault diagnosis: A review and roadmap. *Mechanical Systems and Signal Processing*, 138:106587, 2020.

[60] Jonathan Schmidt, Mário RG Marques, Silvana Botti, and Miguel AL Marques. Recent advances and applications of machine learning in solid-state materials science. *npj Computational Materials*, 5(1):83, 2019.

[61] Keith T Butler, Daniel W Davies, Hugh Cartwright, Olexandr Isayev, and Aron Walsh. Machine learning for molecular and materials science. *Nature*, 559(7715):547–555, 2018.

[62] Tian Xie and Jeffrey C. Grossman. Crystal graph convolutional neural networks for an accurate and interpretable prediction of material properties. *Phys. Rev. Lett.*, 120:145301, Apr 2018.

[63] Aneesur Rahman. Correlations in the motion of atoms in liquid argon. *Physical review*, 136(2A):A405, 1964.

[64] Xipeng Wang, Simón Ramírez-Hinestrosa, Jure Dobnikar, and Daan Frenkel. The lennard-jones potential: when (not) to use it. *Physical Chemistry Chemical Physics*, 22(19):10624–10633, 2020.

[65] Jörg Behler. Perspective: Machine learning potentials for atomistic simulations. *The Journal of chemical physics*, 145(17), 2016.

[66] Y. Mishin. Machine-learning interatomic potentials for materials science. *Acta Materialia*, 214:116980, 2021.

[67] Soumya Sanyal, Arun Kumar Sagotra, Narendra Kumar, Sharad Rathi, Mohana Krishna, Nagesh Somayajula, Duraivelan Palanisamy, Ram R Ratnakar, Suchismita Sanyal, Partha Talukdar, et al. Potential energy surface prediction of alumina polymorphs using graph neural network. *arXiv preprint arXiv:2301.12059*, 2023.

[68] Igor Levin and David Brandon. Metastable alumina polymorphs: Crystal structures and transition sequences. *Journal of the American Ceramic Society*, 81(8):1995–2012, 1998.

[69] Anubhav Jain, Shyue Ping Ong, Geoffroy Hautier, Wei Chen, William Davidson Richards, Stephen Dacek, Shreyas Cholia, Dan Gunter, David Skinner, Gerbrand Ceder, and Kristin A. Persson. Commentary: The Materials Project: A materials genome approach to accelerating materials innovation. *APL Mater.*, 1(1):011002, 2013.

[70] Stefano Curtarolo, Wahyu Setyawan, Shidong Wang, Junkai Xue, Kesong Yang, Richard H. Taylor, Lance J. Nelson, Gus L.W. Hart, Stefano Sanvito, Marco Buongiorno-Nardelli, Natalio Mingo, and Ohad Levy. Aflowlib.org: A distributed materials properties repository from high-throughput ab initio calculations. *Computational Materials Science*, 58:227–235, 2012.

[71] Claudia Draxl and Matthias Scheffler. The nomad laboratory: from data sharing to artificial intelligence. *Journal of Physics: Materials*, 2(3):036001, 2019.

[72] Arun Mannodi-Kanakkithodi, Gregory M. Treich, Tran Doan Huan, Rui Ma, Mattewos Tefferi, Yang Cao, Gregory A. Sotzing, and Rampi Ramprasad. Rational Co-Design of Polymer Dielectrics for Energy Storage. *Adv. Mater. (Weinheim, Ger.)*, 28(30):6277–6291, August 2016.

[73] James E. Saal, Scott Kirklin, Muratahan Aykol, Bryce Meredig, and C. Wolverton. Materials Design and Discovery with High-Throughput Density Functional Theory: The Open Quantum Materials Database (OQMD). *JOM*, 65(11):1501–1509, November 2013.

[74] Alec Belsky, Mariette Hellenbrandt, Vicky Lynn Karen, and Peter Luksch. New developments in the inorganic crystal structure database (ICSD): accessibility in support of materials research and design. *Acta Crystallographica Section B: Structural Science*, 58(3):364–369, 2002.

[75] Andriy Zakutayev, Nick Wunder, Marcus Schwarting, John D Perkins, Robert White, Kristin Munch, William Tumas, and Caleb Phillips. An open experimental database for exploring inorganic materials. *Scientific data*, 5(1):1–12, 2018.

[76] NIST data webpage. https://www.nist.gov/data. Accessed: 2023-11-29.

[77] Gabriel R Schleder, Antonio CM Padilha, Carlos Mera Acosta, Marcio Costa, and Adalberto Fazzio. From dft to machine learning: recent approaches to materials science–a review. *Journal of Physics: Materials*, 2(3):032001, 2019.

[78] George AF Seber and Alan J Lee. *Linear regression analysis*, volume 330. John Wiley & Sons, 2003.

[79] Chih-Chung Chang and Chih-Jen Lin. Libsvm: a library for support vector machines. *ACM transactions on intelligent systems and technology (TIST)*, 2(3):1–27, 2011.

[80] Yann LeCun, Yoshua Bengio, and Geoffrey Hinton. Deep learning. *nature*, 521(7553):436–444, 2015.

[81] Ian Goodfellow, Yoshua Bengio, and Aaron Courville. *Deep learning*. MIT press, 2016.

[82] Amirata Ghorbani, Abubakar Abid, and James Zou. Interpretation of neural networks is fragile. In *Proceedings of the AAAI conference on artificial intelligence*, volume 33, pages 3681–3688, 2019.

[83] Chiho Kim, Ghanshyam Pilania, and Ramamurthy Ramprasad. From Organized High-Throughput Data to Phenomenological Theory using Machine Learning: The Example of Dielectric Breakdown. *Chem. Mater.*, 28(5):1304–1311, March 2016.

[84] Praveen Pankajakshan, Suchismita Sanyal, Onno E. de Noord, Indranil Bhattacharya, Arnab Bhattacharyya, and Umesh Waghmare. Machine Learning and Statistical Analysis for Materials Science: Stability and Transferability of Fingerprint Descriptors and Chemical Insights. *Chem. Mater.*, 29(10):4190–4201, May 2017.

[85] Narendra Kumar, Padmini Rajagopalan, Praveen Pankajakshan, Arnab Bhattacharyya, Suchismita Sanyal, Janakiraman Balachandran, and Umesh V. Waghmare. Machine learning constrained with dimensional analysis and scaling laws: Simple, transferable, and interpretable models of materials from small datasets. *Chemistry of Materials*, 31(2):314–321, 2019.

[86] Israel Cohen, Yiteng Huang, Jingdong Chen, Jacob Benesty, Jacob Benesty, Jingdong Chen, Yiteng Huang, and Israel Cohen. Pearson correlation coefficient. *Noise reduction in speech processing*, pages 1–4, 2009.

[87] Marvin L Cohen. Calculation of bulk moduli of diamond and zinc-blende solids. *Phys. Rev. B: Condens. Matter Mater. Phys.*, 32(12):7988, 1985.

[88] John Robertson. High dielectric constant gate oxides for metal oxide Si transistors. *Rep. Prog. Phys.*, 69(2):327, 2005.

[89] Aaron Clauset, Cosma Rohilla Shalizi, and M. E. J. Newman. Power-law distributions in empirical data. *SIAM Review*, 51(4):661–703, 2009.

[90] Louis Brand. The Pi theorem of dimensional analysis. *Arch. Ration. Mech. Anal.*, 1(1):35–45, 1957.

[91] Ge Wang, Zhilun Lu, Yong Li, Linhao Li, Hongfen Ji, Antonio Feteira, Di Zhou, Dawei Wang, Shujun Zhang, and Ian M Reaney. Electroceramics for high-energy density capacitors: Current status and future perspectives. *Chemical Reviews*, 121(10):6124–6172, 2021. PMID: 33909415.

[92] Fenglin Yuan and Tim Mueller. Identifying models of dielectric breakdown strength from high-throughput data via genetic programming. *Sci. Rep.*, 7(1):17594, December 2017.

[93] Eduardo Caetano Camilo de Souza and Reginaldo Muccillo. Properties and applications of perovskite proton conductors. *Materials Research*, 13(3):385–394, Jul 2010.

[94] Tatsumi Ishihara. *Perovskite oxide for solid oxide fuel cells*. Springer Science & Business Media, 2009.

[95] K.D Kreuer. Aspects of the formation and mobility of protonic charge carriers and the stability of perovskite-type oxides. *Solid State Ionics*, 125(1):285–302, 1999.

[96] G Venkataraman. Soft modes and structural phase transitions. *Bulletin of Materials Science*, 1:129–170, 1979.

[97] Göran Grimvall, Blanka Magyari-Köpe, Vidvuds Ozoliņš, and Kristin A. Persson. Lattice instabilities in metallic elements. *Rev. Mod. Phys.*, 84:945–986, Jun 2012.

[98] Atsushi Togo and Isao Tanaka. First principles phonon calculations in materials science. *Scripta Materialia*, 108:1–5, 2015.

[99] Wolfgang Lechner and Christoph Dellago. Accurate determination of crystal structures based on averaged local bond order parameters. *J. Chem. Phys.*, 129(11):114707, 2008.

[100] Alexander Stukowski. Structure identification methods for atomistic simulations of crystalline materials. *Modelling and Simulation in Materials Science and Engineering*, 20(4):045021, 2012.

[101] Wesley F Reinhart, Andrew W Long, Michael P Howard, Andrew L Ferguson, and Athanassios Z Panagiotopoulos. Machine learning for autonomous crystal structure identification. *Soft Matter*, 13(27):4733–4745, 2017.

[102] Narendra Kumar and Umesh V. Waghmare. Entropic stabilization and descriptors of structural transformation in high entropy alloys. *Acta Materialia*, 255:119077, 2023.

[103] J. P Troadec, A Gervois, and L Oger. Statistics of voronoi cells of slightly perturbed face-centered cubic and hexagonal close-packed lattices. *Europhys. Lett.*, 42(2):167–172, 1998.

[104] Paul J. Steinhardt, David R. Nelson, and Marco Ronchetti. Bond-orientational order in liquids and glasses. *Phys. Rev. B*, 28:784–805, Jul 1983.

[105] EC Bain. A new orientation relationshp between fcc and bcc. *Trans. Metall. Soc. AIME*, 70:25, 1924.

[106] M Černý and J Pokluda. The theoretical tensile strength of fcc crystals predicted from shear strength calculations. *Journal of Physics: Condensed Matter*, 21(14):145406, 2009.

[107] M. Černý, P. Šesták, J. Pokluda, and M. Šob. Shear instabilities in perfect bcc crystals during simulated tensile tests. *Phys. Rev. B*, 87:014117, Jan 2013.

[108] Jinghan Wang, Ju Li, Sidney Yip, Simon Phillpot, and Dieter Wolf. Mechanical instabilities of homogeneous crystals. *Phys. Rev. B*, 52:12627–12635, Nov 1995.

[109] John P Holdren et al. Materials genome initiative for global competitiveness. *National Science and technology council OSTP. Washington, USA*, 2011.

[110] Matthew T. Dunstan, Anubhav Jain, Wen Liu, Shyue Ping Ong, Tao Liu, Jeongjae Lee, Kristin A. Persson, Stuart A. Scott, John S. Dennis, and Clare P. Grey. Large

scale computational screening and experimental discovery of novel materials for high temperature CO_2 capture. *Energy Environ. Sci.*, 9(4):1346–1360, 2016.

[111] Maarten de Jong, Wei Chen, Henry Geerlings, Mark Asta, and Kristin Aslaug Persson. A database to enable discovery and design of piezoelectric materials. *Sci. Data*, 2:150053, September 2015.

[112] Vinit Sharma, Chenchen Wang, Robert G. Lorenzini, Rui Ma, Qiang Zhu, Daniel W. Sinkovits, Ghanshyam Pilania, Artem R. Oganov, Sanat Kumar, Gregory A. Sotzing, Steven A. Boggs, and Rampi Ramprasad. Rational design of all organic polymer dielectrics. *Nat. Commun.*, 5:4845, September 2014.

[113] Liping Yu and Alex Zunger. Identification of potential photovoltaic absorbers based on first-principles spectroscopic screening of materials. *Phys. Rev. Lett.*, 108:068701, Feb 2012.

[114] Vancho Kocevski and Chris Wolverton. Designing High-Efficiency Nanostructured Two-Phase Heusler Thermoelectrics. *Chem. Mater.*, 29(21):9386–9398, November 2017.

[115] Olexandr Isayev, Corey Oses, Cormac Toher, Eric Gossett, Stefano Curtarolo, and Alexander Tropsha. Universal fragment descriptors for predicting properties of inorganic crystals. *Nat. Commun.*, 8:15679, 2017.

[116] Luca M. Ghiringhelli, Jan Vybiral, Sergey V. Levchenko, Claudia Draxl, and Matthias Scheffler. Big Data of Materials Science: Critical Role of the Descriptor. *Phys. Rev. Lett.*, 114(10):105503, March 2015.

[117] Maarten de Jong, Wei Chen, Randy Notestine, Kristin Persson, Gerbrand Ceder, Anubhav Jain, Mark Asta, and Anthony Gamst. A Statistical Learning Framework for Materials Science: Application to Elastic Moduli of k-nary Inorganic Polycrystalline Compounds. *Sci. Rep.*, 6:34256, October 2016.

[118] Atsuto Seko, Hiroyuki Hayashi, Keita Nakayama, Akira Takahashi, and Isao Tanaka. Representation of compounds for machine-learning prediction of physical properties. *Phys. Rev. B: Condens. Matter Mater. Phys.*, 95:144110, Apr 2017.

[119] Keith T. Butler, Daniel W. Davies, Hugh Cartwright, Olexandr Isayev, and Aron Walsh. Machine learning for molecular and materials science. *Nature*, 559(7715):547–555, July 2018.

[120] Robert Tibshirani. Regression Shrinkage and Selection via the Lasso. *J. R. Stat. Soc. Series B Stat. Methodol.*, 58(1):267–288, 1996.

[121] Clarence Zener. A Theory of the Electrical Breakdown of Solid Dielectrics. *Proc. R. Soc. London, Ser. A*, 145(855):523–529, 1934.

[122] F Aguado and VG Baonza. Prediction of bulk modulus at high temperatures from longitudinal phonon frequencies: Application to diamond, c- bn, and 3 c- sic. *Phys. Rev. B: Condens. Matter Mater. Phys.*, 73(2):024111, 2006.

[123] Kanghoon Yim, Youn Yong, Joohee Lee, Kyuhyun Lee, Ho-Hyun Nahm, Jiho Yoo, Chanhee Lee, Cheol Seong Hwang, and Seungwu Han. Novel high-κ dielectrics for next-generation electronic devices screened by automated ab initio calculations. *NPG Asia Mater.*, 7(6):e190–e190, 2015.

[124] Indranil Bhattacharya. *Feature Selection under Multicollinearity & Causal Inference on Time Series*. PhD thesis, Indian Institute of Science, 2017.

[125] Bradley Efron and Robert J Tibshirani. *An Introduction to the Bootstrap*. CRC press, 1994.

[126] Prateek Jain, Ambuj Tewari, and Purushottam Kar. On iterative hard thresholding methods for high-dimensional m-estimation. In *Advances in Neural Information Processing Systems*, pages 685–693, 2014.

[127] J. McPherson, J. Kim, A. Shanware, H. Mogul, and J. Rodriguez. Proposed universal relationship between dielectric breakdown and dielectric constant. In *Digest. International Electron Devices Meeting,*, pages 633–636, December 2002.

[128] Y. Sun, C. Bealing, S. Boggs, and R. Ramprasad. 50+ years of intrinsic breakdown. *IEEE Electr. Insul. Mag.*, 29(2):8–15, March 2013.

[129] Chiho Kim, Ghanshyam Pilania, and Rampi Ramprasad. Machine learning assisted predictions of intrinsic dielectric breakdown strength of abx3 perovskites. *J. Phys. Chem. C*, 120(27):14575–14580, 2016.

[130] Shuaihua Lu, Qionghua Zhou, Yixin Ouyang, Yilv Guo, Qiang Li, and Jinlan Wang. Accelerated discovery of stable lead-free hybrid organic-inorganic perovskites via machine learning. *Nat. Commun.*, 9(1):3405, dec 2018.

[131] Ying Zhang and Chen Ling. A strategy to apply machine learning to small datasets in materials science. *NPJ Comput. Mater.*, 4(1):25, dec 2018.

[132] Dezhen Xue, Prasanna V. Balachandran, John Hogden, James Theiler, Deqing Xue, and Turab Lookman. Accelerated search for materials with targeted properties by adaptive design. *Nat. Commun.*, 7:11241, apr 2016.

[133] Jack D Evans and François-Xavier Coudert. Predicting the mechanical properties of zeolite frameworks by machine learning. *Chem. Mater.*, 29(18):7833–7839, 2017.

[134] Liu Xu, Lu Wencong, Peng Chunrong, Su Qiang, and Guo Jin. Two semi-empirical approaches for the prediction of oxide ionic conductivities in ABO_3 perovskites. *Computational Materials Science*, 46(4):860–868, 2009.

[135] N. Bonanos. Oxide-based protonic conductors: point defects and transport properties. *Solid State Ionics*, 145(1):265–274, 2001. Proceedings of the 10th International Conference on Solid State Protonic Conductors.

[136] N. Bork, N. Bonanos, J. Rossmeisl, and T. Vegge. Simple descriptors for proton-conducting perovskites from density functional theory. *Phys. Rev. B*, 82:014103, Jul 2010.

[137] Junji Hyodo, Kota Tsujikawa, Motoki Shiga, Yuji Okuyama, and Yoshihiro Yamazaki. Accelerated discovery of proton-conducting perovskite oxide by capturing physicochemical fundamentals of hydration. *ACS Energy Letters*, 6(8):2985–2992, 2021.

[138] Paolo Giannozzi, Stefano Baroni, Nicola Bonini, Matteo Calandra, Roberto Car, Carlo Cavazzoni, Davide Ceresoli, Guido L Chiarotti, Matteo Cococcioni, Ismaila Dabo, et al.

Quantum espresso: a modular and open-source software project for quantum simulations of materials. *J. Phys.: Condens. Matter*, 21(39):395502, 2009.

[139] John P. Perdew, J. A. Chevary, S. H. Vosko, Koblar A. Jackson, Mark R. Pederson, D. J. Singh, and Carlos Fiolhais. Atoms, molecules, solids, and surfaces: Applications of the generalized gradient approximation for exchange and correlation. *Phys. Rev. B*, 46:6671–6687, Sep 1992.

[140] John P. Perdew, Kieron Burke, and Matthias Ernzerhof. Generalized gradient approximation made simple. *Phys. Rev. Lett.*, 77:3865–3868, Oct 1996.

[141] David Vanderbilt. Soft self-consistent pseudopotentials in a generalized eigenvalue formalism. *Phys. Rev. B*, 41:7892–7895, Apr 1990.

[142] Graeme Henkelman, Blas P. Uberuaga, and Hannes Jónsson. A climbing image nudged elastic band method for finding saddle points and minimum energy paths. *The Journal of Chemical Physics*, 113(22):9901–9904, 12 2000.

[143] Donald G. Truhlar, Bruce C. Garrett, and Stephen J. Klippenstein. Current status of transition-state theory. *The Journal of Physical Chemistry*, 100(31):12771–12800, 1996.

[144] Xavier Gonze and Changyol Lee. Dynamical matrices, born effective charges, dielectric permittivity tensors, and interatomic force constants from density-functional perturbation theory. *Phys. Rev. B*, 55:10355–10368, Apr 1997.

[145] K.D. Kreuer. Proton-conducting oxides. *Annual Review of Materials Research*, 33(1):333–359, 2003.

[146] Eiko Matsushita and Toshiaki Sasaki. Theoretical approach for protonic conduction in perovskite-type oxides. *Solid State Ionics*, 125(1):31–37, 1999.

[147] Qianfan Zhang, Göran Wahnström, Mårten E. Björketun, Shiwu Gao, and Enge Wang. Path integral treatment of proton transport processes in bazro$_3$. *Phys. Rev. Lett.*, 101:215902, Nov 2008.

[148] K.-D. Kreuer, A. Fuchs, and J. Maier. HD isotope effect of proton conductivity and proton conduction mechanism in oxides. *Solid State Ionics*, 77:157–162, 1995. Solid State Protonic Conductors VII.

[149] Sung Gu Kang and David S. Sholl. First principles studies of proton conduction in KTaO3. *The Journal of Chemical Physics*, 141(2):024707, 07 2014.

[150] Truls Norby, Marius Widerøe, Ronny Glöckner, and Yngve Larring. Hydrogen in oxides. *Dalton Trans.*, pages 3012–3018, 2004.

[151] Katsuyoshi Kakinuma, Hiroshi Yamamura, Hajime Haneda, and Tooru Atake. Oxide-ion conductivity of the perovskite-type solid-solution system, $(Ba_{1-x-y}Sr_xLa_y)_2In_2O_{5+y}$. *Solid State Ionics*, 154-155:571–576, 2002.

[152] Volker L. Deringer, Albert P. Bartók, Noam Bernstein, David M. Wilkins, Michele Ceriotti, and Gábor Csányi. Gaussian process regression for materials and molecules. *Chemical Reviews*, 121(16):10073–10141, 2021.

[153] Yong Zhang, Ting Ting Zuo, Zhi Tang, Michael C. Gao, Karin A. Dahmen, Peter K. Liaw, and Zhao Ping Lu. Microstructures and properties of high-entropy alloys. *Progress in Materials Science*, 61:1–93, 2014.

[154] Bhagevatula Satyanarayana Murty, Jien-Wei Yeh, Srinivasa Ranganathan, and PP Bhattacharjee. *High-entropy alloys*. Elsevier, 2019.

[155] Yong Zhang, Yun Jun Zhou, Jun Pin Lin, Guo Liang Chen, and Peter K Liaw. Solid-solution phase formation rules for multi-component alloys. *Advanced engineering materials*, 10(6):534–538, 2008.

[156] QF He, YF Ye, and Y Yang. Formation of random solid solution in multicomponent alloys: from Hume-Rothery rules to entropic stabilization. *J. Phase Equilibria Diffus.*, 38(4):416–425, 2017.

[157] F. Otto, Y. Yang, H. Bei, and E.P. George. Relative effects of enthalpy and entropy on the phase stability of equiatomic high-entropy alloys. *Acta Mater.*, 61(7):2628–2638, 2013.

[158] Sheng Guo and C. T. Liu. Phase stability in high entropy alloys: Formation of solid-solution phase or amorphous phase. *Prog. Nat. Sci.: Mater. Int.*, 21(6):433–446, 2011.

[159] Y.F. Ye, Q. Wang, J. Lu, C.T. Liu, and Y. Yang. Design of high entropy alloys: A single-parameter thermodynamic rule. *Scr. Mater.*, 104:53–55, 2015.

[160] W. Hume-Rothery, R.W. Smallman, and C.W. Haworth. The structure of metals and alloys. *The Institute of Metals, London (1969)*, 1969.

[161] M Claudia Troparevsky, James R Morris, Markus Daene, Yang Wang, Andrew R Lupini, and G Malcolm Stocks. Beyond atomic sizes and hume-rothery rules: understanding and predicting high-entropy alloys. *Jom*, 67(10):2350–2363, 2015.

[162] Jitesh Kumar, Albert Linda, M Sadhasivam, KG Pradeep, NP Gurao, and Krishanu Biswas. The effect of si addition on the structure and mechanical properties of equiatomic cocrfemnni high entropy alloy by experiment and simulation. *Materialia*, 27:101707, 2023.

[163] Lewis Robert Owen and Nicholas Gwilym Jones. Lattice distortions in high-entropy alloys. *Journal of Materials Research*, 33(19):2954–2969, 2018.

[164] Alex Zunger, S.-H. Wei, L. G. Ferreira, and James E. Bernard. Special quasirandom structures. *Phys. Rev. Lett.*, 65:353–356, Jul 1990.

[165] A. van de Walle, M. Asta, and G. Ceder. The alloy theoretic automated toolkit: A user guide. *Calphad*, 26(4):539–553, 2002.

[166] A. van de Walle, P. Tiwary, M. de Jong, D.L. Olmsted, M. Asta, A. Dick, D. Shin, Y. Wang, L.-Q. Chen, and Z.-K. Liu. Efficient stochastic generation of special quasirandom structures. *Calphad*, 42:13–18, 2013.

[167] Joanne L Murray, Lawrence Herman Bennett, and Hugh Baker. *Binary alloy phase diagrams*, volume 2. ASM International (OH), 1986.

[168] C Colinet, A Bessoud, and A Pasturel. Theoretical determinations of thermodynamic data and phase diagrams of BCC binary transition-metal alloys. *J. Phys. F: Met. Phys.*, 18(5):903–921, may 1988.

[169] A. R. Denton and N. W. Ashcroft. Vegard's law. *Phys. Rev. A*, 43:3161–3164, Mar 1991.

[170] Y. X. Ye, Z. P. Lu, and T. G. Nieh. Dislocation nucleation during nanoindentation in a body-centered cubic TiZrHfNb high-entropy alloy. *Scr. Mater.*, 130:64–68, 2017.

[171] Y. X. Ye, C. Z. Liu, H. Wang, and T. G. Nieh. Friction and wear behavior of a single-phase equiatomic TiZrHfNb high-entropy alloy studied using a nanoscratch technique. *Acta Mater.*, 147:78–89, 2018.

[172] P. E. Blöchl. Projector augmented-wave method. *Phys. Rev. B*, 50:17953–17979, Dec 1994.

[173] https://github.com/dalcorso/thermo_pw.

[174] Sarath Menon, Grisell Díaz Leines, and Jutta Rogal. pyscal: A python module for structural analysis of atomic environments. *J. Open Source Softw.*, 4(43):1824, 2019.

[175] Chris Rycroft. Voro++: A three-dimensional voronoi cell library in c++. Technical report, Lawrence Berkeley National Lab.(LBNL), Berkeley, CA (United States), 2009.

[176] E. S. Fisher and C. J. Renken. Single-crystal elastic moduli and the hcp $\rightarrow$ bcc transformation in Ti, Zr, and Hf. *Phys. Rev.*, 135:A482–A494, Jul 1964.

[177] Anirudh Raju Natarajan, Pavel Dolin, and Anton Van der Ven. Crystallography, thermodynamics and phase transitions in refractory binary alloys. *Acta Materialia*, 200:171–186, 2020.

[178] Long Zhang, Huameng Fu, Shaofan Ge, Zhengwang Zhu, Hong Li, Hongwei Zhang, Aiming Wang, and Haifeng Zhang. Phase transformations in body-centered cubic NbxHfZrTi high-entropy alloys. *Mater. Charact.*, 142:443–448, 2018.

[179] G. D. Samolyuk, Y. N. Osetsky, G. M. Stocks, and J. R. Morris. Role of static displacements in stabilizing body centered cubic high entropy alloys. *Phys. Rev. Lett.*, 126:025501, Jan 2021.

[180] Quanfeng He and Yong Yang. On lattice distortion in high entropy alloys. *Frontiers in Materials*, 5:42, 2018.

[181] Xuefei Chen, Qi Wang, Zhiying Cheng, Mingliu Zhu, Hao Zhou, Ping Jiang, Lingling Zhou, Qiqi Xue, Fuping Yuan, Jing Zhu, et al. Direct observation of chemical short-range order in a medium-entropy alloy. *Nature*, 592(7856):712–716, 2021.

[182] Yuan Yuan, Yuan Wu, Zhi Yang, Xue Liang, Zhifeng Lei, Hailong Huang, Hui Wang, Xiongjun Liu, Ke An, Wei Wu, et al. Formation, structure and properties of biocompatible tizrhfnbta high-entropy alloys. *Materials Research Letters*, 7(6):225–231, 2019.

[183] Hailong Huang, Yuan Wu, Junyang He, Hui Wang, Xiongjun Liu, Ke An, Wei Wu, and Zhaoping Lu. Phase-transformation ductilization of brittle high-entropy alloys via metastability engineering. *Advanced Materials*, 29(30):1701678, 2017.

[184] Peng Wang, Yeqiang Bu, Jiabin Liu, Qianqian Li, Hongtao Wang, and Wei Yang. Atomic deformation mechanism and interface toughening in metastable high entropy alloy. *Materials Today*, 37:64–73, 2020.

[185] Hongquan Song, Fuyang Tian, Qing-Miao Hu, Levente Vitos, Yandong Wang, Jiang Shen, and Nanxian Chen. Local lattice distortion in high-entropy alloys. *Phys. Rev. Mater.*, 1:023404, Jul 2017.

[186] Zhijun Wang, Weifeng Qiu, Yong Yang, and C.T. Liu. Atomic-size and lattice-distortion effects in newly developed high-entropy alloys with multiple principal elements. *Intermetallics*, 64:63–69, 2015.

[187] Keyan Li and Dongfeng Xue. Estimation of electronegativity values of elements in different valence states. *The Journal of Physical Chemistry A*, 110(39):11332–11337, 2006.

[188] Bozhao Zhang, Jun Ding, and En Ma. Chemical short-range order in body-centered-cubic tizrhfnb high-entropy alloys. *Applied Physics Letters*, 119(20):201908, 2021.

[189] Ruopeng Zhang, Yujie Chen, Yan Fang, and Qian Yu. Characterization of chemical local ordering and heterogeneity in high-entropy alloys. *MRS Bulletin*, 47(2):186–193, 2022.

[190] Fanchao Meng, Wenyan Zhang, Zhukun Zhou, Ruixin Sheng, Andrew C-P Chuang, Chongchong Wu, Hailiang Huang, Shangzhou Zhang, Hua Zhang, Lilong Zhu, et al. Charge transfer effect on local lattice distortion in a hfnbtizr high entropy alloy. *Scripta Materialia*, 203:114104, 2021.

[191] Luis Casillas-Trujillo, Barbara Osinger, Rebecka Lindblad, Dennis Karlsson, Alexei I Abrikosov, Stefan Fritze, Kristina von Fieandt, Björn Alling, Ingrid Hotz, Ulf Jansson,

et al. Experimental and theoretical evidence of charge transfer in multi-component alloys–how chemical interactions reduce atomic size mismatch. *Materials Chemistry Frontiers*, 5(15):5746–5759, 2021.

[192] Tobias Brink, Leonie Koch, and Karsten Albe. Structural origins of the boson peak in metals: From high-entropy alloys to metallic glasses. *Physical Review B*, 94(22):224203, 2016.

[193] Shelby R Turner, Stéphane Pailhès, Frédéric Bourdarot, Jacques Ollivier, Yvan Sidis, John-Paul Castellan, Jean-Marc Zanotti, Quentin Berrod, Florence Porcher, Alexei Bosak, et al. Phonon behavior in a random solid solution: a lattice dynamics study on the high-entropy alloy FeCoCrMnNi. *Nature Communications*, 13(1):7509, 2022.

[194] Giulio Monaco and Valentina M Giordano. Breakdown of the Debye approximation for the acoustic modes with nanometric wavelengths in glasses. *Proceedings of the national Academy of Sciences*, 106(10):3659–3663, 2009.

[195] Hideyuki Mizuno, Hayato Shiba, and Atsushi Ikeda. Continuum limit of the vibrational properties of amorphous solids. *Proceedings of the National Academy of Sciences*, 114(46):E9767–E9774, 2017.

[196] Duancheng Ma, Blazej Grabowski, Fritz Körmann, Jörg Neugebauer, and Dierk Raabe. Ab initio thermodynamics of the CoCrFeMnNi high entropy alloy: Importance of entropy contributions beyond the configurational one. *Acta Mater.*, 100:90–97, 2015.

[197] Daan Frenkel. Entropy-driven phase transitions. *Physica A: statistical mechanics and its applications*, 263(1-4):26–38, 1999.

[198] Chenyi Yi, Jingshan Luo, Simone Meloni, Ariadni Boziki, Negar Ashari-Astani, Carole Grätzel, Shaik M Zakeeruddin, Ursula Röthlisberger, and Michael Grätzel. Entropic stabilization of mixed A-cation ABX_3 metal halide perovskites for high performance perovskite solar cells. *Energy & Environmental Science*, 9(2):656–662, 2016.

[199] Corey Oses, Cormac Toher, and Stefano Curtarolo. High-entropy ceramics. *Nature Reviews Materials*, 5(4):295–309, 2020.

[200] Anus Manzoor, Shubham Pandey, Debajit Chakraborty, Simon R Phillpot, and Dilpuneet S Aidhy. Entropy contributions to phase stability in binary random solid solutions. *npj Computational Materials*, 4(1):47, 2018.

[201] R.E. Ryltsev, S.Kh. Estemirova, V.S. Gaviko, D.A. Yagodin, V.A. Bykov, E.V. Sterkhov, L.A. Cherepanova, I.S. Sipatov, I.A. Balyakin, and S.A. Uporov. Structural evolution in TiZrHfNb high-entropy alloy. *Materialia*, 21:101311, 2022.

[202] Azkar S. Ahmad, Y. Su, S. Y. Liu, K. Ståhl, Y. D. Wu, X. D. Hui, U. Ruett, O. Gutowski, K. Glazyrin, H. P. Liermann, H. Franz, H. Wang, X. D. Wang, Q. P. Cao, D. X. Zhang, and J. Z. Jiang. Structural stability of high entropy alloys under pressure and temperature. *Journal of Applied Physics*, 121(23):235901, 06 2017.

[203] Corey Oses, Cormac Toher, and Stefano Curtarolo. High-entropy ceramics. *Nature Reviews Materials*, 5(4):295–309, 2020.

[204] Ye Liu, Jiyuan Yang, Shiqing Deng, Yueyun Zhang, Yongcheng Zhang, Shengdong Sun, Lu Wang, Xiaodong Jiang, Chuanrui Huo, Hui Liu, He Qi, Shi Liu, and Jun Chen. Flexible polarization configuration in high-entropy piezoelectrics with high performance. *Acta Materialia*, 236:118115, 2022.

[205] He Qi, Liang Chen, Shiqing Deng, and Jun Chen. High-entropy ferroelectric materials. *Nature Reviews Materials*, pages 1–2, 2023.

[206] Man Zhang, Xinzhao Xu, Shafique Ahmed, Yajun Yue, Matteo Palma, Peter Svec, Feng Gao, Isaac Abrahams, Michael J. Reece, and Haixue Yan. Phase transformations in an aurivillius layer structured ferroelectric designed using the high entropy concept. *Acta Materialia*, 229:117815, 2022.

[207] Yogesh Sharma, Min-Cheol Lee, Krishna Chaitanya Pitike, Karuna K Mishra, Qiang Zheng, Xiang Gao, Brianna L Musico, Alessandro R Mazza, Ram S Katiyar, Veerle Keppens, et al. High entropy oxide relaxor ferroelectrics. *ACS Applied Materials & Interfaces*, 14(9):11962–11970, 2022.

[208] Abhishek Sarkar, Di Wang, Mohana V. Kante, Luis Eiselt, Vanessa Trouillet, Gleb Iankevich, Zhibo Zhao, Subramshu S. Bhattacharya, Horst Hahn, and Robert Kruk. High

entropy approach to engineer strongly correlated functionalities in manganites. *Advanced Materials*, 35(2):2207436, 2023.

[209] Jing Hu, Lujie Cao, Zhenyu Wang, Jinlong Liu, Junjun Zhang, Yulin Cao, Zhouguang Lu, and Hua Cheng. Hollow high-entropy metal organic framework derived nanocomposite as efficient electrocatalyst for oxygen reduction reaction. *Composites Communications*, 27:100866, 2021.

[210] Xinhui Zhao, Zhimin Xue, Wenjun Chen, Xiyue Bai, Ruifen Shi, and Tiancheng Mu. Ambient fast, large-scale synthesis of entropy-stabilized metal–organic framework nanosheets for electrocatalytic oxygen evolution. *Journal of Materials Chemistry A*, 7(46):26238–26242, 2019.

[211] Xiaoshi Qian, Donglin Han, Lirong Zheng, Jie Chen, Madhusudan Tyagi, Qiang Li, Feihong Du, Shanyu Zheng, Xingyi Huang, Shihai Zhang, et al. High-entropy polymer produces a giant electrocaloric effect at low fields. *Nature*, 600(7890):664–669, 2021.

[212] Xuan Zhang, Jiahao Yao, Bin Liu, Jun Yan, Lei Lu, Yi Li, Huajian Gao, and Xiaoyan Li. Three-dimensional high-entropy alloy–polymer composite nanolattices that overcome the strength–recoverability trade-off. *Nano letters*, 18(7):4247–4256, 2018.

[213] Bingbing Yang, Yang Zhang, Hao Pan, Wenlong Si, Qinghua Zhang, Zhonghui Shen, Yong Yu, Shun Lan, Fanqi Meng, Yiqian Liu, et al. High-entropy enhanced capacitive energy storage. *Nature Materials*, 21(9):1074–1080, 2022.

[214] Yanjiao Ma, Yuan Ma, Sören Lukas Dreyer, Qingsong Wang, Kai Wang, Damian Goonetilleke, Ahmad Omar, Daria Mikhailova, Horst Hahn, Ben Breitung, and Torsten Brezesinski. High-entropy metal-organic frameworks for highly reversible sodium storage. *Advanced Materials*, 33(34):2101342, 2021.

[215] O.N. Senkov, G.B. Wilks, D.B. Miracle, C.P. Chuang, and P.K. Liaw. Refractory high-entropy alloys. *Intermetallics*, 18(9):1758–1765, 2010.

[216] Michael Widom. Modeling the structure and thermodynamics of high-entropy alloys. *Journal of Materials Research*, 33(19):2881–2898, 2018.

[217] K. Yashiro. Deformation mode analysis by eigenvectors of atomic elastic stiffness in static uniaxial tension of various fcc, bcc, and hcp metals. *AIP Advances*, 10(3):035301, 03 2020.

[218] Félix Mouhat and François-Xavier Coudert. Necessary and sufficient elastic stability conditions in various crystal systems. *Phys. Rev. B*, 90:224104, Dec 2014.

[219] R Hill. The elastic behaviour of a crystalline aggregate. *Proceedings of the Physical Society. Section A*, 65(5):349, may 1952.

[220] Maarten De Jong, Wei Chen, Thomas Angsten, Anubhav Jain, Randy Notestine, Anthony Gamst, Marcel Sluiter, Chaitanya Krishna Ande, Sybrand Van Der Zwaag, Jose J Plata, et al. Charting the complete elastic properties of inorganic crystalline compounds. *Scientific data*, 2(1):1–13, 2015.

[221] Shivakumar I. Ranganathan and Martin Ostoja-Starzewski. Universal elastic anisotropy index. *Phys. Rev. Lett.*, 101:055504, Aug 2008.

[222] Jan W. Jaeken and Stefaan Cottenier. Solving the christoffel equation: Phase and group velocities. *Computer Physics Communications*, 207:445–451, 2016.

[223] Fedor I Fedorov. *Theory of elastic waves in crystals*. Springer Science & Business Media, 2013.

[224] C.R Krenn, D Roundy, J.W Morris, and Marvin L Cohen. Ideal strengths of bcc metals. *Materials Science and Engineering: A*, 319-321:111–114, 2001.

[225] Konrad Polthier, Samy Khadem, Eike Preuß, and Ulrich Reitebuch. Publication of interactive visualizations with java view. In *Multimedia tools for communicating mathematics*, pages 241–264. Springer, 2002.

[226] Lallit Anand and Sanjay Govindjee. *Continuum mechanics of solids*. Oxford University Press, 2020.

[227] Clarence M Zener and Sidney Siegel. Elasticity and anelasticity of metals. *The Journal of Physical Chemistry*, 53(9):1468–1468, 1949.

[228] Yi X. Wang, Hua Y. Geng, Q. Wu, Xiang R. Chen, and Y. Sun. First-principles investigation of elastic anomalies in niobium at high pressure and temperature. *Journal of Applied Physics*, 122(23):235903, 12 2017.

[229] Xiaoqing Li. Phase stability and micromechanical properties of TiZrHf-based refractory high-entropy alloys: A first-principles study. *Phys. Rev. Mater.*, 7:113604, Nov 2023.

[230] S.F. Pugh. Xcii. relations between the elastic moduli and the plastic properties of polycrystalline pure metals. *The London, Edinburgh, and Dublin Philosophical Magazine and Journal of Science*, 45(367):823–843, 1954.

[231] R.P. Thompson and W.J. Clegg. Predicting whether a material is ductile or brittle. *Current Opinion in Solid State and Materials Science*, 22(3):100–108, 2018.

[232] Frederick A Lindemann. Über die berechnung molekularer eigenfrequenzen. *Phys. Z*, 11:609–612, 1910.

[233] Charusita Chakravarty, Pablo G. Debenedetti, and Frank H. Stillinger. Lindemann measures for the solid-liquid phase transition. *J. Chem. Phys.*, 126(20):204508, 2007.

[234] D. Wolf, P. R. Okamoto, S. Yip, J. F. Lutsko, and M. Kluge. Thermodynamic parallels between solid-state amorphization and melting. *Journal of Materials Research*, 5(2):286–301, 1990.

[235] Alessio Zaccone and Eugene M. Terentjev. Disorder-assisted melting and the glass transition in amorphous solids. *Phys. Rev. Lett.*, 110:178002, Apr 2013.

[236] Amit Banerjee, Daniel Bernoulli, Hongti Zhang, Muk-Fung Yuen, Jiabin Liu, Jichen Dong, Feng Ding, Jian Lu, Ming Dao, Wenjun Zhang, Yang Lu, and Subra Suresh. Ultralarge elastic deformation of nanoscale diamond. *Science*, 360(6386):300–302, 2018.

[237] David Roundy and Marvin L. Cohen. Ideal strength of diamond, si, and ge. *Phys. Rev. B*, 64:212103, Nov 2001.

[238] Y.X. Ye, B.L. Musico, Z.Z. Lu, L.B. Xu, Z.F. Lei, V. Keppens, H.X. Xu, and T.G. Nieh. Evaluating elastic properties of a body-centered cubic NbHfZrTi high-entropy alloy – A direct comparison between experiments and ab initio calculations. *Intermetallics*, 109:167–173, 2019.

[239] Hailong Huang, Yan Sun, Peipei Cao, Yuan Wu, Xiongjun Liu, Suihe Jiang, Hui Wang, and Zhaoping Lu. On cooling rates dependence of microstructure and mechanical properties of refractory high-entropy alloys HfTaTiZr and HfNbTiZr. *Scripta Materialia*, 211:114506, 2022.

[240] Y.D. Wu, Y.H. Cai, T. Wang, J.J. Si, J. Zhu, Y.D. Wang, and X.D. Hui. A refractory $Hf_{25}Nb_{25}Ti_{25}Zr_{25}$ high-entropy alloy with excellent structural stability and tensile properties. *Materials Letters*, 130:277–280, 2014.

[241] YH Jo, WM Choi, DG Kim, A Zargaran, SS Sohn, HS Kim, BJ Lee, NJ Kim, and S Lee. FCC to BCC transformation-induced plasticity based on thermodynamic phase stability in novel $V_{10}Cr_{10}Fe_{45}Co_xNi_{35-x}$ medium-entropy alloys. *Scientific reports*, 9(1):2948, 2019.

[242] Masato Wakeda, Yoji Shibutani, Shigenobu Ogata, and Junyoung Park. Relationship between local geometrical factors and mechanical properties for Cu-Zr amorphous alloys. *Intermetallics*, 15(2):139–144, 2007.

[243] Duane C. Wallace. Thermoelasticity of stressed materials and comparison of various elastic constants. *Phys. Rev.*, 162:776–789, Oct 1967.

[244] N. H. Macmillan, Anthony Kelly, and Alan Howard Cottrell. The mechanical properties of perfect crystals ii. the stability and mode of fracture of highly stressed ideal crystals. *Proceedings of the Royal Society of London. A. Mathematical and Physical Sciences*, 330(1582):309–317, 1972.

[245] R. Hill. On the elasticity and stability of perfect crystals at finite strain. *Mathematical Proceedings of the Cambridge Philosophical Society*, 77(1):225–240, 1975.

[246] D. M. Clatterbuck, C. R. Krenn, Marvin L. Cohen, and J. W. Morris. Phonon instabilities and the ideal strength of aluminum. *Phys. Rev. Lett.*, 91:135501, Sep 2003.

[247] S. D. Wang, X. J. Liu, Z. F. Lei, D. Y. Lin, F. G. Bian, C. M. Yang, M. Y. Jiao, Q. Du, H. Wang, Y. Wu, S. H. Jiang, and Z. P. Lu. Chemical short-range ordering and its strengthening effect in refractory high-entropy alloys. *Phys. Rev. B*, 103:104107, Mar 2021.

[248] Bozhao Zhang, Jun Ding, and En Ma. Chemical short-range order in body-centered-cubic TiZrHfNb high-entropy alloys. *Applied Physics Letters*, 119(20):201908, 11 2021.

[249] C Colinet, A Bessoud, and A Pasturel. Theoretical determinations of thermodynamic data and phase diagrams of bcc binary transition-metal alloys. *Journal of Physics F: Metal Physics*, 18(5):903, 1988.

[250] Sriswaroop Dasari, Abhishek Sharma, Chao Jiang, Bharat Gwalani, Wei-Chih Lin, Kai-Chi Lo, Stéphane Gorsse, An-Chou Yeh, Srivilliputhur G. Srinivasan, and Rajarshi Banerjee. Exceptional enhancement of mechanical properties in high-entropy alloys via thermodynamically guided local chemical ordering. *Proceedings of the National Academy of Sciences*, 120(23):e2211787120, 2023.